

**PATTERNABLE ELECTROPHOSPHORESCENT ORGANIC
LIGHT-EMITTING DIODES WITH SOLUTION-PROCESSED
ORGANIC LAYERS**

A Dissertation
Presented to
The Academic Faculty

By

Andreas Haldi

In Partial Fulfillment
Of the Requirements for the Degree
Doctor of Philosophy in the
School of Electrical and Computer Engineering

Georgia Institute of Technology

December 2008

**PATTERNABLE ELECTROPHOSPHORESCENT ORGANIC
LIGHT-EMITTING DIODES WITH SOLUTION-PROCESSED
ORGANIC LAYERS**

Approved by:

Prof. Bernard Kippelen, Advisor
School of Electrical and Computer
Engineering
Georgia Institute of Technology

Prof. Russell D. Dupuis
School of Electrical and Computer
Engineering
Georgia Institute of Technology

Prof. Oliver Brand
School of Electrical and Computer
Engineering
Georgia Institute of Technology

Prof. Glenn S. Smith
School of Electrical and Computer
Engineering
Georgia Institute of Technology

Prof. Jean-Luc Brédas
School of Chemistry and Biochemistry
Georgia Institute of Technology

Date Approved: August 1, 2008

ACKNOWLEDGMENTS

Many people deserve a thank you for their support during my Ph.D. program, and I already apologize to whomever I am forgetting in the following list. First, I would like to thank my advisor, Prof. Bernard Kippelen, for accepting me as a graduate student in his group and for letting me work on whichever project I wanted to work on. Then, I have to thank Dr. Benoit Domercq for leading me to and on the OLED project towards where I knew enough about it that I could take on that research by myself. Further thanks go to my reading and oral defense committee, Prof. Russell D. Dupuis, Prof. Oliver Brand, Prof. Glenn Smith, and Prof. Jean-Luc Brédas for their availability as a committee member and for their helpful input towards additional chapters in this thesis when I proposed my Ph.D. work.

It goes without saying that my program would have lasted a lot longer if it had not been for the support of many students and postdocs in the Kippelen Research Group. There are too many to name them all, but the following have to be mentioned separately: Dr. Joshua N. Haddock for helping me out anywhere inside and outside of the lab during the first two years of my Ph.D. program, Prof. Seunghyup Yoo for his help on the vacuum deposition system and his insight into organic electronics, Dr. Canek Fuentes for any support I needed when optics came into play, William J. Potscavage for any kind of help and company during many years, and Dr. Asha Sharma for some of the device fabrication that was helpful to me, too.

Since many OLEDs in this dissertation were fabricated with newly synthesized materials, it is also necessary to mention the chemists that provided me with these

materials: Alpay Kimyonok in the group of Prof. Marcus Weck made all the phosphorescent copolymers that are used in chapter 4 and 5 of this thesis. The synthesis of hole-transport and electron-transport polymers was done by Yadong Zhang, as well as several other graduate students and postdocs in the group of Prof. Seth Marder.

And last but not least, special thanks go to my family and Erica who have supported me for a long time and were always proud of my Ph.D. program regardless of whether they saw any progress in my work or not.

The financial support for this work came in part from Solvay SA, from the STC Program of the National Science Foundation under Agreement Number DMR-0120967, and from the Office of Naval Research.

TABLE OF CONTENTS

Acknowledgments	iii
List of Tables	viii
List of Figures	ix
Summary	xiv
Chapter 1 Introduction	1
1.1 Organic Light-Emitting Diodes	1
1.2 Advantages of OLEDs	2
1.3 History of OLED Technology	4
1.4 Organic Compounds: Small Molecules and Polymers	5
1.5 Figures of Merit	6
1.6 Goal and Structure of the Dissertation.....	8
Chapter 2 Background on Organic Semiconductors and Organic Light-Emitting Diodes	10
2.1 Organic Semiconductors.....	10
2.1.1 Atomic Orbitals	11
2.1.2 Chemical bonds	12
2.1.3 Molecular Energy Levels and Energy Bands	14
2.2 Principle of Operation of OLEDs	16
2.2.1 Charge Injection.....	17
2.2.2 Charge Mobility.....	18
2.2.3 Space-Charge-Limited Current.....	21
2.2.4 Langevin Recombination.....	22
2.2.5 Singlet and Triplet Excited States.....	24
2.2.6 Light Emission.....	25
2.2.7 Energy Transfer from Host to Guest	28
2.3 OLED Efficiency	30
2.3.1 OLED Device Architecture	32
2.3.2 Light Outcoupling.....	33
Chapter 3 Experimental Methods	36
3.1 OLED Test Setup.....	36

3.2	Electroluminescence Spectra Measurements.....	37
3.3	CIE Spectral Coordinates.....	37
3.4	Luminance Calculation.....	40
3.5	OLED Efficiency Calculation.....	41
Chapter 4	Hybrid Electrophosphorescent OLEDs with a Solution-Processed Hole-Transport Layer	43
4.1	State-of-the-Art High-Efficiency OLEDs.....	43
4.2	Ionization Potential Study.....	45
4.3	Simplification of the Device Architecture	50
Chapter 5	Hybrid Electrophosphorescent OLEDs with Solution-Processed Hole-Transport and Emissive Layers.....	54
5.1	Introduction.....	54
5.1.1	Solution-Processed Multilayer Stacks and Crosslinking.....	55
5.1.2	Molecularly Doped OLEDs.....	56
5.1.3	Dendrimers	58
5.1.4	Emissive Layers from Copolymers	59
5.2	Experimental Results	61
5.2.1	Iridium Complex Variation.....	63
5.2.2	Optimization Rationale.....	66
5.2.3	Molecular Weight and Iridium Content Variation.....	68
5.2.4	Spacer Variation	72
Chapter 6	Solution-Processed Electrophosphorescent Multilayer OLEDs.....	74
6.1	Introduction.....	74
6.1.1	State of the Art.....	74
6.1.2	Crosslinking of the Emissive Layer.....	76
6.1.3	Electron-Transport/Hole-Blocking Polymer	77
6.2	Experimental Results	80
6.2.1	OLEDs with a Crosslinkable Emissive Layer	80
6.2.2	Solution-Processed Multilayer OLEDs	82
6.2.3	Photopatterned OLEDs.....	85
Chapter 7	Modeling the Charge Injection into OLEDs	88
7.1	Introduction.....	88
7.2	Theory and Model.....	90
7.3	Experiment.....	91
7.4	Results and Discussion	93

Chapter 8	Conclusions and Outlook	104
8.1	Conclusions.....	104
8.2	Outlook	107
8.3	List of Publications	109
Appendix - Device Fabrication	110	
References.....	113	

LIST OF TABLES

Table 4.1. Ionization potentials I_p , mobility, and triplet energy values of different hole-transport materials (HTM) and device performance at 100 cd/m ² of OLEDs with device structure ITO/HTM (25-35 nm)/CBP:Ir(ppy) ₃ (6%, 20 nm)/BCP (6 nm)/Alq ₃ (20 nm)/LiF (1 nm)/Al.....	47
Table 5.1. Characterization of copolymers with peak maxima of solid-state photoluminescence $\lambda_{\max,PL}$ and electroluminescence spectra $\lambda_{\max,EL}$, plus external quantum efficiencies and luminous efficiencies at 100 cd/m ² for devices based on phosphorescent copolymers with various molecular weights, various iridium concentrations, and different linkers between the side groups and the polymer backbone. The device structure was ITO/P3 (35 nm)/P(8-10)(a-c)(2-40) (20-25 nm)/BCP (40 nm)/LiF (1 nm)/Al.....	69
Table 7.1. Saturation current density J_0 , ideality factor n , parallel resistance R_p , zero-field mobility μ_0 , and mobility field-dependence factor β , all resulting from fits of the model to electrical characteristics at room temperature for α -NPD diodes with different thicknesses L	95
Table 7.2. Saturation current density J_0 , ideality factor n , parallel resistance R_p , zero-field mobility μ_0 , and mobility field-dependence factor β , all resulting from fits of the model to electrical characteristics at room temperature for organic diodes with thickness L . For pentacene and C ₆₀ diodes, the series resistance R_s is noted instead of any mobility. The effective Richardson constant A^* and the injection barrier Φ_B were extrapolated from current measurements at different temperatures.	99

LIST OF FIGURES

Figure 1.1. Sony XEL-1 OLED TV.....	2
Figure 1.2. Increase of the power efficiency of OLEDs over time.....	5
Figure 2.1. Illustration of the 2s- (a), the 2p- (b), and the hybrid (c) orbitals for a carbon atom [23].....	12
Figure 2.2. Illustration of an ethylene molecule (C_2H_4) with a σ - and a π -bond between the carbon atoms (top), and part of a conjugated polymer with overlapping p-orbitals (bottom) [23].....	13
Figure 2.3. Illustration of the interaction between the p-orbitals of N ethylene (C_2H_4) molecules with band formation in the case of an infinite number of molecules stacked on top of each other. The two p-orbitals on the carbon atoms are shown with the different phases of the wavefunction. Arrows indicate the presence of electrons in a certain energy level with the direction of the arrow denoting the direction of the spin (modified from [25]).....	15
Figure 2.4. Principle of operation of an organic light-emitting diode with charge injection (1), charge transport (2), electron-hole pair creation (3) and its migration (4), followed by recombination resulting in an excited state of a molecule, which relaxes radiatively (5). E_F denotes the Fermi energy level of the metal electrode.	16
Figure 2.5. Metal-to-organic semiconductor interface in the Schottky-Mott limit where the vacuum level is assumed to be constant for hole injection (left) and electron injection (right) with the Fermi energy E_F and the work function W of the metals, the HOMO and LUMO levels of the organic semiconductor, the ionization potential I_p , the electron affinity χ , and the injection barrier Φ_B	18
Figure 2.6. Representation of the reorganization energy λ for a hopping process according to Marcus theory. The two parabolas represent the potential energies of reactants and products.....	19
Figure 2.7. Jablonski diagram of electronic singlet and triplet states and possible transitions between these states. Solid arrows represent radiative transitions, curvy lines show nonradiative transitions from higher excited states to the lowest excited state (internal conversions, IC) and the nonradiative transition from the lowest singlet to the lowest triplet state (intersystem crossing, ISC).....	27
Figure 2.8. Förster (top) and Dexter (bottom) energy transfer in a host-guest system. The arrows denote electrons with the direction of their spin.	30

Figure 2.9. Single-layer (left) and multilayer (right) OLED device architecture with electron-blocking layer (EBL), hole-transport layer (HTL), emissive layer (EL), hole-blocking layer (HBL), and electron-transport layer (ETL).....	33
Figure 2.10. Bottom-emitting (left) and top-emitting (right) OLEDs. Small arrows in the bottom-emitting OLED represent light that is waveguided in the ITO or in the glass.	35
Figure 3.1. Illustration of the current-voltage test setup.	37
Figure 3.2. Color-matching functions \bar{x} , \bar{y} , and \bar{z} as a function of the wavelength.	38
Figure 3.3. CIE 1931 chromaticity diagram. The outer curved boundary is delimited by monochrome light with the according wavelengths in nanometers. The corners of the triangle represent the RGB primary colors, and E marks the equal energy point corresponding to a constant energy distribution in the visible wavelength range.	39
Figure 3.4. Photopic (S_{ph}) and detector (S_{det}) response as a function of the wavelength in the visible range.	41
Figure 4.1. Chemical structures of α -NPD, CBP, BCP, Ir(ppy) ₃ , and Alq ₃ (top), and the device structure of the first efficient devices reported by Baldo <i>et al.</i> [53] (bottom).....	44
Figure 4.2. Structure of crosslinkable TPD-based copolymers.	46
Figure 4.3. External quantum efficiencies as a function of the current density for OLEDs with device structure ITO/HTM (25-35 nm)/CBP:Ir(ppy) ₃ (6%, 20 nm)/BCP (6 nm)/Alq ₃ (20 nm)/LiF (1 nm)/Al.	48
Figure 4.4. Current density as a function of the applied voltage for devices with the structure ITO/HTM (25-35 nm)/CBP:Ir(ppy) ₃ (6%, 20 nm)/Al.	49
Figure 4.5. Luminance (solid shapes) and external quantum efficiency (empty shapes) as a function of the applied voltage for a device with 4 organic layers (device A, squares): ITO/PVK (25 nm)/CBP:Ir(ppy) ₃ (6%, 20 nm)/BCP (6 nm)/Alq ₃ (20 nm)/LiF (1 nm)/Al, and for a device with 3 organic layers (device B, circles): ITO/PVK (25 nm)/CBP:Ir(ppy) ₃ (6%, 20 nm)/BCP (40 nm)/LiF (1 nm)/Al. The bottom part of the figure illustrates the different device architectures.	51
Figure 4.6. Luminance (solid shapes) and external quantum efficiency (empty shapes) as a function of the applied voltage for device B (circles): ITO/PVK (25 nm)/CBP:Ir(ppy) ₃ (6%, 20 nm)/BCP (40 nm)/LiF (1 nm)/Al, for device C (diamonds): ITO/PVK (35 nm)/CBP:Ir(ppy) ₃ (6%, 20 nm)/BCP (40 nm)/LiF (1 nm)/Al, and for device D (triangles): ITO/PVK (35 nm)/CBP:Ir(ppy) ₃ (6%, 20 nm)/BCP (40 nm)/LiF (2.5 nm)/Al.	53
Figure 5.1. Chemical structure of Ir(mppy) ₃ , PBD, and the dendrimer reported by Lo <i>et al.</i> [108].	57

Figure 5.2. Electrophosphorescent copolymers with an iridium complex in the polymer backbone as described in [114] with m:n = 1:99 (a), and with an iridium complex in a side-chain of the polymer as reported in [112] with x:y:z = 18:79:3 (b).....	60
Figure 5.3. Chemical structures of carbazoyl-fluorene based copolymers with different iridium complexes where the ratio m:n is 9:1.....	62
Figure 5.4. Electroluminescence spectra for devices with the structure ITO/ P1 (35 nm)/ P(5-8) (25 nm)/BCP (6 nm)/AlQ ₃ (20 nm)/LiF (1 nm)/Al and the corresponding CIE 1931 coordinates.	64
Figure 5.5. Current density (solid symbols, top), luminance (empty symbols, bottom), and external quantum efficiency (solid symbols, bottom) as a function of the applied voltage for devices with the structure ITO/ P1 (35 nm)/(P7 or P8) (25 nm)/BCP (6 nm)/AlQ ₃ (20 nm)/LiF (1 nm)/Al.....	65
Figure 5.6. Chemical structure of orange copolymers with different linker groups.....	67
Figure 5.7. Device structure of OLEDs based on copolymers with different colors (a) and device structure for optimization of the orange-emitting copolymer P8 (b).	68
Figure 5.8. External quantum efficiencies as a function of the loading level of the iridium complex in the copolymer for OLEDs with device configuration ITO/ P3 (35 nm)/ P8a(2-40) (20-25 nm)/BCP (40 nm)/LiF (1 nm)/Al.....	70
Figure 5.9. Electroluminescence spectra for OLED devices using copolymers P8a(2, 10, 20, 40) with increasing iridium complex content as emitting layer.....	71
Figure 5.10. Current density (solid symbols, top), luminance (solid symbols, bottom), and external quantum efficiency (empty symbols, bottom) as a function of the applied voltage for a device with structure ITO/ P3 (35 nm)/ P10a(5) (25 nm)/BCP (40 nm)/LiF (1 nm)/Al.	73
Figure 6.1. Crosslinkable electrophosphorescent copolymer based on polymer P10a(5) with a charge-transport moiety (left), a phosphorescent orange-emitting complex (center), and a crosslinkable cinnamate based group (right) with m:n:o = 70:5:25.....	77
Figure 6.2. Chemical structures of solution-processable electron-transport materials used in the literature [128, 158, 162]. Whereas PFN and TPBI are examples of a polymer and a small molecule, respectively, that are soluble in organic solvents, <i>t</i> -Bu-PBD-SO ₃ Na is soluble in ethanol.	78
Figure 6.3. Chemical structures of electron-transport polymers based on a silole small-molecule (P12) and based on a bisoxadiazole small-molecule (P13).	79
Figure 6.4. Absorption spectrum of the monomer of the hole-transport moiety in copolymer P11	81

Figure 6.5. Current density (solid symbols, top), luminance (empty symbols, bottom), and external quantum efficiency (solid symbols, bottom) as a function of the applied voltage for devices with the structure ITO/ P3 (35 nm)/ P11 (17 nm)/BCP (40 nm)/LiF (2.5 nm)/Al with (circles) and without (square) 1250 mJ/cm ² UV exposure of P11	82
Figure 6.6. Current density (solid symbols, top), luminance (empty symbols, bottom), and external quantum efficiency (solid symbols, bottom) as a function of the applied voltage for devices with the structure ITO/ P3 (35 nm)/ P11 (17 nm)/ETL (35-40 nm)/LiF (2.5 nm)/Al where the electron-transport layer (ETL) consisted of BCP (squares), P12 (circles), or P13 (triangles).	83
Figure 6.7. Absorption spectra of P12 (solid line) and P13 (dashed line).	84
Figure 6.8. Schematic of interdigitated electrodes with photopatterned emissive layers (left), and a micrograph of the electrodes with a photopatterned layer of P3 (right).	86
Figure 6.9. Photograph of photopatterned OLEDs with orange electrophosphorescent and blue electrofluorescent lines with linewidths of 110 μm.	87
Figure 7.1. Equivalent circuit of an organic single-layer diode.	90
Figure 7.2. Chemical structures of α-NPD, P1 , C ₆₀ and pentacene.	92
Figure 7.3. Current density versus applied voltage at room temperature for α-NPD diodes with thicknesses of 80 nm and 150 nm. Plots of five devices are shown for each thickness.	94
Figure 7.4. Current density as a function of the applied voltage at room temperature for α-NPD diodes with thicknesses ranging from 60 nm to 150 nm. Experimental data is shown as empty symbols; solid lines represent the simulated curves.	95
Figure 7.5. Current density as a function of the applied voltage at room temperature for organic diodes with organic layers of α-NPD (100 nm, squares) and P1 (90 nm, circles). Experimental data is shown as empty symbols; solid lines represent the simulated curves.	96
Figure 7.6. Current density as a function of the applied voltage for an α-NPD diode with a thickness of 100 nm measured at temperatures ranging from 1 °C to 72 °C. Experimental data is shown as empty symbols; solid lines represent the simulated curves.	97
Figure 7.7. Plot of zero-field mobility versus (1000/T) ² for organic diodes consisting of α-NPD (100 nm, squares) and P1 (90 nm, circles). Experimental data is shown as empty symbols; solid lines are linear fits to this data.	98
Figure 7.8. Current density as a function of the applied voltage at room temperature for organic diodes with organic layers of pentacene (80 nm, triangles) and C ₆₀ (100 nm)/	

BCP (8 nm, diamonds). Experimental data is shown as empty symbols; solid lines represent the simulated curves.	101
Figure 7.9. Current density as a function of the applied voltage for a pentacene diode with a thickness of 80 nm measured at temperatures ranging from 1 °C to 72 °C. Experimental data is shown as empty symbols; solid lines represent the simulated curves.	102
Figure 7.10. Plot of (J_0/T^2) versus $(1/kT)$ for organic diodes consisting of three different materials to extrapolate the injection barrier Φ_B and the effective Richardson constant A^* . Experimental data is shown as empty symbols; solid lines are linear fits to the data. ...	103
Figure A-1. Diagram of the substrate cleaning process.	110
Figure A-2. Diagram of the OLED device fabrication process.	111
Figure A-3. Diagram of the fabrication process for patterned solution-processed multilayer OLEDs.	112

SUMMARY

Organic light-emitting diodes (OLEDs) have drawn much attention in the last two decades because of several advantages, such as high brightness and a wide viewing angle. In recent years, the power efficiency of OLEDs has been increased to exceed the efficiency of fluorescent light bulbs. However, such high-efficiency devices are typically based on small molecules that have to be evaporated in vacuum. A much higher fabrication throughput and therefore lowered costs are expected if high-efficiency OLEDs were processed from solution.

The present work shows how solution-processed electrophosphorescent multilayer OLEDs can be achieved by starting with an evaporated three-layer device structure and replacing layer by layer with a solution-processed layer. First, the hole-transport layer will be replaced by a polymer and high efficiencies are observed when using a hole-transport polymer with a high ionization potential and a low hole mobility. Then, the emissive layer is replaced by a copolymer consisting of hole-transport groups and emissive complexes in its side-chains. OLEDs with four different colors are shown where the orange devices show the highest efficiency. The orange copolymer is further optimized by making changes to the chemical nature of the polymer, such as different molecular weight, different concentrations of the emissive complex and different linkers between the side-chains and the polymer backbone.

Finally, a three-layer solution-processed OLED is fabricated by crosslinking the hole-transport and the emissive layer, and by spin-coating an electron-transport polymer on top. Moreover, using the photocrosslinking properties of the emissive layer, solution-

processed multilayer OLEDs of two different colors (orange and blue) are patterned using photolithography to fabricate a white-light source with a tunable emission spectrum.

Furthermore, with more and more organic semiconductors being integrated into the circuitry of commercial products, good electrical models are needed for a circuit design with predictive capabilities. Therefore, a model for the example of an organic single-layer diode is introduced in the last chapter of this thesis. The model has been implemented into SPICE and consists of an equivalent circuit that is mostly based on intrinsic material properties, which can be measured in independent experiments. The model has been tested on four different organic materials. Material parameters that were extracted from a fit of the model to the experimental electrical characteristics of the diodes agree well with values from the literature.

CHAPTER 1

INTRODUCTION

1.1 Organic Light-Emitting Diodes

Organic light-emitting diodes (OLEDs) have received a large interest in the research community for the last twenty years. OLEDs consist of a thin film of an organic compound placed between two electrodes. By applying a voltage to the electrodes, charges get injected into the organic material where they form excited states that recombine and generate light.

In the past nine years, OLED displays have become commercially available in portable small electronics applications, such as mobile phones, MP3 players, car radios, digital cameras, and TVs. OLED displays are especially suited for such applications because of their reduced power consumption compared to LCDs. In OLED displays, only active pixels are turned on while inactive pixels do not use any power, whereas LCD displays require the same power for their backlight independent of whether a black or a white picture is shown. Furthermore, since the color of an OLED can be tuned, no filters are necessary in the fabrication of an OLED display and very thin displays can be fabricated, which is another important factor for portable devices that have to be packed as efficiently as possible.

Whereas small OLED displays can be produced cost-efficiently nowadays and while Samsung has already shown prototypes of OLED displays with diagonals up to 40 inches, the fabrication of larger displays is still very cost-intensive and will have to be improved significantly if OLEDs should ever become competitive with other

technologies in the computer or TV display market. Nevertheless, the first commercial OLED TV has just been introduced to the market by Sony Corp. (see Figure 1.1) [1]. However, the price tag of \$2,500 for this 11-inch TV at the time of its introduction into the market in the year 2008 is nowhere near competitive to other display technologies.



Figure 1.1. Sony XEL-1 OLED TV.

1.2 Advantages of OLEDs

OLEDs have many advantages over other display technologies. For example, OLEDs are very thin devices with the thickness of the organic layers in the range of about 100 nm. As mentioned, no backlight or color filters are needed for OLED displays either, which leads to unusually thin displays like the Sony TV with a display thickness of 3 mm and Sony's newest prototypes with a display thickness of only 0.3 mm [1].

Because of the small thickness of these devices, displays can also be made much lighter, and the main weight comes from the device substrate.

Furthermore, the close relationship of organic materials to plastics and the thinness of the devices allow for flexibility and make OLEDs compatible with plastic substrates. Much work has therefore been done on flexible substrates and first prototypes of flexible color displays have already been shown [1].

Because of the vertical device structure of an OLED, with electrodes on top and on the bottom of the device, OLEDs also have the advantage that they are theoretically not limited in the lateral dimensions. However, with current fabrication processes OLED devices with an area of only up to 100 cm² seem feasible [2].

Last but not least, OLED devices show high brightness that is suitable for display applications as well as for lighting. The direct emission of every single pixel also leads to wide viewing angle with every angle receiving the same amount of light (Lambertian emitter), which makes OLEDs stand out compared to LCD displays with an increasing but still limited viewing angle.

The biggest disadvantage of OLEDs is their degradation in air. Hence, proper encapsulation with very low leakage of oxygen and moisture is needed. For a long time, even the lifetime of OLEDs in inert atmosphere was considered a serious issue. However, by optimizing the materials and the device structures, OLED lifetimes have now reached a point where their lifetime is comparable or exceeds the expected lifetime of commercial products [2, 3].

1.3 History of OLED Technology

The early history of OLEDs goes back to the 1950s and 1960s [4, 5]. In experiments on μm to mm-thick organic crystals, electroluminescence was observed when voltages of a few hundreds of volts were applied [5]. Since such voltages are impractical for most applications, these early results went almost forgotten until the technical progress in semiconductor processing allowed the fabrication of thin organic films where electroluminescence could be observed at applied voltages of only 30V [6]. Nevertheless, it took another 5 years until the first OLEDs with a reasonable power efficiency of more than 1 lm/W were demonstrated [7]. Whereas these first devices were all based on organic small molecules, electroluminescence was shown in polymers only a few years later [8].

The reports by Tang *et al.* [7] and Burroughes *et al.* [8] sparked research in OLEDs, and increasing efficiencies were reported at a steady pace by using more efficient device architectures and, especially, by synthesizing materials with higher photoluminescence quantum yields. However, the biggest increase in efficiency resulted from the introduction of phosphorescent dyes into OLED devices, which multiplied the efficiencies by a factor of four as will be shown in the next chapter [9].

Further optimization of these devices recently led to power efficiencies in the range of 100 lm/W (see Figure 1.2). Such high-efficiency OLEDs are typically based on small molecules that are evaporated in vacuum and that emit in the green color spectrum since the eye is most sensitive at these wavelengths. The power efficiencies of OLEDs in other colors are still inferior to green devices, but they have also been increased and even white OLEDs now reach efficiencies that are close to those of fluorescent lamps and

therefore make OLEDs also a potential candidate for lighting applications. On the other hand, OLEDs with a solution-processed emissive layer generally show lower efficiencies and require some evaporated organic layers to maximize the efficiency (hybrid OLEDs).

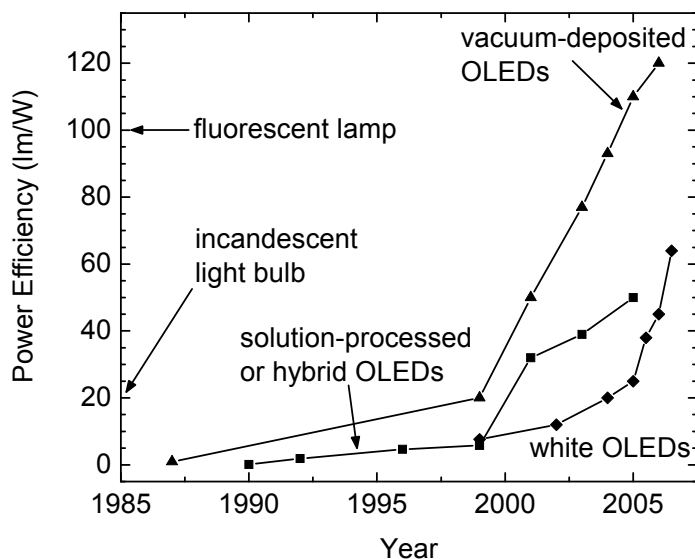


Figure 1.2. Increase of the power efficiency of OLEDs over time.

1.4 Organic Compounds: Small Molecules and Polymers

Organic compounds are molecules that consist of several atoms (mostly carbon atoms) held together by covalent bonds, which means that some of their atoms share electrons, as will be explained in chapter 2. For fabrication reasons, two different classes of organic compounds have to be distinguished: small molecules and polymers. Whereas organic small molecules contain only a few carbon atoms, a polymer consists of a long chain of repeated units connected to each other via covalent bonds. While the fabrication

of OLEDs based on small molecules are typically fabricated using thermal evaporation with expensive equipment in high-vacuum, polymers can be dissolved in and processed from solution using well known techniques, such as inkjet printing [10] or screen printing [11]. Furthermore, polymers tend to entangle with each other in the solid state, which makes them thermally more stable than small molecules that tend to crystallize at temperatures below 100 °C [12, 13].

Compared to vacuum-processing, solution-processing of semiconductor materials can help reduce production costs since it can be done at atmospheric pressure, which saves pumping time, and thus increases the throughput. Furthermore, extensive research has already been put into solution-processing by the printing industry, and fabrication processes could be optimized quickly. Organic semiconductors can even be printed in roll-to-roll processes, as has been shown for RF ID tags with organic semiconductors by PolyIC GmbH & Co. KG [14] and for OLEDs by General Electric Co. [15]

1.5 Figures of Merit

Different parameters have been defined to quantify the quality of an OLED, and the most important figures of merit are the following:

Internal quantum efficiency (IQE): The internal quantum efficiency describes the ratio between the number of photons that are emitted in the organic layers of the OLED and the number of electrons that were injected into the device. The IQE is measured as a percentage.

External quantum efficiency (EQE): The external quantum efficiency is probably the most reported figure of merit. The EQE is based on the IQE; however, it also includes

the extraction loss of photons from the organic layers into the air. Therefore, it describes the number of photons that are emitted by an OLED towards the viewer per injected electron. Like the IQE, the EQE is given as a percentage.

Current efficiency: The current efficiency has a unit of cd/A and is proportional to the EQE. However, in the current efficiency, the number of photons is weighed by the spectral response of the eye.

Power efficiency: Similar to the current efficiency, the power efficiency also takes into account the applied voltage that is necessary to achieve a particular brightness. The power efficiency is given in lm/W.

Maximum luminance: The maximum luminance describes the highest brightness that can be observed from a device before it disintegrates. This parameter determines what application a device is suitable for since different applications have different brightness requirements.

Lifetime: For commercial applications, the lifetime of a device is essential. Due to material and interface degradation in an OLED under operation, a decrease in brightness can be observed over time. The lifetime of a device is therefore defined as the time it takes for an OLED to show half of the initial brightness with the OLED being driven either at a constant current or at a constant voltage.

Color purity: For display applications, it is important that a wide color gamut can be achieved. For that purpose, the three primary colors red, green, and blue should be as pure as possible, meaning that their emission spectrum should be as narrow as possible to approximate an almost monochromatic emission. For an optimized gamut,

monochromatic light with a wavelength of 700 nm, 546.1 nm, and 435.8 nm for red, green, and blue is required [16].

Since the efficiencies and the lifetime of OLEDs are dependent on the brightness of the device, they are usually measured at 100 cd/m² or 1,000 cd/m². 100 cd/m² is the typical brightness of small, portable display applications, such as laptop displays. For lighting applications, 5,000 cd/m² or more are needed.

Even though all these parameters have to be optimized for most commercial applications, this task is very time-consuming and cannot be done efficiently in the time of a Ph.D. program. The present work therefore focuses on optimizing the external quantum efficiency.

1.6 Goal and Structure of the Dissertation

As has been discussed above, solution-processed electrophosphorescent OLEDs show many advantages in the fabrication of devices. However, their efficiencies are still significantly lower than the efficiencies that have been measured for vacuum-deposited small-molecule OLEDs. The present work shows how efficient solution-processed OLEDs can be achieved. Starting from a multilayer device structure for vacuum-deposited small-molecule OLEDs that has been reported in the literature, layers will be replaced one by one with a solution-processed material until all organic layers are processed from solution. Furthermore, the last chapter introduces a device model for simple organic diodes that can be used for electrical design of circuits that incorporate organic materials and is therefore essential for the successful integration of organic semiconductors into commercial products.

This thesis is structured as follows. Chapter 2 reviews the basic background on organic semiconductors, the OLED device architecture, and chapter 3 explains the used test setup for OLED measurements. Chapter 4 then describes the state of the art for vacuum-deposited electrophosphorescent OLEDs and shows how high efficiencies can be achieved in a simplified hybrid OLED device structure where the hole-transport material is deposited from solution.

In chapter 5, methods to achieve multilayer devices from solution are explained. Then, the current state of the art for OLEDs with solution-processed emissive layers is discussed, and our approach of electrophosphorescent copolymers as the emissive layer is introduced. Copolymers with different colors are incorporated in OLEDs and the chemical structure of one of these copolymers is optimized to achieve high efficiencies in an OLED.

Chapter 6 concludes the fabrication of a solution-processed three-layer OLED by introducing an insoluble emissive layer and two newly synthesized electron-transport polymers. By patterning the emissive layers, a light source consisting of two different colors is used to generate light with a tunable emission spectrum.

Finally, chapter 7 introduces a model for the electrical characteristics of an organic diode that can be used to design circuits with organic semiconductors. By fitting the model to experimental data of organic diodes with several materials, intrinsic parameters of these organic semiconductors are extracted and compared to values from the literature.

CHAPTER 2

BACKGROUND ON ORGANIC SEMICONDUCTORS AND ORGANIC LIGHT-EMITTING DIODES

2.1 Organic Semiconductors

Whereas inorganic semiconductors are based on a large network of covalent bonds between atoms, organic semiconductors consist of organic (carbon-based) molecules that interact through dipole-dipole forces, the van der Waals force. For a long time, organic semiconductors were only seen as insulators with wide bandgaps and a rather low conductivity [17-20]. However, in recent years, mobilities in organic thin-film devices exceeding $1 \text{ cm}^2/\text{Vs}$ have been reported [21-23], which is comparable to mobilities measured in amorphous silicon. Moreover, although organic semiconductors typically also exhibit an amorphous structure, fewer intrinsic defects are found in a system of nonradical molecules compared to inorganic amorphous semiconductors where a large number of dangling bonds exists.

Furthermore, not only do many organic semiconductors have bandgaps in the range of 1.5 to 3.5 eV, and can therefore emit light in the visible region, but the organic molecules can also be tailored to show any desired property, such as a specific ionization potential or a particular emission spectrum, and an almost unlimited number of semiconductor materials are feasible. The origin of the semiconductor properties of organic materials will be reviewed in the following subsections.

2.1.1 Atomic Orbitals

To understand the origin of charge transport in organic semiconductors, atomic orbitals and their tendency to form chemical bonds have to be considered first. By solving the Schrödinger equation for a hydrogen atom, wavefunctions can be defined that describe the region where one or two electrons can be found for the atom, the orbitals. Even though the Schrödinger equation includes additional terms for heavier atoms, it can be assumed that these terms just cause slight distortions to the orbitals of the hydrogen atom. Therefore, orbitals are often used in organic compounds to describe chemical bonds between atoms, where the bond results from the overlap of orbitals from separate atoms. In carbon, each atom has four valence orbitals ($2s$, $2p_x$, $2p_y$, and $2p_z$) that are responsible for the formation of covalent bonds (see Figure 2.1) [24]. However, for covalent bonds, it turns out that the s - and p -orbitals are linearly superposed to new orbitals, the hybrid orbitals. Three different kinds of hybrid orbitals are possible: sp^1 , sp^2 , and sp^3 where the subscript denotes the number of p -orbitals that are part of the superposition (see Figure 2.1).

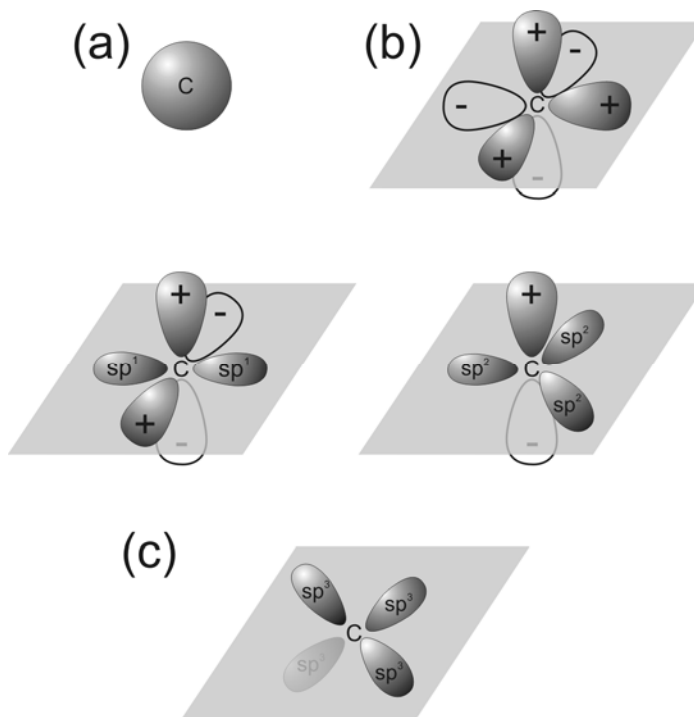


Figure 2.1. Illustration of the 2s- (a), the 2p- (b), and the hybrid (c) orbitals for a carbon atom [24].

2.1.2 Chemical bonds

With the introduction of hybrid orbitals, the formation of covalent bonds is straightforward. First, by overlapping the hybrid orbitals sp^1 , sp^2 , or sp^3 of two atoms, the covalent single bonds, or σ -bonds, are formed. However, more important in organic semiconductors are the double and triple bonds, which consist of one σ -bond and one or two π -bonds, respectively, and which occur in systems with sp^2 or sp^1 hybridization. In such systems, the π -bond results from the overlap of atomic orbitals with pure p-character as shown in Figure 2.2.

Whereas the spatial overlap between the hybrid orbitals in σ -bonds is large, the overlap of p-orbitals in π -bonds is rather small, and therefore, the bonding energy is smaller in π -bonds than in σ -bonds. However, because of the weaker coupling between the p-orbitals, the electrons in these orbitals tend to be more delocalized in space, and more polarization of the electrons can be expected. In molecular systems in which single and double bonds or double and triple bonds alternate, the conjugated systems, the delocalization of the electrons can be achieved over an even longer range of distance than just two atoms, since p-orbitals keep overlapping each other along the chain (Figure 2.2).

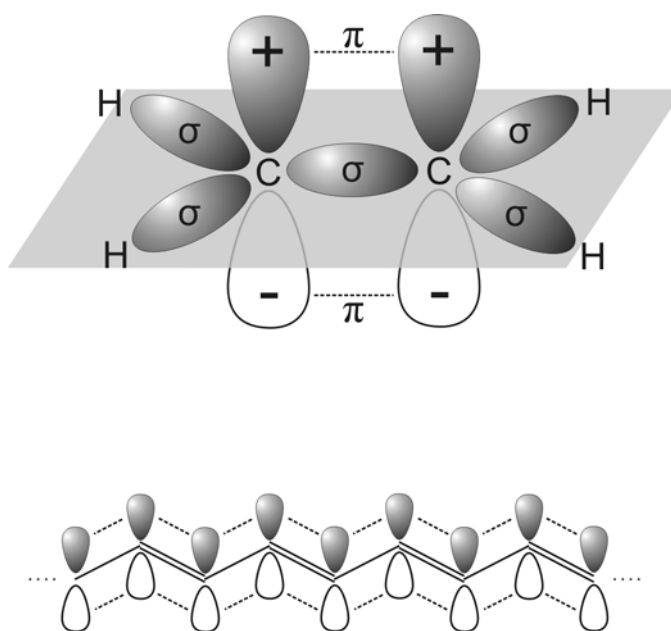


Figure 2.2. Illustration of an ethylene molecule (C₂H₄) with a σ - and a π -bond between the carbon atoms (top), and part of a conjugated polymer with overlapping p-orbitals (bottom) [24].

2.1.3 Molecular Energy Levels and Energy Bands

Because of the above mentioned delocalization of the electrons, wavefunctions have to be defined that describe the location of an electron on the whole molecule rather than just on an atom, the molecular orbitals. Since the Schrödinger equation becomes very complicated in a system with several atoms and electrons, eigenfunctions and eigenvalues of the Hamiltonian are usually approximated by neglecting certain terms in the Hamiltonian. The following section will describe one of these approximations for molecular orbitals, the linear combination of atomic orbitals-molecular orbitals (LCAO-MO). It has been mentioned before that the bonding energy is larger in σ -bonds than in π -bonds. Hence, electrons in σ -bonds are harder to remove than electrons in π -bonds, and their contribution to the electrical current can be neglected [25]. Therefore, the following part of this section will only focus on the π -molecular orbitals.

The wavefunction Ψ_π of a π -molecular orbital can be defined in first approximation as linear combinations of the atomic p-orbitals with wavefunction Φ_l :

$$\Psi_\pi = \sum_{l=1}^N a_l \Phi_l \quad (2.1)$$

where N is the number of carbon atoms in the molecule, a_l are linear coefficients, and the sum goes over all carbon atoms [25]. For N carbon atoms, we can define N molecular orbitals that are orthogonal given the hermiticity of the Hamiltonian. In the ground state of a molecule, the molecular orbitals of the lowest energies are filled with two electrons of opposite spin (Pauli-Principle). The filled molecular orbital with the highest energy is then called the highest occupied molecular orbital (HOMO), whereas the molecular orbital with the next higher energy contains no electron and is called the lowest unoccupied molecular orbital (LUMO) (see Figure 2.3).

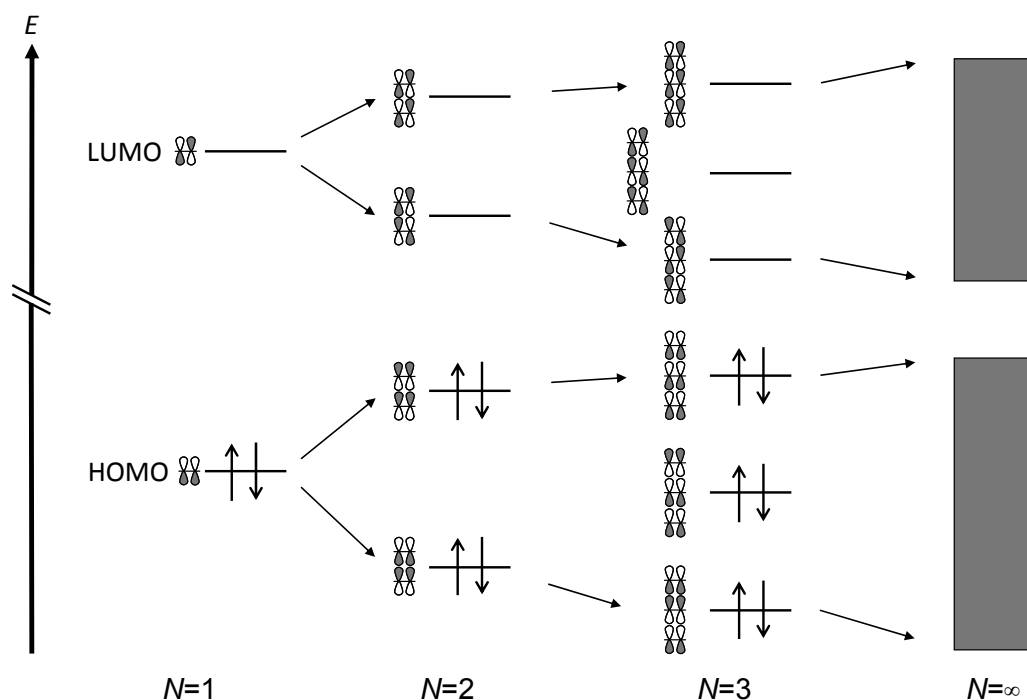


Figure 2.3. Illustration of the interaction between the p-orbitals of N ethylene (C_2H_4) molecules with band formation in the case of an infinite number of molecules stacked on top of each other. The two p-orbitals on the carbon atoms are shown with the different phases of the wavefunction. Arrows indicate the presence of electrons in a certain energy level with the direction of the arrow denoting the direction of the spin (modified from [26]).

In molecular solids where organic molecules are within a close distance to each other, molecular orbitals of different molecules overlap. Even a system of two molecules can therefore not be considered like two separate molecules, but the energy of the molecular orbitals splits because of interactions between the molecules. Hence, if many molecules start interacting, the splitting of the energies causes a bandlike structure comparable to valence and conduction bands in inorganic semiconductors (see Figure 2.3) [26].

2.2 Principle of Operation of OLEDs

OLEDs operate in a similar fashion to inorganic light-emitting diodes. By applying a voltage to the anode and the cathode, charges are injected from the electrodes into the organic semiconductor. Holes and electrons then travel in the semiconductor toward the opposite electrodes. When the charges meet, they create an electron-hole pair that can further diffuse in the organic semiconductor until it recombines to form a molecular excited state, which relaxes and emits light (see Figure 2.4). Each of these steps is explained in more details in the following subsections.

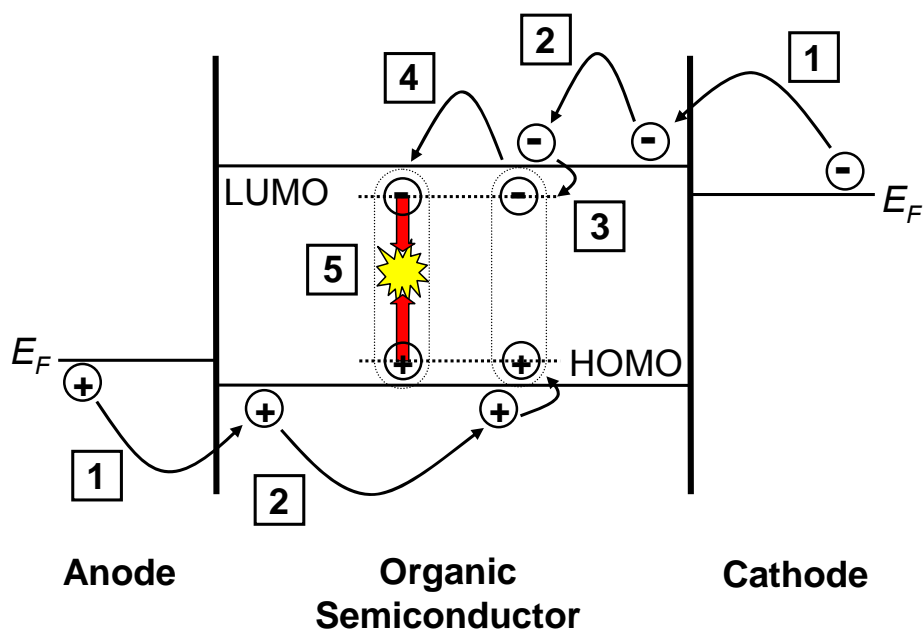


Figure 2.4. Principle of operation of an organic light-emitting diode with charge injection (1), charge transport (2), electron-hole pair creation (3) and its migration (4), followed by recombination resulting in an excited state of a molecule, which relaxes radiatively (5). E_F denotes the Fermi energy level of the metal electrode.

2.2.1 Charge Injection

As for inorganic semiconductor devices, the contact of the metal electrode to the organic semiconductor plays an important role in the operation of the device. Although the physics at the metal-organic interface is not quite clear on a microscopic basic, it is generally understood that the injection current from a metal electrode into an organic semiconductor can be adapted from equations for Schottky contacts in inorganic semiconductors [27]. To get injected, charges have to get across the energy barrier that is formed between the work function W of the injecting electrode and the HOMO or LUMO energy level of the organic semiconductor depending on whether hole- or electron-injection, respectively, is considered (Figure 2.5). The current density J across this energy barrier is then given by the general diode equation:

$$J = J_0 \left(\exp \left[\frac{qV}{nkT} \right] - 1 \right) \quad (2.2)$$

where J_0 is the saturation current density, q is the elementary charge, V is the applied voltage, n is the ideality factor, k is the Boltzmann constant, and T is the temperature. The saturation current density is dependent on the chosen model for injection and can be attributed to either thermionic emission or charge tunneling [28-30]. Many studies have found good agreement of experimental data to the thermionic emission model [29, 31, 32], where the saturation current density J_0 is given by the equation:

$$J_0 = A^* T^2 \exp \left(- \frac{\Phi_B}{kT} \right) \quad (2.3)$$

with A^* the effective Richardson constant and Φ_B the injection barrier for charges as shown in Figure 2.5 [33].

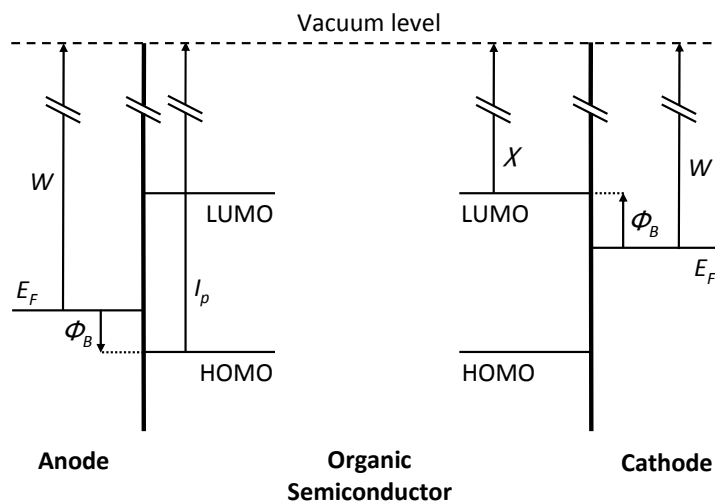


Figure 2.5. Metal-to-organic semiconductor interface in the Schottky-Mott limit where the vacuum level is assumed to be constant for hole injection (left) and electron injection (right) with the Fermi energy E_F and the work function W of the metals, the HOMO and LUMO levels of the organic semiconductor, the ionization potential I_p , the electron affinity χ , and the injection barrier Φ_B .

2.2.2 Charge Mobility

In a microscopic

view, charge transport in a molecular material can be seen as a hopping process that is based on an electron-transfer reaction, in which an electron is moving between two neighboring molecules as schematized in the following equation for a hole hopping process:



where A and B are two neighboring molecules. This reaction results in a motion of

positive charge, which can be directed by an applied electric field. The rate constant k_{ET} of the electron-transfer reaction can be described by Marcus theory as

$$k_{ET} = A_0 \exp\left[\frac{-\lambda}{4k_B T}\right] \quad (2.5)$$

where A_0 is a prefactor related to the electron coupling matrix element between donor A and acceptor B , and λ is the reorganization energy [34, 35]. The reorganization energy λ represents the energy that is necessary to transfer an electron from molecule A to molecule B



while the geometries of both molecules remains fixed since the electron-transfer process occurs in a much faster time frame than the molecules can relax into a geometry that is energetically most stable (see Figure 2.6).

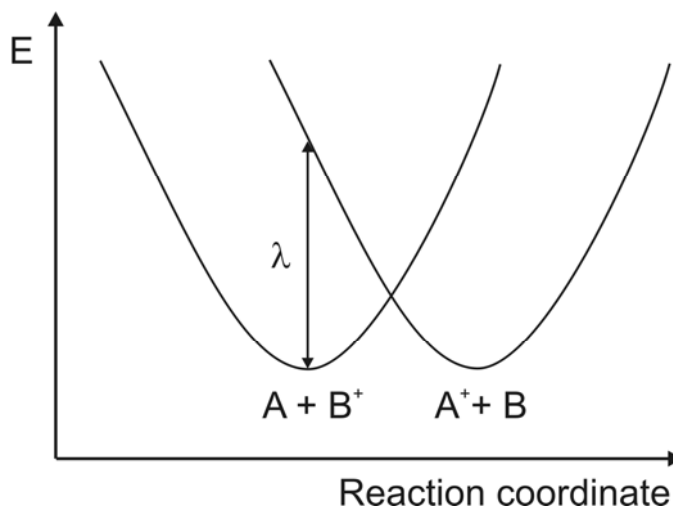


Figure 2.6. Representation of the reorganization energy λ for a hopping process according to Marcus theory. The two parabolas represent the potential energies of reactants and products.

From the assumption that all charge transport results from charges hopping through a manifold of localized states with superimposed positional disorder, the so-called disorder formalism has been derived [36, 37]. In this formalism, hopping site energies and distances have Gaussian distributions, i.e. for the hopping sites energies the distribution is

$$g(\varepsilon) = (2\pi\sigma^2)^{-1/2} \exp\left(-\frac{\varepsilon^2}{2\sigma^2}\right) \quad (2.7)$$

where the energy ε is measured relative to the center of the distribution and σ is the width of the energetical disorder distribution.

Furthermore, assuming significant disorder effects such that electron-phonon coupling is weak enough to neglect polaronic effects [38], and assuming that each hopping event is statistically independent and that hopping between sites i and j with energies ε_i and ε_j , respectively, can be described by jump rates ν_{ij} of the Miller-Abrahams form

$$\nu_{ij} = \nu_0 \exp(-2\gamma\Delta R_{ij}) \exp\left[-\left(\frac{\varepsilon_i - \varepsilon_j}{kT}\right)\right]; \varepsilon_i > \varepsilon_j \quad (2.8)$$

$$\nu_{ij} = \nu_0 \exp(-2\gamma\Delta R_{ij}); \varepsilon_i < \varepsilon_j \quad (2.9)$$

where ν_0 is a pre-factor, γ is the inverse wave function decay constant, and ΔR_{ij} is the intersite distance between sites i and j [39, 40]. Monte Carlo simulations of a system based on the equations above, led to an empirical equation of the mobility μ as a function of the temperature and the applied electric field E

$$\mu(\sigma, E) = \mu_{0,0} \exp\left[-\left(\frac{2}{3} \frac{\sigma}{kT}\right)^2\right] \exp\left[C\left(\left[\frac{\sigma}{kT}\right]^2 - \Sigma^2\right)E^{1/2}\right] \quad (2.10)$$

where $\mu_{0,0}$ is the disorder-free mobility, C is an empirical constant with a value of $2.9 \times 10^{-4} \text{ (cm/V)}^{1/2}$, and Σ is the width of the positional disorder distribution [37]. Equation (2.10) is only valid for high electric fields larger than 10^5 V/cm and for temperatures below the glass transition temperature T_g [41], and for a width of the position disorder distribution $\Sigma \geq 1.5$ [37].

2.2.3 Space-Charge-Limited Current

For low applied electric fields, the charge transport in organic semiconductors is given by the ohmic drift current:

$$J = n_0 e \mu \frac{V}{L} \quad (2.11)$$

where e is the elementary charge, n_0 the charge carrier density, μ the charge mobility, V the applied voltage and L the device thickness. However, assuming an ohmic contact that can supply an infinite number of charges and due to the low free-carrier density in organic semiconductors, it is possible at higher applied electric fields that more charges are injected than can be transported and excess charges start building up in the semiconductor [42].

Because of these excess charges, the electric field inside the semiconductor is no longer constant, and the current behavior cannot be explained with the ohmic drift current anymore. Instead, Mott and Gurney have shown that this space-charge-limited current (SCLC) follows the equation:

$$J = \frac{9}{8} \mu \varepsilon \varepsilon_0 \frac{V^2}{L^3} \quad (2.12)$$

where ε is the dielectric constant, and ε_0 is the permittivity of free space [25, 43]. Alternatively, in the presence of trap states with an exponential distribution, a trap-charge limited current density can be written as

$$J = \frac{N_{eff} e \mu}{H^l} \left(\frac{\varepsilon_0 \varepsilon}{e} \frac{l}{l+1} \right)^l \left(\frac{2l+1}{l+1} \right)^{l+1} \frac{V^{l+1}}{L^{2l+1}} \quad (2.13)$$

where N_{eff} is the effective density of states in the transport band, H is the total concentration of traps, and l is a characteristic distribution parameter [44].

As has been discussed above (section 2.2.2), the mobility in organic semiconductors is typically field-dependent while the general equation (2.12) for SCLC was derived for field-independent mobilities. By introducing the Frenkel effect into the derivation for SCLC, where only one set of traps with an effective trap depth that is reduced by the effective field is considered, P.N. Murgatroyd has shown that the equation for SCLC can be written as

$$J = \frac{9}{8} \varepsilon \varepsilon_0 \mu_0 \exp\left(0.891\beta \frac{V}{L}\right) \frac{V^2}{L^3} \quad (2.14)$$

with μ_0 the zero-field mobility and β the field-dependence factor of the mobility [45].

2.2.4 Langevin Recombination

After both holes and electrons have been injected into an organic semiconductor, the two charges start interacting and recombination can occur. The recombination of statistically independent oppositely charged carriers has been studied by Paul Langevin in 1903 [46]. Assuming that just one particle is moving with a thermal energy of kT while

the other particle is stationary, the moving charge gets trapped in the Coulomb potential of the stationary charge once they are within a distance of less than the coulombic capture radius r_c , where the coulomb attractive potential energy is equal to the thermal energy:

$$\frac{e^2}{4\pi\epsilon\epsilon_0 r_c} = kT \quad (2.15)$$

or

$$r_c = \frac{e^2}{4\pi\epsilon\epsilon_0 kT}. \quad (2.16)$$

It can be assumed that the same effect occurs even when both carriers are moving as long as their mean free path is smaller than the coulombic capture radius, which is given for organic materials with mobilities below $1 \text{ cm}^2/\text{Vs}$ and a coulombic capture radius of roughly 20 nm at room temperature and with $\epsilon = 3$ [25]. Thus, the recombination in organic semiconductors can be viewed as a drift of the opposite charges towards each other because of the coulombic field. The electron-hole pair can then diffuse through the organic semiconductor [47, 48] until it recombines, which results in a charge-neutral excited state of a molecule where one electron is found in one of the usually unoccupied molecular orbitals, while one hole is present in one of the normally occupied molecular orbitals. The recombination rate for the Langevin recombination is given by

$$\dot{n}_+ = \dot{n}_- = -n_+ n_- e(\mu_e + \mu_h) / \epsilon\epsilon_0. \quad (2.17)$$

where n_+ is the density of holes, n_- is the density of electrons, ϵ_0 is the permittivity of free space, ϵ is the dielectric constant, and μ_e and μ_h are the electron and the hole mobility, respectively [49].

2.2.5 Singlet and Triplet Excited States

The electronic excited states of a molecule, where one electron is excited from an occupied state into an unoccupied state and thus leaves a hole, can be described in quantum mechanics. Since a hole represents just a missing electron, both the hole and the electron can be represented by similar wavefunctions. In a system with two particles of spin 1/2, eigenstates of the Hamiltonian have to be antisymmetric in respect to the exchange of the particles (Pauli Principle) [50]. Since the wavefunctions can be written as the product of the spatial and the spin wavefunctions, the spin wavefunction can therefore be either symmetric or antisymmetric as long as the spatial wavefunction has the opposite parity. For the electron and the hole, the spin part of the wavefunction can be represented by $\Psi_{spin} = |\uparrow\rangle$ or $|\downarrow\rangle$ where the arrow describes the direction of the spin. The four possible combinations of the spin wavefunctions can therefore be differentiated between one antisymmetric (singlet) state S_n :

$$\Psi_{spin} = \frac{1}{\sqrt{2}} \left(|\uparrow\rangle|\downarrow\rangle - |\downarrow\rangle|\uparrow\rangle \right) \quad (2.18)$$

and three symmetric (triplet) states T_n :

$$\Psi_{spin} = \frac{1}{\sqrt{2}} \left(|\uparrow\rangle|\downarrow\rangle + |\downarrow\rangle|\uparrow\rangle \right) \quad (2.19)$$

$$\Psi_{spin} = |\uparrow\rangle|\uparrow\rangle \quad (2.20)$$

$$\Psi_{spin} = |\downarrow\rangle|\downarrow\rangle. \quad (2.21)$$

It has to be noted that the Langevin recombination does not necessarily generate excited singlet and triplet states with the lowest energy (S_1 or T_1) at their formation, but higher excited states (S_n or T_n) can be generated initially. However, while higher excited

states are important for the formation ratio between singlet and triplet states [51], they have a very short lifetime and decay quickly into the lowest excited states through a nonradiative process, known as internal conversion. In the following parts, we therefore concentrate on the lowest excited states and their recombination.

2.2.6 Light Emission

After its generation, the excited electronic state of a molecule has a given lifetime until it relaxes back to the ground state in a radiative or nonradiative process. The probability P of radiative relaxation from state Ψ_i to state Ψ_j is proportional to the square of the transition dipole moment

$$P \propto \langle \Psi_i | M | \Psi_j \rangle^2 = \left| \int \Psi_i M \Psi_j d\tau \right|^2 \quad (2.22)$$

where M is the dipole moment operator and the integration over $d\tau$ covers the whole space of all $3N$ coordinates with N the number of electrons. Since

$$M = \sum_i e r_i \quad (2.23)$$

where e is the electron charge and r_i is the distance of the i th electron from the origin of a coordinate system that is fixed to the molecule, the dipole moment operator does not affect the spin part of the wavefunction of a state. Therefore, only transitions with similar spin symmetry result in a transition dipole moment that is unequal to zero. Hence, with the ground state S_0 being a singlet state, radiative transitions are only possible between the lowest singlet excited state S_1 and the ground state S_0 , whereas transitions from the lowest triplet excited state T_1 to the ground state are forbidden. The resulting radiation from such transitions is called fluorescence.

However, this assumption holds only in first approximation where the total Hamiltonian is assumed to include just the ordinary Hamiltonian and electron repulsion. Some relativistic effects can be included by adding the first term of the relativistic expansion of the Dirac equation, the so-called spin-orbit coupling term. The x-component of the spin-orbit coupling Hamiltonian can be written as

$$H_{SO}^x = \frac{1}{2n} \sum_i^n \sum_k^n (A_i l_{xi} + A_k l_{xk}) (s_{xi} + s_{xk}) + \frac{1}{2n} \sum_i^n \sum_k^n (A_i l_{xi} - A_k l_{xk}) (s_{xi} - s_{xk}) \quad (2.24)$$

where

$$A_i = \sum_j^m \left(\frac{1}{r_{ij}} \right) \left(\frac{dV(r_{ij})}{dr_{ij}} \right) \quad (2.25)$$

with j a particular nucleus, r_{ij} the distance from electron i to the nucleus j , l the atomic orbital operator, s the spin operator, V the nuclear potential, n the number of electrons, and m the number of nuclei [52].

Whereas the spin part of the first term in equation (2.24) is symmetric with respect to the exchange of electrons, the spin part of the second term is asymmetric for electron wavefunctions with the same angular quantum number l . Therefore, wavefunctions with different spin symmetry are no longer orthogonal to each other, but the triplet states gain some singlet character and vice versa. It turns out that when spin-orbit coupling is considered, radiative recombination from a triplet state to the ground state, the so-called phosphorescence, is allowed and its probability is proportional to the transition probability from the singlet state S_1 to the ground state S_0 without spin-orbit coupling. For a central field potential, the strength of the spin-orbit coupling is proportional to Z^8 where Z is the atomic number of the atom [53]. Because of this strong dependence of the phosphorescence on the atomic number of the atom, organometallic

complexes with a heavy metal such as iridium, platinum or osmium typically exhibit good phosphorescence and are used in OLEDs [54].

In addition to phosphorescence, the mixing of singlet and triplet character of the excited states in spin-orbit coupling is also responsible for transitions between the lowest excited singlet state S_1 and the lowest excited triplet state T_1 , the so-called intersystem crossing. Since the energy of T_1 is generally lower than the energy of S_1 (Hund's rule), it can be beneficiary for an excited singlet state to relax to the ground state through intersystem crossing to the triplet state followed by phosphorescent emission instead of a fluorescent relaxation. A diagram of the discussed radiative and nonradiative transitions is shown in Figure 2.7.

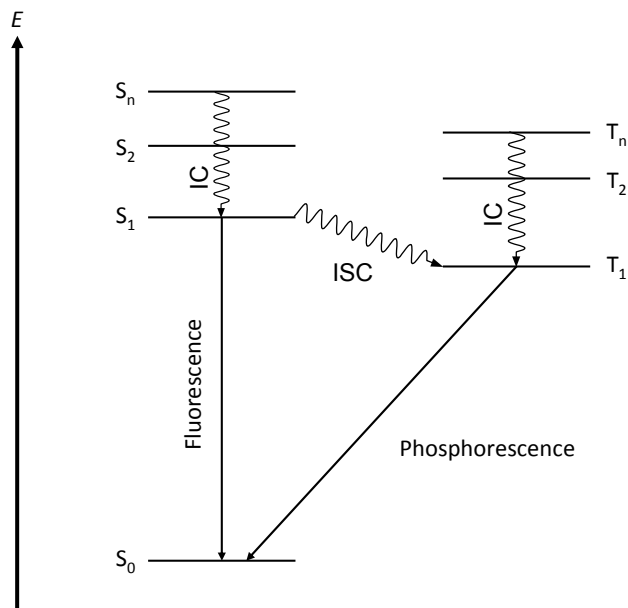


Figure 2.7. Jablonski diagram of electronic singlet and triplet states and possible transitions between these states. Solid arrows represent radiative transitions, curvy lines show nonradiative transitions from higher excited states to the lowest excited state (internal conversions, IC) and the nonradiative transition from the lowest singlet to the lowest triplet state (intersystem crossing, ISC).

2.2.7 Energy Transfer from Host to Guest

In phosphorescent devices, some of the lowest excited triplet states T_1 can be lost through the so-called triplet exciton fusion or triplet-triplet annihilation. When two triplets with the energy of T_1 collide, the energy of one excited state is transferred to the other excited state, which results in the loss of an excited state [25, 55]:



where S_n or T_n denote a higher excited singlet or triplet state.

Because of this quenching mechanism, it is not efficient to make OLEDs with emitting layers that consist solely of phosphorescent complexes. Hence, a small amount of phosphorescent complexes is typically doped into a host material that acts as a buffer layer between the phosphorescent complexes [56]. However, for a high probability of radiative transitions on the phosphorescent complex, good energy transfer from the host to the guest molecule is necessary. The energy transfer in such host-guest systems can be explained by either the Förster or the Dexter mechanism.

The Förster mechanism, also called the Coulomb mechanism, represents the classical interaction between charge distributions or, in first approximation, the interaction between two electrical dipoles. The probability of Förster energy transfer decays with R^{-6} where R is the distance between the molecules, and dipole interactions up to a distance of 10 nm can be expected [57]. Since the dipole operator does not interact with the spin, spin conservation of the molecules is required, which leads to a singlet transfer

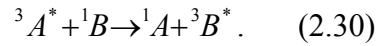


where the superscript 1 denotes a singlet state and the star marks an excited state.

Dexter transfer is also called exchange interaction and is a purely quantum mechanical phenomenon that requires the overlap of the orbitals in which the energy transfer occurs. For the exchange interaction, the total spin of both molecules before and after the process has to prevail, which leads to processes with spin conservation of the molecules



and to processes with spin transfer between the molecules:



However, since the probability of the exchange interaction decreases exponentially with increasing molecular distance and is occurring over distances of 1 nm [57], singlet-singlet transfers as shown in equation (2.28) and (2.29) are dominated by Förster transfers. Both energy transfer mechanisms are shown in Figure 2.8.

It should be noted that the Dexter energy transfer is dominant in host-guest systems such as CBP:Ir(ppy)₃ [58]. Also, note that for efficient devices, it is important that the host has good charge-transport properties to move charges from the electrodes to the emissive complexes, but it is even more important that the singlet and triplet energy level in the host are higher than the triplet level in the emissive complex to support good charge transfer from the host to the emissive complex.

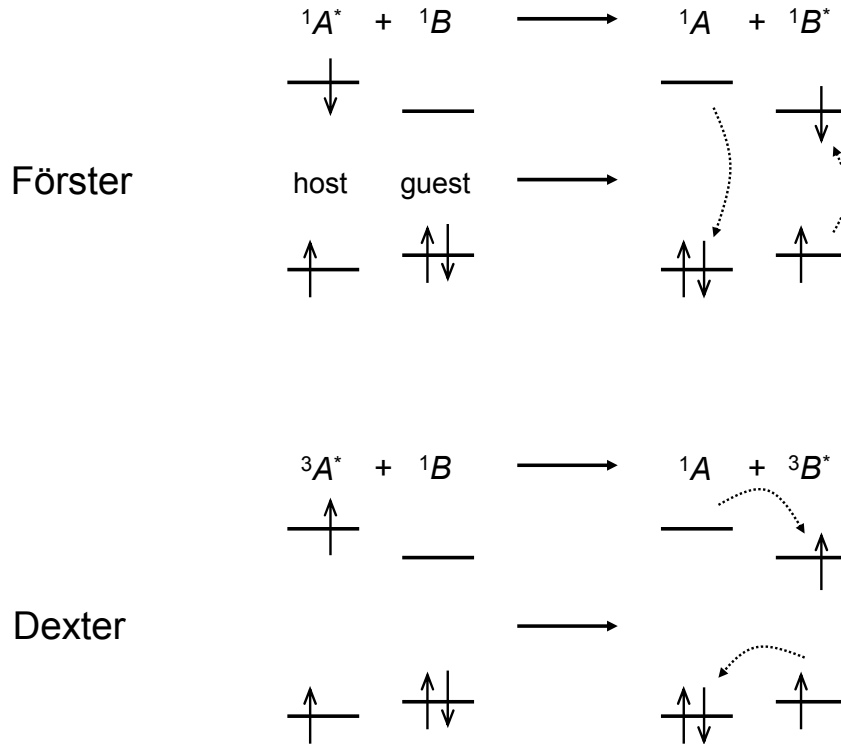


Figure 2.8. Förster (top) and Dexter (bottom) energy transfer in a host-guest system. The arrows denote electrons with the direction of their spin.

2.3 OLED Efficiency

The most often reported figure of merit for an OLED is its external quantum efficiency (EQE). The EQE is defined as the ratio between the number of photons emitted from the surface of an OLED divided by the number of injected electrons. The external quantum efficiency η_{ext} can also be written as the product of the internal quantum efficiency η_{int} (number of photons emitted in the organic material divided by number of electrons injected) times the out-coupling efficiency η_{ph} [59]:

$$\eta_{ext} = \eta_{int}\eta_{ph} \quad (2.31)$$

where the internal quantum efficiency is dependent on the device architecture and the material properties of the OLED:

$$\eta_{int} = \gamma\eta_{ex}\Phi_p \quad (2.32)$$

with γ the electron-hole charge-balance or Langevin recombination factor, η_{ex} the efficiency of the formation of excited electronic states that lead to radiative transitions, and Φ_p the photoluminescence quantum yield.

The photoluminescence quantum yield Φ_p is a material constant that describes the ratio between the number of radiative transitions and the number of total transitions from the excited states to the ground state in a material. Similarly, the efficiency η_{ex} is dependent on the material and is given by the nature of the emission. As has been shown above, radiative transitions in fluorescent devices only occur from the singlet excited state, and it is therefore expected from spin statistics that η_{ex} has an upper limit of 25% since only one out of four excited states is a singlet state, which has been confirmed in experiments on small molecules [60]. It has to be noted, however, that η_{ex} can exceed this limit in polymers where experiments suggested that up to 60% of excited states were singlet excited states [61], which has been attributed to a faster decay of higher excited singlet states to the lowest excited singlet state compared to triplet excited states in compounds with a longer chain length [51, 62]. In phosphorescent devices on the other hand, all three triplet states participate in the light emission. Additionally, since the singlet excited state has higher energy than the triplet excited state, singlets can relax into the triplet state through intersystem crossing, and therefore, $\eta_{ex} = 100\%$ can be achieved [59].

Unlike these first two parameters, γ and η_{ph} can be partially controlled in the design of the device architecture. The optimization of these two parameters and their limits are explained in the following two subsections.

2.3.1 OLED Device Architecture

The simplest device structure for an OLED is the so-called single-layer device where only one organic material is placed between the two electrodes (see Figure 2.9). It seems obvious that the efficiency for such a device architecture is the highest if the number of holes and electrons in the device are equal, such that potentially every charge has a countercharge with which it can recombine [63, 64]. If either charge occurs more often in the organic layer, it is likely that these charges will not recombine before they get extracted at the opposite electrode, and therefore γ and the efficiency of the device are decreased. Charge balance can be achieved by adjusting the injection energy barrier for the minority or majority carriers [65, 66], or by blending the organic layer with materials that support the charge transport of the minority carriers [63, 67].

However, even with optimized charge balance in a single-layer OLED, it is not very likely that all charges will recombine. Instead, some charges are able to travel to the opposite electrode, and efficiencies in single-layer devices are therefore typically low [68]. However, great improvement of the efficiency can be achieved by adding a hole-blocking layer (HBL) between the emissive layer and the cathode. Because of its high ionization potential, the hole-blocking layer inhibits holes from traveling all the way to the cathode, which leads to a higher recombination probability of the accumulated charges at the interface between the emissive layer and the hole-blocking layer [69].

Similarly, a hole-transport material with low electron affinity can be placed between the emissive layer and the anode as an electron-blocking layer (EBL, Figure 2.9) [68]. For very high efficiencies, even more complex multilayer structures with up to six different layers have been used [70].

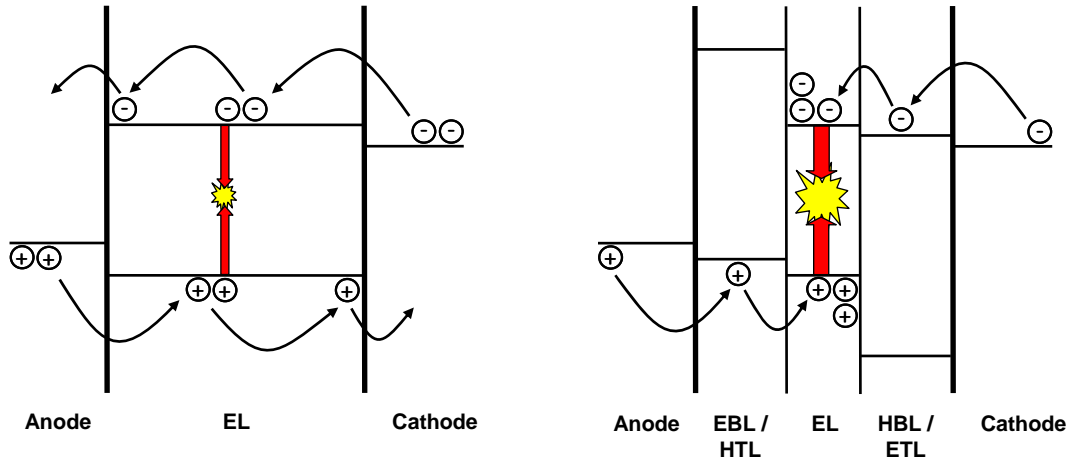


Figure 2.9. Single-layer (left) and multilayer (right) OLED device architecture with electron-blocking layer (EBL), hole-transport layer (HTL), emissive layer (EL), hole-blocking layer (HBL), and electron-transport layer (ETL).

2.3.2 Light Outcoupling

Typically, OLEDs are fabricated on glass substrates that are coated with an indium tin oxide (ITO) layer, which acts as a transparent and conductive electrode. Organic layers are then deposited on the substrates, and the devices are capped with a metal cathode. Since the light is extracted through the glass substrate, such devices are usually referred to as bottom-emitting OLEDs (see Figure 2.10). However, it turns out

that this device geometry is not very efficient in coupling out the generated light through the substrate and into the viewer's eyes.

Assuming that the cathode acts as a perfect mirror, an estimation of the maximum light output of the bottom-emission geometry can be calculated from simple ray theory. The amount of light energy transmitted from a medium 1 with refractive index n_1 into a medium 2 with refractive index n_2 normalized by the light energy incident on the interface between medium 1 and 2 is given by [71, 72]

$$\eta_{ph} = 1 - \sqrt{1 - \left(\frac{n_2}{n_1}\right)^2} \approx 0.5 \left(\frac{n_2}{n_1}\right)^2 \quad (2.33)$$

This equation holds even for multilayer structures as long as there is no local minimum of the refractive index within the multilayer structure [73]. With a refractive index of the organic material $n_{organic} = 1.8$ [74] and with $n_{air} = 1$, an outcoupling efficiency η_{ph} of approximately 15% can be calculated. This value is only a crude approximation of the outcoupling efficiency, but even more involving calculations resulted in only slightly higher outcoupling efficiencies between 20 and 25% for thin-film devices on top of ITO coated glass substrates [71, 75].

There have been some research studies on improving the outcoupling efficiency of bottom-emitting OLEDs [76-81]. In most reports, the emitting surface of the glass substrate is manipulated to avoid internal total reflection between glass and air [77, 79, 80]. Alternatively, the ITO to glass interface is modified to avoid waveguiding effects in the ITO [73, 78, 81]. Outcoupling improvements of up to 300% have been measured [78]. However, it has to be noted that such improvements occur mostly in the direction perpendicular to the glass substrate. Whereas basic bottom-emitting OLEDs have the

same intensity independent of the observer's angle (Lambertian emitter), geometries with improved outcoupling are typically not Lambertian [78].

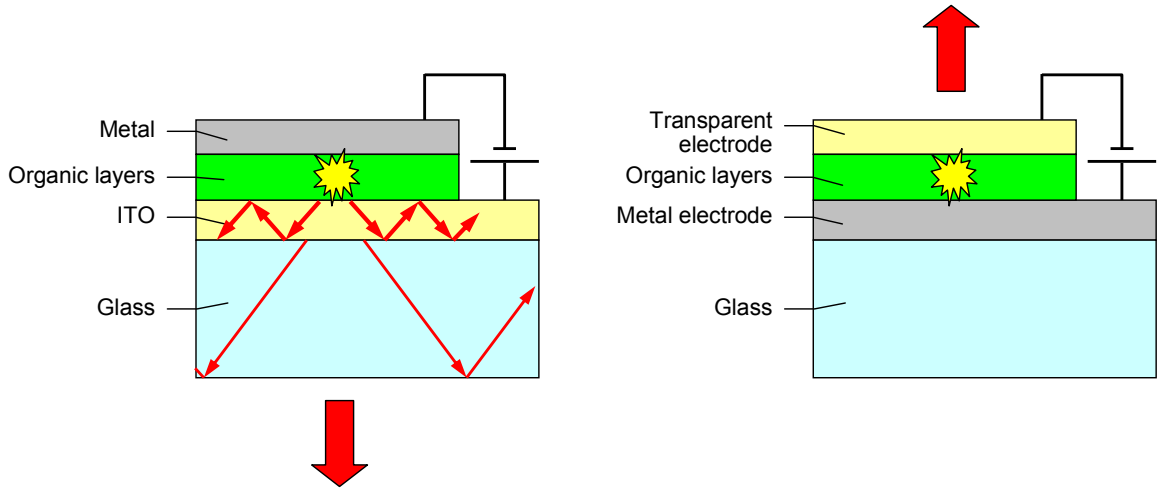


Figure 2.10. Bottom-emitting (left) and top-emitting (right) OLEDs. Small arrows in the bottom-emitting OLED represent light that is waveguided in the ITO or in the glass.

In a completely different approach, top-emitting OLEDs have been proposed to avoid waveguiding effects in the ITO layer and the glass substrates [82, 83]. Top-emitting OLEDs are fabricated on metal coated substrates that fully reflect the light, while the top electrode, the cathode, is transparent. However, the EQE of top-emitting OLEDs seems to be limited to about 20 to 25% as well [84], which has been attributed to surface plasmon-polariton modes that occur at the metal surfaces [85].

CHAPTER 3

EXPERIMENTAL METHODS

3.1 OLED Test Setup

Current-voltage (I-V) measurements were made using a Keithley 2400 sourcemeter where the current was measured as a function of the applied voltage. Simultaneously, by placing the OLED substrate behind a quartz window, the light output of the device was measured using a calibrated photodiode (FDS 100 from Thorlabs, Inc.). The generated photocurrent was converted into a voltage by a current-to-voltage converter with an Analog Devices 549LH operational amplifier and a resistor R of $5\text{ M}\Omega$ (Figure 3.1). In such a converter, the output voltage V_{det} is related to the photocurrent I_{det} according to Ohm's Law:

$$V_{det} = RI_{det} \quad (3.1)$$

The output voltage from the light power measurement was read by a computer using a digital acquisition board (DAQPad 6020E from National Instruments). The light and current measurements were implemented in a LabView program for simultaneous testing. The whole current-voltage test setup is shown in Figure 3.1. The testing was done immediately after the deposition of the metal cathode onto the organic layers of the OLED in a nitrogen atmosphere without exposing the devices to air.

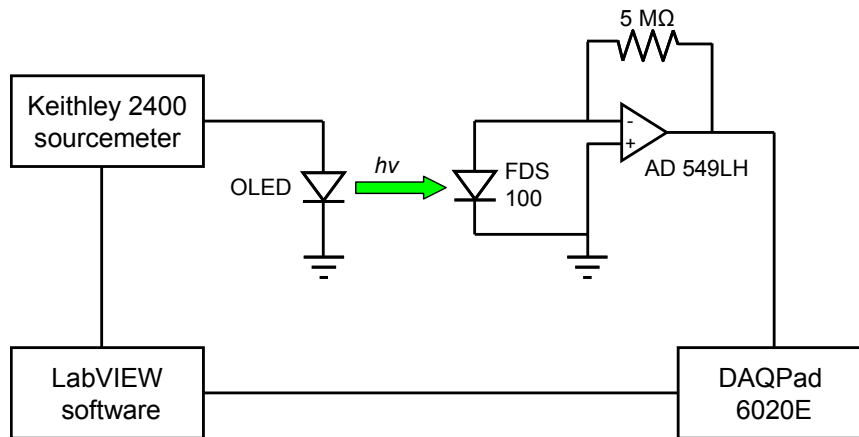


Figure 3.1. Illustration of the current-voltage test setup.

3.2 Electroluminescence Spectra Measurements

Similar to the current-voltage measurements, the OLED substrate was placed behind a quartz window and a voltage was applied using the Keithley sourcemeter. The electroluminescence spectra in the visible region were then measured by an Oceanoptics spectrometer USB 4000. By implementing the spectrometer measurements and the voltage control in a LabView program, spectra could be measured as a function of the applied voltage to ensure that no changes of the spectra occurred with increasing voltage.

3.3 CIE Spectral Coordinates

To categorize colors, the International Commission in Illumination (CIE) in 1931 created a color space that addresses an (x,y) coordinate to any color spectrum [16]. This color space is based on the color perception of the eye where three different kinds of receptors are used to register the light in the long, middle, and short wavelength ranges

[86]. Each test color can therefore be described by how much its spectrum overlaps with the response spectra of each of the receptors, which results in the tristimulus values. Likewise, the CIE color space is based on three color-matching functions, one in the red (\bar{x}), one in the green (\bar{y}), and one in the blue (\bar{z}) as shown in Figure 3.2.

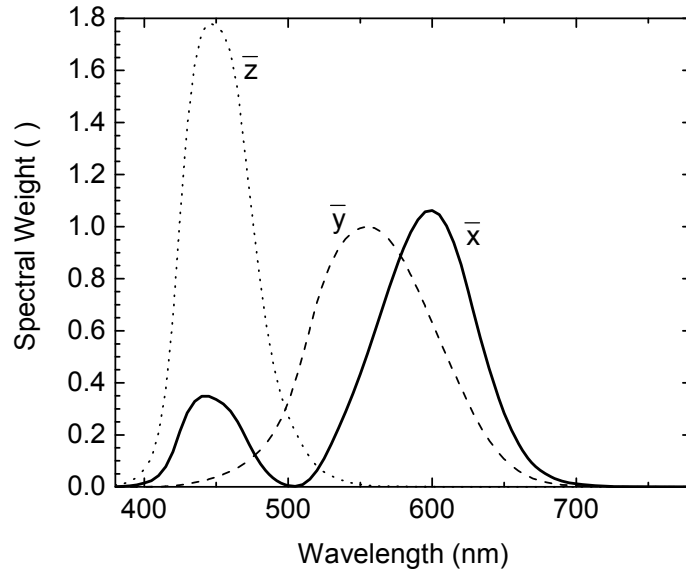


Figure 3.2. Color-matching functions \bar{x} , \bar{y} , and \bar{z} as a function of the wavelength.

The tristimulus value X that represents the spectral overlap between the color-matching function \bar{x} and the test color is then calculated from

$$X = \int S_{TEST}(\lambda)\bar{x}(\lambda)d\lambda \quad (3.2)$$

where S_{TEST} is the test spectrum. The tristimulus values Y and Z are calculated in the same manner. Normalizing the tristimulus values of any test color to

$$x = \frac{X}{X+Y+Z} \quad (3.3)$$

and likewise for the y coordinate results in the chromaticity diagram shown in Figure 3.3.

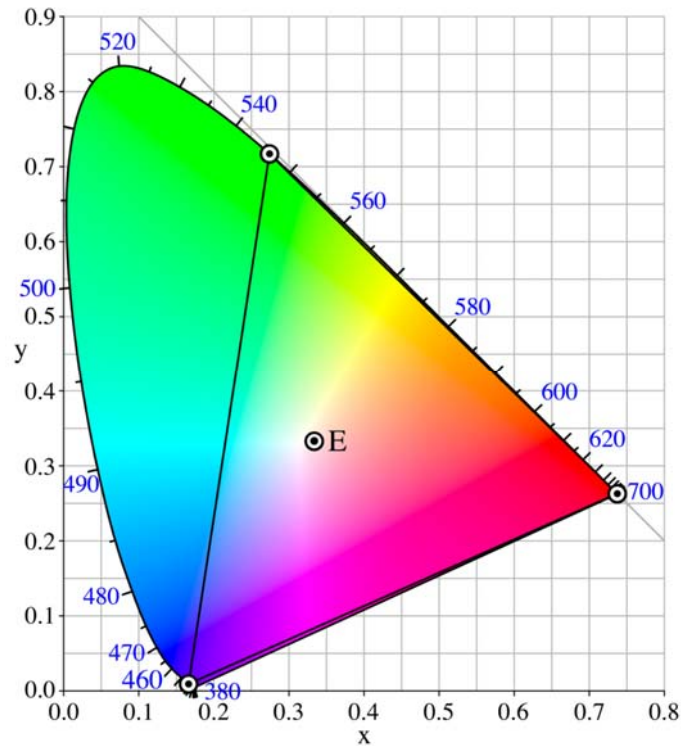


Figure 3.3. CIE 1931 chromaticity diagram. The outer curved boundary is delimited by monochrome light with the according wavelengths in nanometers. The corners of the triangle represent the RGB primary colors, and E marks the equal energy point corresponding to a constant energy distribution in the visible wavelength range.

In display applications, colors are generally achieved by additive mixing of the light that is emitted from red, green and blue (RGB) pixels. The CIE color coordinates for the RGB primary colors in CIE are (0.73, 0.27), (0.27, 0.72), and (0.17, 0.01), respectively, which corresponds to monochromatic light with a wavelength of 700 nm, 546.1 nm, and 435.8 nm, respectively.

3.4 Luminance Calculation

Since OLED displays are ultimately designed for the human eye, the light output of such devices is not measured in radiometric units (i.e. watt), but in photometric units (i.e. candela). Photometric units are always weighed in response to the photopic sensitivity function, which is the response of the human eye (see Figure 3.4). The radiated power of light-emitting diodes is therefore reported as the luminance in cd/m^2 , which describes the amount of light that is emitted from an area of 1 m^2 and falls into a given solid angle.

With Φ_v the luminous flux per watt:

$$\Phi_v = 683 \frac{\text{lumen}}{\text{watt}} \int S_{ph}(\lambda) \times S_{OLED}(\lambda) d\lambda \quad (3.4)$$

where S_{ph} is the photopic response and S_{OLED} is the normalized spectrum of the OLED, and with R_{det} the weighed detector response:

$$R_{det} = \int S_{det}(\lambda) \times S_{OLED}(\lambda) d\lambda \quad (3.5)$$

where S_{det} is the response of the detector as shown in Figure 3.4, we can calculate the luminance L as

$$L = \frac{V_{det}}{R \cdot R_{det}} \frac{\Phi_v}{A} \frac{d^2}{A_{det}} \quad (3.6)$$

where R is the resistor in the current-to-voltage converter at the calibrated photodiode (as shown in section 3.1), V_{det} is the measured output of the detector circuit, A is the area of the device, d is the distance between the device and the detector, and A_{det} is the area of the detector. The first term in the equation for the luminance describes the power that is

measured by the photodiode, while the last term is the inverse of the solid angle assuming that the OLED can be approximated as a point source from the view of the detector.

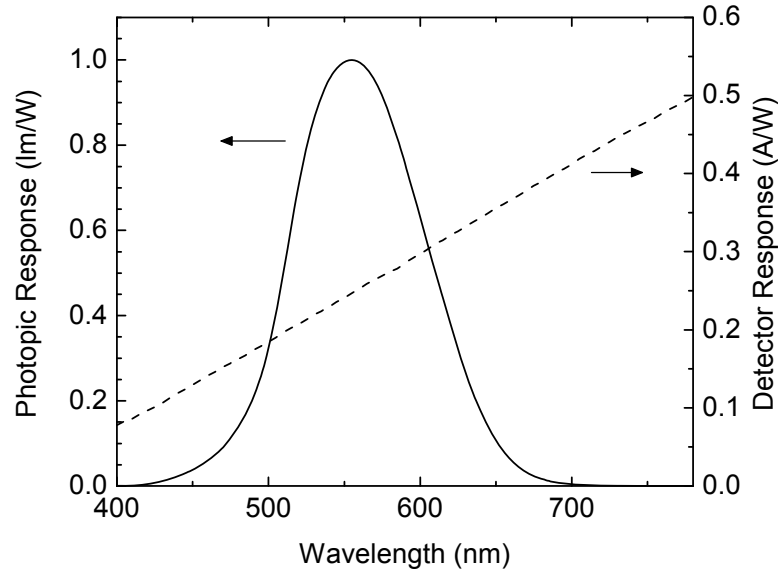


Figure 3.4. Photopic (S_{ph}) and detector (S_{det}) response as a function of the wavelength in the visible range.

3.5 OLED Efficiency Calculation

As mentioned above (section 2.3, page 30), the external quantum efficiency (EQE) describes the number of photons that are emitted in the forward viewing direction divided by the number of electrons that are injected into the diode. Therefore, to calculate the EQE, the measured spectral light output first has to be converted into the number of photons n_{ph} per unit of energy:

$$n_{ph} = \frac{1}{hc} \int S_{OLED}(\lambda) \lambda d\lambda \quad (3.7)$$

where h is the Planck constant and c is the speed of light. Assuming a Lambertian emitter, we can then calculate the EQE as

$$EQE = \frac{V_{det}}{R \cdot R_{det}} n_{ph} \frac{q \pi d^2}{I A_{det}} \quad (3.8)$$

where I is the measured current and q is the elementary charge. The last term in this equation yields the total emitted light for a Lambertian emitter.

The current efficiency L_{eff} , which is given in cd/A and is similar to the external quantum efficiency but also includes the photopic response, can be calculated directly from the luminance L and the current density J as

$$L_{eff} = \frac{L}{J} \quad (3.9)$$

CHAPTER 4

HYBRID ELECTROPHOSPHORESCENT OLEDs WITH A SOLUTION-PROCESSED HOLE-TRANSPORT LAYER

4.1 State-of-the-Art High-Efficiency OLEDs

As has been mentioned before, there has been a strong interest in electrophosphorescent OLEDs recently because singlet and triplet excited states can contribute to light emission, which can lead to an internal quantum efficiency of 100%. In one of the first reports of an electrophosphorescent OLED, Baldo *et al.* used the green phosphorescent emitter *fac* tris(2-phenylpyridinato-N,C^{2'}) iridium (Ir(ppy)₃, Figure 4.1) as the emissive complex and obtained an external quantum efficiency (EQE) of 7.5% (26 cd/A) at 100 cd/m² [56]. Their device structure consisted of 4,4'-bis[N-(1-naphthyl)-N-phenyl-amino]biphenyl (α -NPD) as a hole-transport layer (HTL), 4,4'-di(carbazol-9-yl)-biphenyl (CBP) as a host for Ir(ppy)₃, 2,9-dimethyl-4,7-diphenyl-1,10-phenanthroline (BCP) as a hole-blocking layer, and tris-(8-hydroxyquinolino-N,O) aluminum (Alq₃) as an electron-transport layer (Figure 4.1). The device was capped with a Mg:Ag cathode.

Generally, OLEDs show higher efficiencies when alkali metal compounds, especially lithium compounds, are used as a buffer layer between the organic layers and the cathode [65, 87]. Such buffer layers enhance electron injection, which leads to lower turn-on voltages and higher efficiencies because of a better charge balance in the device. For example, Tsutsui *et al.* have been able to improve the performance of the previously mentioned devices by using a Li₂O/aluminum cathode instead of the Mg:Ag cathode [88]. External quantum efficiencies of 13.7% at 105 cd/m² were measured.

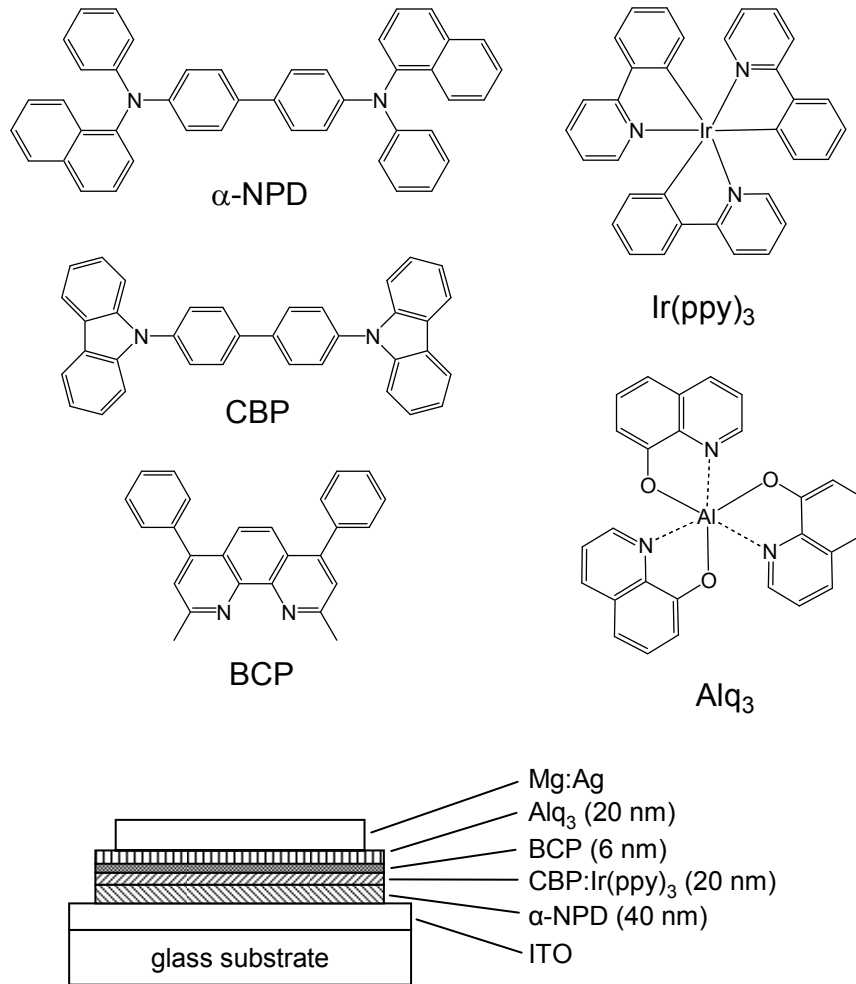


Figure 4.1. Chemical structures of α -NPD, CBP, BCP, Ir(ppy)₃, and Alq₃ (top), and the device structure of the first efficient devices reported by Baldo *et al.* [56] (bottom).

Since then, several teams have modified the device architecture and the nature of the materials in those devices to improve efficiency, light output, and turn-on voltage [59, 68, 70, 89-91]. Most commonly, different host-guest materials have been used to improve the energy transfer from the host to the guest [59]. J. Kido *et al.*, on the other hand, demonstrated higher efficiencies by introducing a doped hole transport layer for better hole injection [90] and by using hole- and electron-blocking materials with larger energy

barriers for better confinement of the excitons in the emissive layer [89]. Combinations of these methods have also been reported [68, 70, 91]. Most of the cited references report efficiencies of up to 19% for optimized devices while Kido *et al.* reach efficiencies of up to 29% [89]. However, the most efficient devices (higher than 20% EQE) are based on complex device structures with at least four organic layers, three of which are deposited from the vapor phase. As mentioned earlier (chapter 1.4, page 5), the rather slow deposition rate of organic layers ($\sim 1 \text{ \AA/s}$) can be a limiting factor in the manufacturing cost of such devices. Therefore, device geometries in which fewer organic materials and fewer layers are deposited from the vapor phase and in which high efficiency is maintained are desirable.

4.2 Ionization Potential Study

In this chapter, it will be shown that the efficiency of phosphorescent OLEDs based on the well-known host-guest matrix CBP:Ir(ppy)₃ can be significantly improved by tuning the ionization potential (I_p) and the hole-mobility (μ_h) of the hole-injection/transport layer. In addition, the device structure is simplified by using a wet-processable material and by reducing the number of subsequent evaporated layers without compromising the performance. For this study, a series of crosslinkable side-chain copolymers based on *N,N'*-bis(*m*-tolyl)-*N,N'*-diphenyl-1,1'-biphenyl-4,4'-diamine (TPD) was used as the hole-transport layer [92]. The ionization potential of these copolymers can easily be tuned by using differently substituted TPD side-chain moieties (Figure 4.2. Structure of crosslinkable TPD-based copolymers.). The estimated ionization potential of these TPD copolymers (**P1** to **P4**) ranges from 5.2 eV to 5.5 eV while the

hole mobilities, characterized by the time-of-flight technique at an applied electric field of 4×10^5 V/cm at room temperature, decrease from 1.8×10^{-5} to 5.9×10^{-7} cm²/Vs [93]. To complete the study, poly(*N*-vinyl-carbazole) (PVK) which has a higher ionization potential of 5.8 eV [94] and a lower mobility in the range of 10^{-8} to 10^{-7} cm²/Vs [95] was also tested. The TPD-based copolymers were synthesized by the group of Prof. Seth Marder of the School of Chemistry and Biochemistry at the Georgia Institute of Technology.

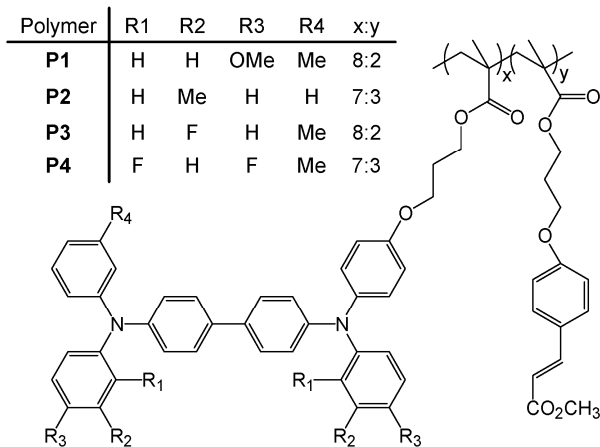


Figure 4.2. Structure of crosslinkable TPD-based copolymers.

For the fabrication of the devices, TPD-copolymer films of 35 nm thickness (25 nm for PVK) were spin-coated from toluene onto air-plasma treated ITO coated substrates in an inert nitrogen atmosphere. Air-plasma treatment of ITO increases the workfunction of the anode and therefore reduces the energy barrier for hole-injection into the organic semiconductor [96, 97]. The TPD-copolymer films were crosslinked for one minute under a broadband UV-light with 0.7 mW/cm² power density. The substrates were

then loaded into a Kurt J. Lesker Spectros vacuum system without being exposed to atmosphere. For all subsequent organic layers, materials were first purified using gradient zone sublimation and were then thermally evaporated at a rate of 1 Å/s at a pressure below 1×10^{-7} Torr on top of the hole-transport layers. For the emitting layer, a concentration of 6% Ir(ppy)₃ was co-evaporated into a 20 nm-thick film of CBP. A 6 nm-thick layer of BCP was used as a hole-blocking layer, followed by a 20 nm-thick layer of Alq₃ as an electron-transport layer. Finally, a 1 nm-thick layer of lithium fluoride (LiF) was deposited as an electron-injection layer, followed by a 200 nm-thick aluminum cathode. Schematics of the substrate cleaning and OLED fabrication processes are shown in the Appendix.

Table 4.1. Ionization potentials I_p , mobility, and triplet energy values of different hole-transport materials (HTM) and device performance at 100 cd/m² of OLEDs with device structure ITO/HTM (25-35 nm)/CBP:Ir(ppy)₃ (6%, 20 nm)/BCP (6 nm)/Alq₃ (20 nm)/LiF (1 nm)/Al.

HTM	I_p (eV)	Hole mobility ^c (cm ² /Vs)	Triplet energy (eV)	EQE (%)	Luminous efficiency (cd/A)	Power efficiency (lm/W)
P1	5.25 ^a	1.8×10^{-5}	2.48 ^d	4.0	14	7
P2	5.34 ^a	6.4×10^{-6}	2.49 ^d	10.2	35	18
P3	5.45 ^a	7.2×10^{-7}	2.51 ^d	12.0	41	17
P4	5.47 ^a	5.9×10^{-7}	2.56 ^d	14.3	49	25
PVK	5.8 ^b	4.5×10^{-7}	3.0 ^e	18.1	62	29

^acalculated from electrochemistry (see Ref. [93])

^bestimated from photoemission spectroscopy (see Ref. [94])

^cmeasured at 4×10^5 V/cm and T = 297 K. The mobilities of **P1-P4** were reported by Domercq *et al.* (see Ref. [93]). The hole mobility of PVK was measured by a time-of-flight experiment.

^dcalculated in a similar framework as Ref. [98].

^esee Ref. [99]

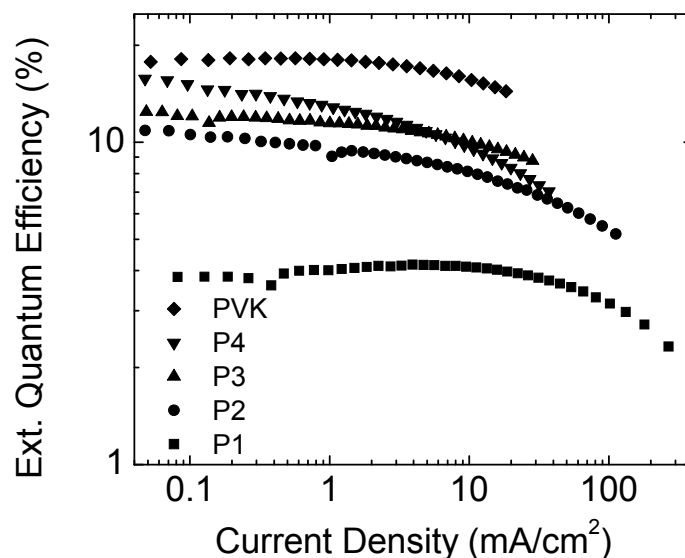


Figure 4.3. External quantum efficiencies as a function of the current density for OLEDs with device structure ITO/HTM (25-35 nm)/CBP:Ir(ppy)₃ (6%, 20 nm)/BCP (6 nm)/Alq₃ (20 nm)/LiF (1 nm)/Al.

The external quantum efficiencies (EQEs) are shown as a function of the current densities in Figure 4.3 for the devices with the five different hole-transport materials (HTM). EQE, luminous efficiency, and power efficiency at 100 cd/m² are listed in Table 4.1. While devices with **P1** ($I_p = 5.2$ eV, $\mu_h = 1.8 \times 10^{-5}$ cm²/Vs) show the lowest external quantum efficiency of 4.0% at 100 cd/m², devices with PVK ($I_p = 5.8$ eV, $\mu_h = 4.5 \times 10^{-7}$ cm²/Vs) exhibit an EQE of up to 18.1% at 100 cd/m². These results indicate that the efficiency increases with an increasing ionization potential and a decreasing hole mobility of the hole-transport material. These two effects both lead to a reduction of the

injected hole current relative to the electron current, resulting in an improved charge balance. This hypothesis is in agreement with previous studies [100-104]. However, it should also be noted that other studies do not show any relation between the ionization potential of the hole-transport material and the efficiency of the OLED [12, 105, 106].

To further investigate the observed effect, we prepared and characterized hole carrier devices with the structure ITO/HTM (25-35 nm)/CBP:Ir(ppy)₃ (6%, 20 nm)/aluminum. A significant decrease in current density was observed in devices using hole-transport materials with increasing ionization potential and decreasing hole mobility, therefore further supporting the charge balance optimization explanation (Figure 4.4).

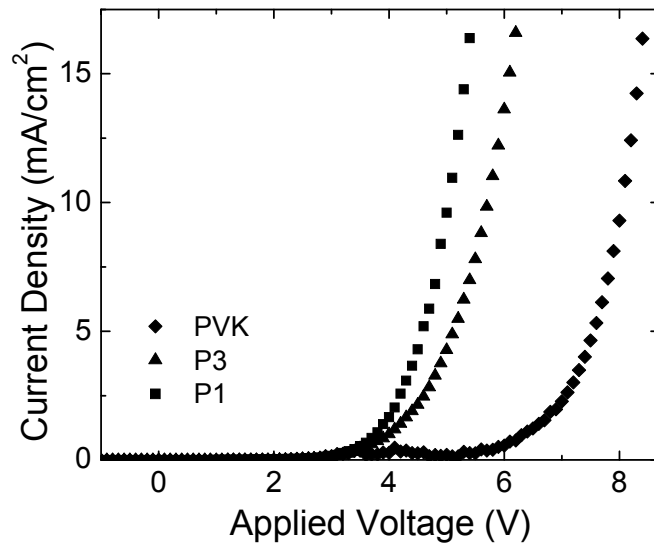


Figure 4.4. Current density as a function of the applied voltage for devices with the structure ITO/HTM (25-35 nm)/CBP:Ir(ppy)₃ (6%, 20 nm)/Al.

Nevertheless, another possible origin of the increase in device efficiency can be attributed to an increase of the triplet energy of the hole-transport material. While hole-transport materials with a low triplet energy allow nonradiative recombination through energy transfer from the emissive excited state of Ir(ppy)₃ to the triplet state of the hole-transport material, this loss mechanism can be reduced if the triplet energy of the hole-transport material is higher than that of the emissive complex [106]. As shown in Table 4.1, the calculated triplet level energies of polymers **P1** to **P4** vary only by 0.08 eV. However, their average value is close to that of Ir(ppy)₃ (2.4±0.1 eV) [107]. Hence, small variations could lead to rather big changes in efficiency. On the other hand, when using PVK with a triplet energy of 3.0 eV [99], the nonradiative loss mechanism should be significantly reduced. The triplet level energy values were estimated from theoretical calculations performed by the group of Prof. Jean-Luc Brédas of the School of Chemistry and Biochemistry at the Georgia Institute of Technology.

4.3 Simplification of the Device Architecture

For the efficient OLEDs that have been presented above with PVK as the hole-transport material, the fabrication can now be further improved by reducing the number of layers in the device architecture. It has been shown previously that BCP exhibits a higher electron mobility than Alq₃. BCP can therefore also be used as an electron-transport layer with integrated hole-blocking properties [108, 109]. Hence, we fabricated devices where the Alq₃ layer was removed and the thickness of the BCP layer was increased (see Figure 4.5, bottom). The luminance and the efficiencies as a function of the applied voltage are shown in Figure 4.5 for the devices with 3 and 4 organic layers. A

lower turn-on voltage can be observed for the devices with 3 organic layers while the efficiency at high luminance is similar to the devices with 4 organic layers. However, due to some leakage in the current at low luminance, the efficiency for the 3-layer devices is low at 100 cd/m².

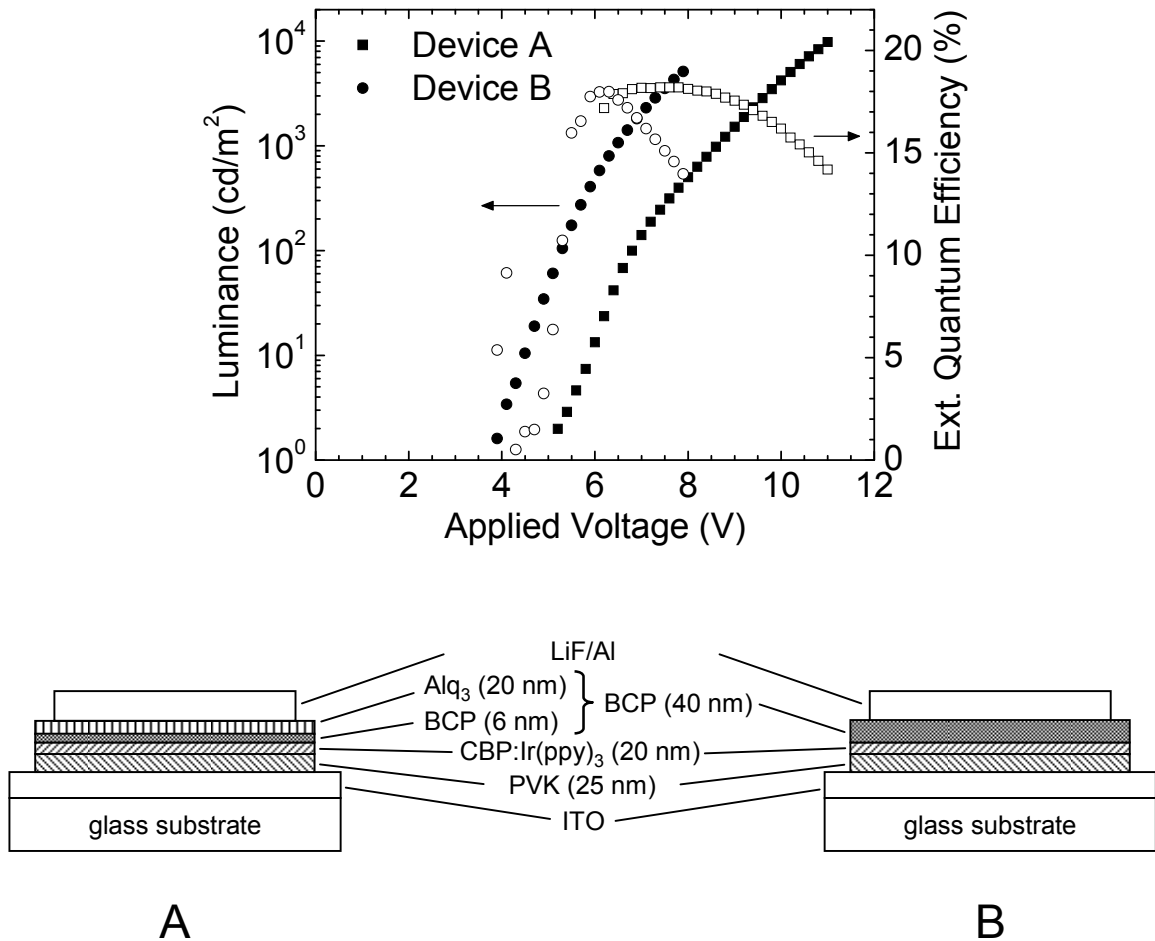


Figure 4.5. Luminance (solid shapes) and external quantum efficiency (empty shapes) as a function of the applied voltage for a device with 4 organic layers (device A, squares): ITO/PVK (25 nm)/CBP:Ir(ppy)₃ (6%, 20 nm)/BCP (6 nm)/Alq₃ (20 nm)/LiF (1 nm)/Al, and for a device with 3 organic layers (device B, circles): ITO/PVK (25 nm)/CBP:Ir(ppy)₃ (6%, 20 nm)/BCP (40 nm)/LiF (1 nm)/Al. The bottom part of the figure illustrates the different device architectures.

To reduce the leakage at low luminance, the thickness of PVK was increased to 35 nm. The slight increase in thickness resulted in a higher turn-on voltage for the new devices while the efficiency remained similar (Figure 4.6). Moreover, the electron-injection was optimized by varying the thickness of LiF. An optimized LiF thickness of 2.5 nm led to devices with external quantum efficiencies of up to 21.2% and luminous efficiencies of 72 cd/A at 100 cd/m². This is the highest efficiency achieved in a device comprised of less than four organic layers. It should also be noted that all of the materials used for this high-efficiency device are commercially available while other reports with high efficiencies typically include some specialty compounds. Furthermore, the hole-transport layer is processed from solution, which reduces the overall deposition time of the remaining two organic layers that are deposited from the vapor phase at low deposition rates (1 Å/s).

As mentioned above, only 20 to 25% of the light emission can theoretically be collected in the forward direction of a bottom-emitting OLED due to total internal reflection effects in the device [73, 75]. The high efficiencies measured in this study therefore suggest that we obtain an internal quantum efficiency close to 100%.

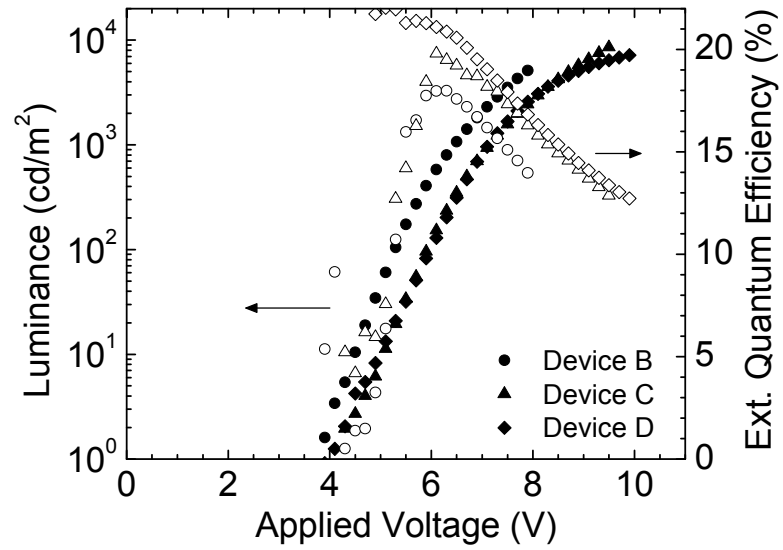


Figure 4.6. Luminance (solid shapes) and external quantum efficiency (empty shapes) as a function of the applied voltage for device B (circles): ITO/PVK (25 nm)/CBP:Ir(ppy)₃ (6%, 20 nm)/BCP (40 nm)/LiF (1 nm)/Al, for device C (diamonds): ITO/PVK (35 nm)/CBP:Ir(ppy)₃ (6%, 20 nm)/BCP (40 nm)/LiF (1 nm)/Al, and for device D (triangles): ITO/PVK (35 nm)/CBP:Ir(ppy)₃ (6%, 20 nm)/BCP (40 nm)/LiF (2.5 nm)/Al.

CHAPTER 5

HYBRID ELECTROPHOSPHORESCENT OLEDs WITH SOLUTION-PROCESSED HOLE-TRANSPORT AND EMISSIVE LAYERS

5.1 Introduction

While high efficiencies were first achieved in vacuum-deposited OLEDs [56, 59, 88], only recently have comparable efficiencies been measured in devices with solution-processed emissive layers [68, 110]. The performance of solution-processed devices has been increased using various approaches, such as synthesizing dendrimers of phosphorescent complexes to provide site isolation of the emissive material and therefore reduce triplet-triplet annihilation [110, 111], molecularly doping a hole-transport polymer with phosphorescent complexes and an electron-transport material [68, 112, 113], or synthesizing copolymers that combine all these properties [114-116].

Independently of the emissive layer, it has been shown that OLED efficiencies increase if a hole-transport/electron-blocking layer is used between the anode and the emissive layer, as explained in section 2.3.1, page 32 [68, 117-120]. However, the fabrication of solution-processed multilayer stacks is not straightforward since previously processed layers have to be insoluble in the solvent of the subsequent layer.

In this chapter, the fabrication of solution-processed multilayer structures will be explained first. Then, the two most successful fabrication methods for solution-processed emissive layers to date, molecularly doped layers and emissive layers based on

dendrimers, will be discussed and the state of the art in such devices will be shown. Next, the problems of such mixed layers will be mentioned and our approach of a copolymer-based emissive layer will be presented. Finally, devices based on copolymers with different colors will be shown where the copolymer with an orange electroluminescence spectrum will be optimized for highest efficiencies in an OLED structure.

5.1.1 Solution-Processed Multilayer Stacks and Crosslinking

Multilayer structures can easily be achieved with small molecules in vacuum deposition. However, the device fabrication for solution-processed multilayer OLEDs is more complicated since it is necessary that the previously deposited layer does not dissolve when the next layer is deposited. In general, there are four different methods to achieve multilayer stacks from solution [121]. First, layers can be processed from a precursor that turns insoluble upon heating [122]. Alternatively, orthogonal solvents can be used for neighboring layers where the solvent of the second layer does not dissolve the previously deposited material [69, 112, 123]. Furthermore, films can also be made insoluble by crosslinking [100, 124-129]. Finally, an intermediate liquid buffer layer can be used that does not dissolve the previous layer, but protects it from the solvent of the subsequent layer [130]. In the present work, crosslinking has been used for the fabrication of solution-processed multilayer devices since it does not impose any restriction on the choice of solvent for the following layer.

In the crosslinking process, enough energy has to be supplied to the material such that chemical bonds on the specific crosslinking groups can rearrange to make a link between separate molecules or polymers, which creates a network of connected

molecules or polymers that can no longer be dissolved. Crosslinking of polymers can be achieved thermally or optically. In this work, optical crosslinking will be used for solution-processed multilayer depositions because of its additional advantage that devices can be patterned during crosslinking using photolithography [100]. In fact, fully solution-processed multicolor displays based on fluorescent organic materials have already been demonstrated using photocrosslinkable materials [131, 132].

5.1.2 Molecularly Doped OLEDs

Most of the research in electrophosphorescent OLEDs with solution-processed emissive layers has been done on molecularly doped OLEDs. In this approach, a solution of a charge transport polymer (hole- or electron-transport) is doped with a phosphorescent dye and possibly other materials. Layers that are processed from these mixed solutions typically show properties of all the materials combined. With the growing commercial availability of small molecules for organic electronic applications, materials for molecularly doped OLEDs can be acquired easily whereas materials for the dendrimer and the copolymer approach have to be synthesized first.

As has been shown in chapter 3, Ir(ppy)₃ doped into CBP can lead to high efficiencies. Therefore, poly(N-vinyl-carbazole) (PVK) as a close relative of CBP is an obvious candidate as a host for the same emissive complex. Hence, the combination of PVK and Ir(ppy)₃ was used in the first molecularly doped OLEDs [133]. To increase and optimize the efficiency, a thermally evaporated hole-blocking/electron-transport layer had to be deposited between the molecularly doped layer and the cathode, and external quantum efficiencies of up to 7.5% at 100 cd/m² were observed.

However, later studies have shown that the efficiency improves significantly if an electron-transport material, such as 2-(4-biphenyl)-5-(4-*tert*-butylphenyl)-1,3,4-oxadiazole (PBD, Figure 5.1), is blended into the emissive layer [63, 134]. The electron-transport material increases the number of electrons in the emissive layer to balance the number of holes, which leads to a higher recombination rate. Efficiencies of up to 8.5% at 100 cd/m² were reported for devices with an emissive layer consisting of PVK, Ir(ppy)₃ and PBD [69].

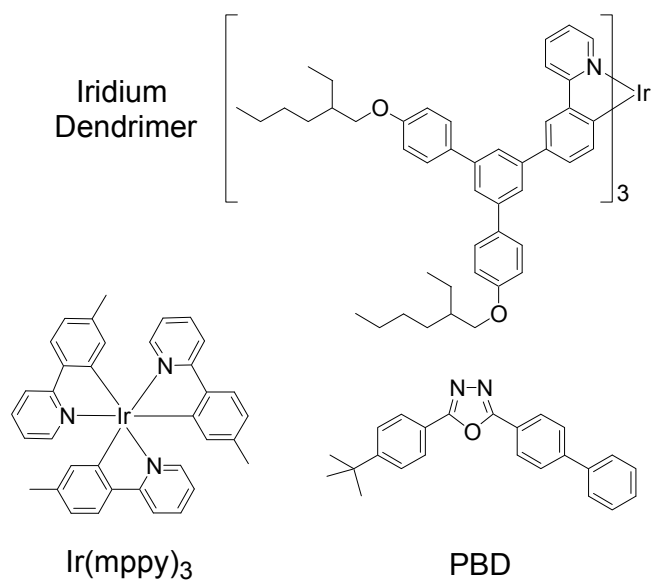


Figure 5.1. Chemical structure of Ir(mppy)₃, PBD, and the dendrimer reported by Lo *et al.* [110].

Nevertheless, external quantum efficiencies of optimized molecularly doped OLEDs based on the phosphorescent emitter Ir(ppy)₃ typically do not exceed 10% with the exception of one report by Kim *et al.* where 15.5% EQE was measured at 100 cd/m² in an OLED that consisted of just one molecularly doped layer in a single-layer device

architecture [112]. It has been shown that this upper limit is caused by aggregation and phase separation of the Ir(ppy)₃ molecules in the emissive layer that lead to triplet-triplet annihilation and therefore to lower efficiencies [135]. Adding alkyl substituents to the ligands of the complex, however, has been shown to improve the interaction between the emissive complex and the polymer matrix, leading to a better solubility and to a more homogeneous distribution of the phosphorescent dye [136, 137]. Hence, record-high efficiencies for OLEDs with a solution-processed emissive layer have been reported using Ir(mppy)₃ (Figure 5.1) [68].

5.1.3 Dendrimers

In an attempt to combine charge-transport and emission on the same molecule, fluorescent and phosphorescent dendrimers have been reported [111]. Dendrimers are large molecules that consist of a core and of branches, called dendrons (see Figure 5.1). Phosphorescent dendrimers typically have a core that consists of a heavy metal atom that is surrounded by some charge transport units with good solubility. By adjusting the length of the dendrons, the probability of interactions between the molecules can be decreased and the triplet-triplet annihilation is lowered. Nevertheless, the external quantum efficiencies of OLEDs with solution-processed dendrimer emissive layers and thermally evaporated hole-blocking layers just barely exceeded 10%, which was attributed to low charge balance in the dendrimer layer [111, 138]. Therefore, to date, dendrimers have to be blended with an additional charge-transport material, a hole-transport material for the cited references, to achieve good charge balance, similar to

molecularly doped OLEDs [110, 139]. Using a dendrimer blend and an evaporated hole-blocking layer, EQEs of up to 16% at 100 cd/m² have been measured [110].

5.1.4 Emissive Layers from Copolymers

In a different approach, clustering of the organometallic complexes can potentially be circumvented by incorporation of the host material and the organometallic phosphorescent complex in a copolymer. By choosing the right synthetic methodology, it is possible to fabricate copolymers that are derived from monomers with specified functionalities, such as phosphorescent emission, hole and electron transport, or crosslinking properties. Furthermore, in contrast to many guest-host approaches, copolymers may be less subject to morphological changes, such as phase separation and crystallization, over time. Therefore, copolymers have the potential for higher stability, especially in applications that require large light output and consequently generate heat under operational conditions. This stability at higher temperatures can also further ease packaging and processing requirements.

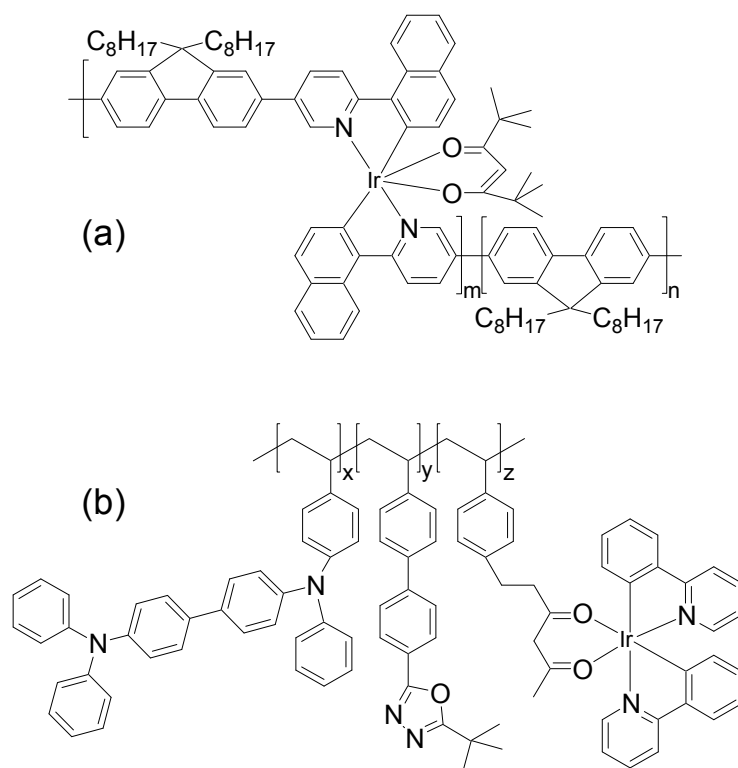


Figure 5.2. Electrophosphorescent copolymers with an iridium complex in the polymer backbone as described in [116] with $m:n = 1:99$ (a), and with an iridium complex in a side-chain of the polymer as reported in [114] with $x:y:z = 18:79:3$ (b)

OLEDs based on copolymers in which an iridium complex is directly attached to or even inserted into the polymer backbone generally exhibit low efficiencies, apart from a report by Zhen *et al.* on a red-emitting chelating copolymer that was incorporated in devices with up to 6.5% external quantum efficiency (see Figure 5.2) [116, 140, 141]. In a different approach, Evans *et al.* have demonstrated that polymers with an iridium complex attached to the polymer as a side-chain are preferable to achieve high efficiencies in OLED devices [142]. This approach has often been used in the literature, and in many cases, iridium complex units (for phosphorescent emission) and carbazole units (for hole transport) have been attached as side groups to vinyl polymer backbones

[115, 143-146]. However, the external quantum efficiencies of single-layer devices based on these copolymers rarely exceed 1%. As before, more efficient OLEDs result from devices with a thermally evaporated hole-blocking and/or electron-transport [143, 144], or as Tokito *et al.* demonstrated, from devices where a small molecule with electron-transport properties is dispersed in the copolymer [115]. However, because of the versatility that can be achieved in copolymers, electron-transport properties can also be incorporated in the copolymer directly. In fact, the highest efficiency reported for a device with an emissive layer based on copolymers resulted when all three components – the hole-transport material, the electron-transport material, and the emissive material – were copolymerized from side-chain monomers. Using a copolymer with a polyvinyllic backbone and with side groups consisting of iridium complexes for emission, *N,N'*-diphenyl-*N,N'*-bis(3-methylphenyl)-[1,1'-biphenyl]-4,4'-diamine (TPD) for hole transport, and 2-(4-biphenyl)-5-(4-tert-butylphenyl)-1,3,4-oxadiazole (PBD) for electron-transport, external quantum efficiencies of up to 11.8% were achieved (see Figure 5.2) [114].

5.2 Experimental Results

In the present study, copolymers based on the very efficient host-guest system of CBP:Ir(ppy)₃ were synthesized by the group of Prof. Markus Weck of the School of Chemistry and Biochemistry at the Georgia Institute of Technology and their structure was optimized to achieve high efficiencies in an OLED. For that purpose, iridium complexes and a 2,7-di(carbazol-9-yl)fluorene group, a very close relative of CBP, were covalently attached to the polymer backbone by randomly copolymerizing the two

functional monomers using a ring-opening metathesis polymerization (ROMP), which is a living polymerization that allows high control over the molecular weight and the monomer distribution within the copolymer from random to block copolymers [147]. By synthesizing the copolymer in this manner, the structure of each monomer can be optimized independently without drastically modifying the polymerization reactivity.

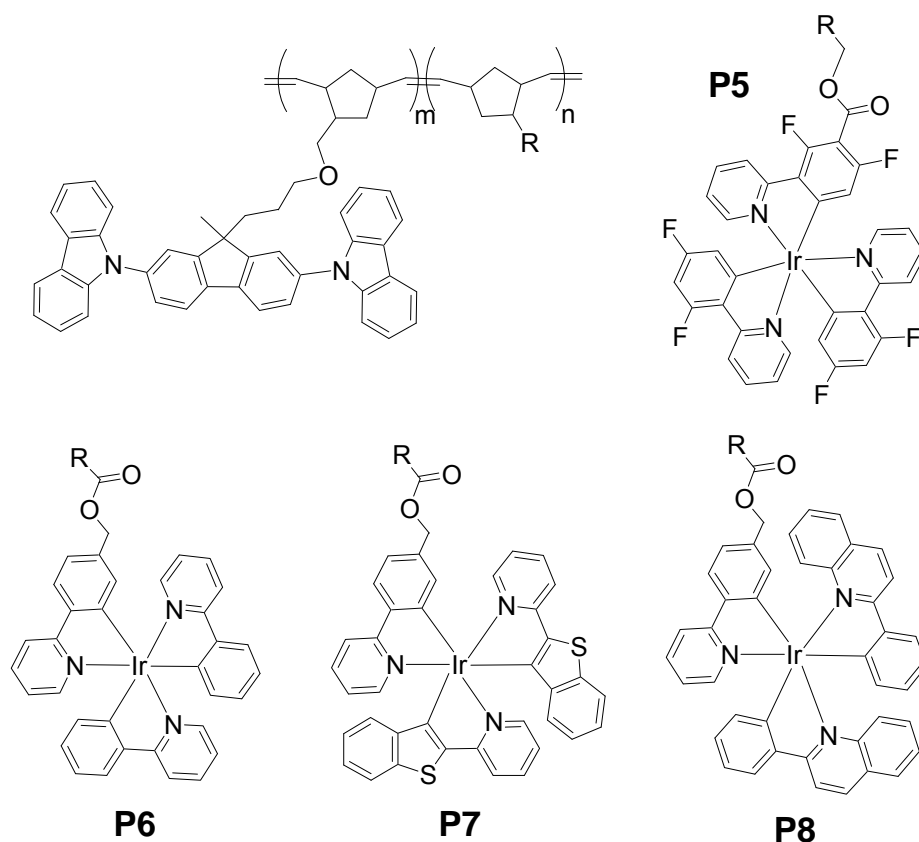


Figure 5.3. Chemical structures of carbazoyl-fluorene based copolymers with different iridium complexes where the ratio m:n is 9:1.

It is well known that the color of iridium complexes can be tuned by the attachment of substituents to the ligands that are surrounding the heavy metal atom [148-152]. Therefore, by incorporating different iridium complexes in the copolymer,

materials with four different emission spectra were synthesized and used in OLED devices (see Figure 5.3) [147]. With the goal of optimizing the efficiency of OLEDs based on these copolymers, structural changes were then made to the copolymer with the orange-emitting iridium complex, which showed the highest efficiency in the initial screening of the four copolymers with different electroluminescence spectra.

5.2.1 Iridium Complex Variation

Figure 1.1 shows the electroluminescence spectra of devices in which the copolymers **P5-P8** have been used as the emitting layer between the crosslinked TPD-based copolymer **P1** (see Figure 4.2, page 46) as the hole-transport material (35 nm) and vacuum-deposited layers of BCP (6 nm), AlQ₃ (20 nm), LiF (1 nm), and aluminum (150 nm) as hole-blocking, electron-transport, electron-injection, and cathode layer, respectively (Figure 5.7, page 68). Devices fabricated using copolymers **P6-P8** show electroluminescence spectra with emission maxima that are similar to those measured in photoluminescence experiments performed on the copolymers in solid state [147]. However, it should be noted that the electroluminescence (EL) spectra of devices fabricated using copolymer **P5** show a shift toward longer wavelengths with a maximum at 511 nm compared to a maximum of 465 nm in photoluminescence spectra (Figure 5.4).

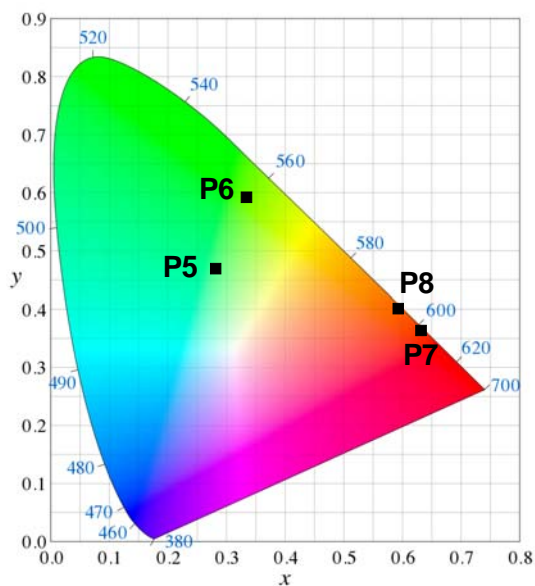
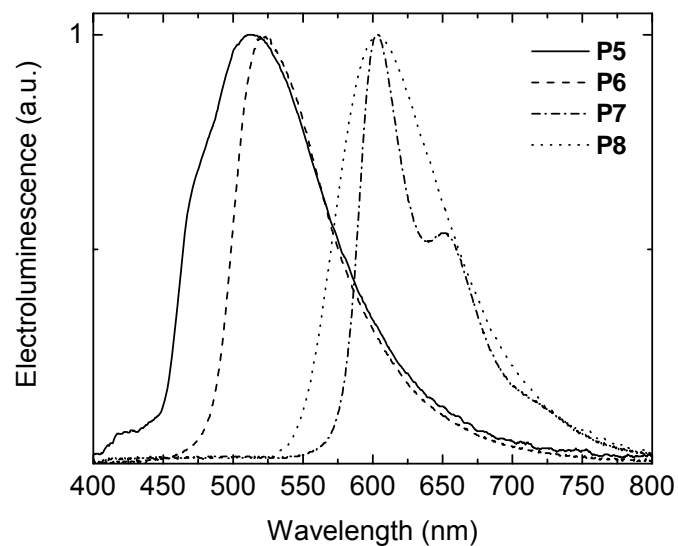


Figure 5.4. Electroluminescence spectra for devices with the structure ITO/**P1** (35 nm)/**P(5-8)** (25 nm)/BCP (6 nm)/AlQ₃ (20 nm)/LiF (1 nm)/Al and the corresponding CIE 1931 coordinates.

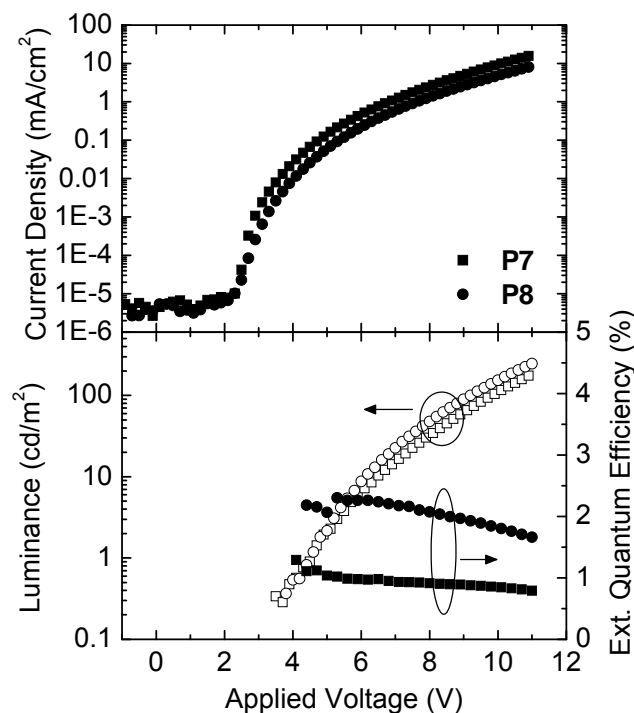


Figure 5.5. Current density (solid symbols, top), luminance (empty symbols, bottom), and external quantum efficiency (solid symbols, bottom) as a function of the applied voltage for devices with the structure ITO/P1 (35 nm)/(P7 or P8) (25 nm)/BCP (6 nm)/AlQ3 (20 nm)/LiF (1 nm)/Al.

Figure 5.5 shows the electrical characteristics of devices fabricated with copolymer **P7** and **P8** as emitting layers. External quantum efficiencies at 100 cd/m² were 0.9% and 1.9% for devices with copolymer **P7** and **P8**, respectively. These results are encouraging given the low photoluminescence quantum efficiency of these two copolymers (7% and 10% for copolymers **P7** and **P8**, respectively, in solution) compared to that of Ir(ppy)₃ (40% in solution and 97% in doped thin films) [153, 154]. Devices fabricated from copolymers **P5** and **P6**, on the other hand, yielded low light output and

very low efficiencies. The origin of the lower performance in our copolymer materials, especially in **P5** and in **P6**, compared to their small-molecule counterparts is not well understood at this stage and has to be further investigated.

5.2.2 Optimization Rationale

Since the orange copolymer **P8** showed the highest efficiency of copolymers **P5-P8** in this first screening of copolymers with different colors, this copolymer was further used in a study with the goal of optimizing the performance of such copolymers in OLEDs. In this study, several properties of the copolymer **P8**, including its iridium concentration, its molecular weight, and the nature and length of the linker group between the side groups and the polymer backbone were varied. The molecular weight M_n was varied because it may influence processing and the morphology of the films, which in turn will impact device performance. Likewise, the concentration of the iridium emitter was varied and optimized to mitigate the adverse effects of concentration quenching and to avoid any insufficient energy transfer from host to guest material in the emissive layer, as has been reported previously for evaporated and molecularly doped OLEDs [55, 155].

Finally, the nature and length of the linker group between the side-chains and the polymer backbone was varied (Figure 5.6). While a short spacer between the emissive center and the polymer backbone might be desirable to minimize the number of inactive groups, a long spacer for the emitter may be desirable to achieve better mixing with the host material units. Furthermore, the variation of the length of the linker group between the emitter and the backbone was also motivated by the work of Evans *et al.* [142] that

suggested that a longer linker could minimize the wavefunction overlap between the organometallic complex and the hole-transport moiety, reducing Dexter triplet energy back-transfer from the emitter to the host material.

In another study, we changed the nature of the linker between the hole-transport material and the polymer backbone to address the effect of its polarity on device performance while keeping its length short. Hence, an ether linker was replaced by a more polar ester linker. Such a substitution can lead to a decrease of the hole mobility of the polymer due to the higher polarity of the ester group [128, 156], leading to better balance between holes and electrons, as suggested previously [138].

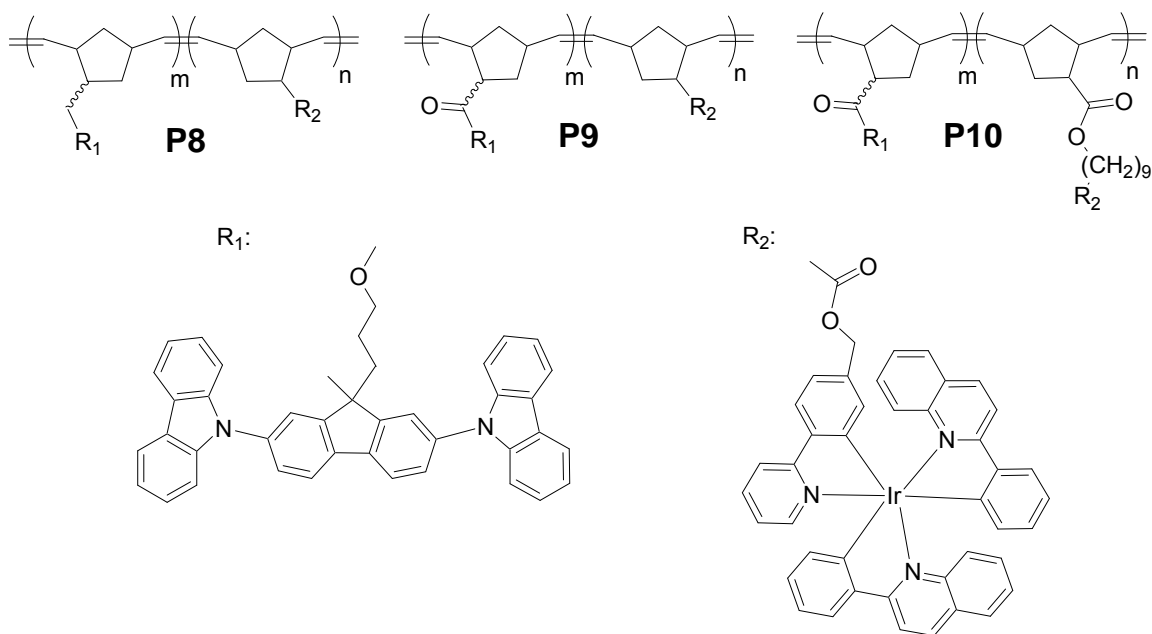


Figure 5.6. Chemical structure of orange copolymers with different linker groups.

In the following discussion, the different copolymers that have been synthesized and studied will be referred to as **P(8-10)(a-c)(n)**. The first numeric index (**8-10**) is used

to identify the polymers as shown in Figure 5.6. The second index (**a-c**) refers to the molecular weight range of the copolymer where (**a**) is the lowest and (**c**) is the highest molecular weight, and finally the third index (**n**) refers to the percentage of iridium containing monomers relative to the total number of monomers that were used in the polymerization.

5.2.3 Molecular Weight and Iridium Content Variation

For the device fabrication, a 35 nm-thick film of the TPD-based copolymer **P3** (see Figure 4.2, page 46) was employed as hole-transport material. The TPD-derivative with two fluoro groups was chosen since this derivative has a larger ionization potential compared to **P1** which leads to higher efficiencies in OLEDs, as shown in chapter 3. The hole-transport material was spin-coated onto air plasma-treated ITO coated glass substrates and crosslinked under a broadband UV light. A 25 nm-thick film of the copolymers was then spin-coated on top of the hole-transport material, followed by vacuum deposition of 40 nm of BCP as the hole-blocking layer, 1 nm LiF as the electron-injection layer, and aluminum as the cathode layer (Figure 5.7).

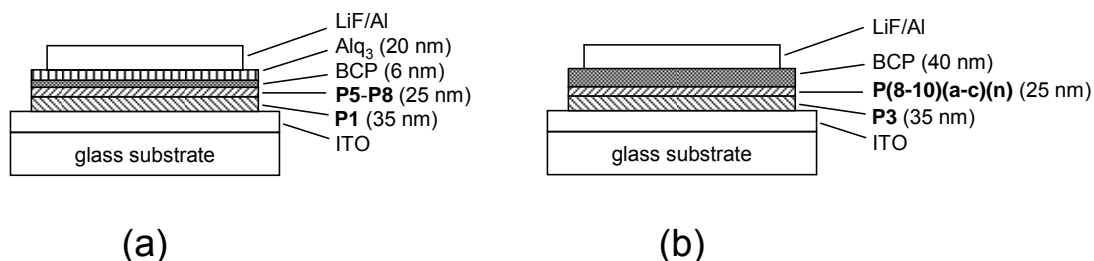


Figure 5.7. Device structure of OLEDs based on copolymers with different colors (a) and device structure for optimization of the orange-emitting copolymer **P8** (b).

External quantum efficiencies and luminous efficiencies at 100 cd/m² for the devices fabricated with different copolymers are listed in Table 5.1. The efficiency of devices with copolymers of different molecular weight (**P8a-c(10)**) was found to decrease for the copolymers with the highest molecular weight (238 kDa). However, no significant difference in efficiencies could be found when the molecular weight was varied between 19 kDa and 70 kDa.

Table 5.1. Characterization of copolymers with peak maxima of solid-state photoluminescence $\lambda_{\max,PL}$ and electroluminescence spectra $\lambda_{\max,EL}$, plus external quantum efficiencies and luminous efficiencies at 100 cd/m² for devices based on phosphorescent copolymers with various molecular weights, various iridium concentrations, and different linkers between the side groups and the polymer backbone. The device structure was ITO/**P3** (35 nm)/**P(8-10)(a-c)(2-40)** (20-25 nm)/BCP (40 nm)/LiF (1 nm)/Al.

Polymer	m:n [mol%]	M _n [kDa]	$\lambda_{\max,PL}$ [nm]	$\lambda_{\max,EL}$ [nm]	EQE [%]	Luminous efficiency [cd/A]
P8a(10)	89:11	19.0	594	600	2.9±0.3	3.9±0.4
P8b(10)	92:8	70.0	590	602	3.2±0.3	4.9±0.4
P8c(10)	90:10	238.0	591	607	1.5±0.1	2.0±0.1
P8a(2)	98:2	16.0	595	596	1.9±0.3	2.6±0.4
P8a(5)	95:5	23.0	605	598	3.4±0.4	4.6±0.5
P8a(7)	93:7	16.0	597	602	3.0±0.4	4.1±0.5
P8a(15)	81:19	21.0	605	607	2.4±0.2	3.2±0.3
P8a(20)	79:21	19.5	604	607	2.0±0.1	2.7±0.2
P8a(30)	75:25	19.5	612	611	1.9±0.1	2.6±0.1
P8a(40)	71:29	27.0	613	612	1.7±0.1	2.3±0.1
P9a(10)	90:10	16.0	592	605	3.9±0.3	5.3±0.4
P10a(10)	90:10	20.0	594	603	4.5±0.5	8.0±0.9
P10a(5)	95:5	16.5	595	597	4.9±0.4	8.8±0.7

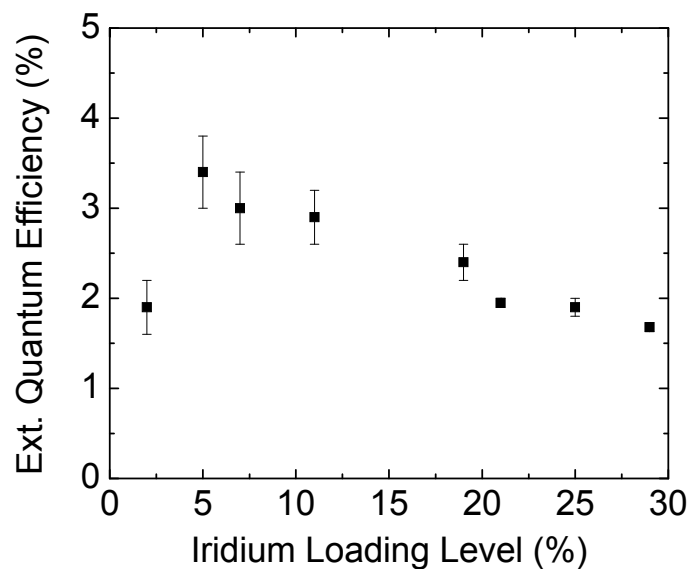


Figure 5.8. External quantum efficiencies as a function of the loading level of the iridium complex in the copolymer for OLEDs with device configuration ITO/P3 (35 nm)/P8a(2-40) (20-25 nm)/BCP (40 nm)/LiF (1 nm)/Al.

The study of the dependence of the concentration of the iridium complex in the copolymer (**P8a(2-40)**) showed that the highest efficiency could be achieved for loading levels around 5 mol% (Figure 5.8). This is in agreement with several literature reports of similar studies on evaporated and molecularly doped OLEDs where the best efficiencies are generally reported for iridium complex concentrations below 8 wt%, or 5-6 mol% [55, 56, 59, 113, 116, 123, 155, 157]. For higher loading levels, concentration quenching as mentioned in section 2.2.6 is expected [58]. For concentrations below 1 wt%, light emission from the host and the guest can be observed simultaneously [123], indicating that the efficiency of the energy transfer from the host to the guest is reduced. In our case,

a red shift in the electroluminescence spectrum was also observed for increasing iridium concentration (Figure 5.9), comparable to the red-shift measured in the photoluminescence spectra of these polymers. While the maximum of the spectrum is at 596 nm for the copolymer with an iridium complex concentration of 5 mol%, it shifts to 612 nm for copolymers with 29 mol% iridium concentration. For the low concentration of 2 mol%, a slight shoulder in the spectrum at 500 nm was visible. With a 5 mol% iridium concentration, the CIE 1931 coordinates of the emission were (0.58, 0.42).

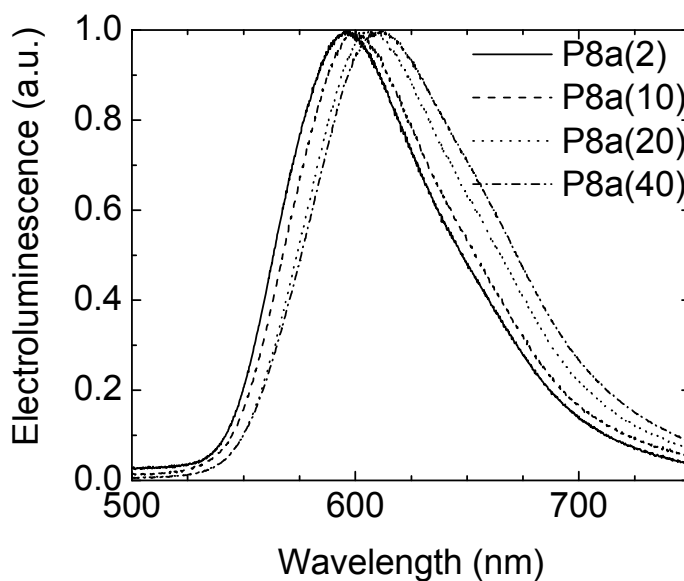


Figure 5.9. Electroluminescence spectra for OLED devices using copolymers **P8a(2, 10, 20, 40)** with increasing iridium complex content as emitting layer.

5.2.4 Spacer Variation

In a next step, the influence of the linkage between the functional groups and the polymer backbone on the efficiency of the OLEDs was studied. First, the ether group that connects the bis(carbazolyl)fluorene group to the polymer backbone was replaced by an ester group (**P9**). The efficiency of an OLED with **P9a(10)** as the emissive layer was 1% higher at 100 cd/m² than for the copolymer with an ether linkage. Finally, inserting an elongated linkage between the iridium complex and the polymer backbone (**P10a(10)**) increased the EQE by another 0.6%.

Combining the results discussed above, a copolymer with an elongated ester linker and an iridium complex concentration of 5 mol% was synthesized (**P10a(5)**). The external quantum efficiency measured in an OLED based on this copolymer as emissive layer was the highest of the present study: 4.9±0.4% and 8.8±0.7 cd/A at 100 cd/m² (Figure 5.10). This result validates the trends that were established through our studies in which we varied different properties independently. Given the low value (10% in toluene) of the photoluminescence quantum yield of the orange iridium emitter that was incorporated in these copolymers [147], the measured EQE of 4.9% in devices with polymer **P10a(5)** indicates that the electroluminescent properties of this copolymer are nearly optimized.

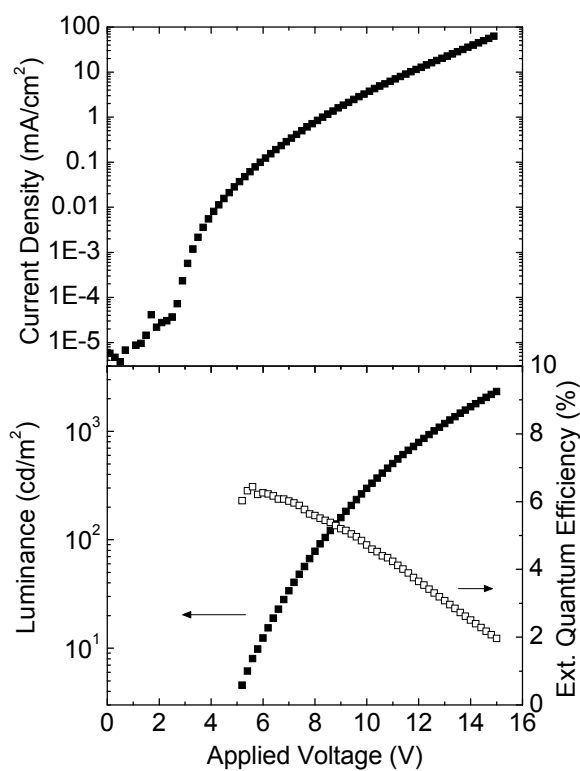


Figure 5.10. Current density (solid symbols, top), luminance (solid symbols, bottom), and external quantum efficiency (empty symbols, bottom) as a function of the applied voltage for a device with structure ITO/P3 (35 nm)/P10a(5) (25 nm)/BCP (40 nm)/LiF (1 nm)/Al.

CHAPTER 6

SOLUTION-PROCESSED ELECTROPHOSPHORESCENT MULTILAYER OLEDs

6.1 Introduction

In the previous chapter, the fabrication of OLEDs with a solution-processed hole-transport and emissive layer was described. However, the reported devices still required an evaporated electron-transport/hole-blocking layer to achieve maximum efficiency. The following chapter will now focus on devices in which all organic layers are processed from solution. First, solution-processed multilayer structures with electron-transport/hole-blocking layers from the literature are discussed. Then, our approach for photocrosslinking of the emissive layer is described, and devices with three solution-processed layers will be shown. Finally, photocrosslinking of the emissive layer will be used to fabricate patterned devices with two different colors to create a white light source with a tunable emission spectrum.

6.1.1 State of the Art

As has been discussed in the previous chapter, many reports of OLEDs with a solution-processed emissive layer have been published. However, with some exceptions [68, 112], most solution-processed OLEDs show only low efficiencies if no electron-transport/hole-blocking layer is integrated in the device structure [69, 158, 159]. To date, almost all reports of OLEDs with a solution-processed emissive layer that show high

efficiencies therefore include a thermally evaporated electron-transport/hole-blocking layer between the emissive layer and the cathode.

Nevertheless, some fully solution-processed multilayer OLEDs including a solution-processed electron-transport layer have been reported in the literature [130, 159-166]. Only about half of these reports are electrophosphorescent OLEDs [159, 160, 164, 166]. However, for all the reported devices the efficiencies were increased because of the additional solution-processed electron-transport layer.

Different methods for solution-processed multilayer stacks have been mentioned before (chapter 5.1.1, page 55). The most popular approach to achieve multilayer OLEDs from solution is the use of orthogonal solvents for adjacent layers. Typically, water- or alcohol-soluble hole- and electron-transport materials are used whereas the emissive layer is processed from an organic solvent [160, 162-166]. Alternatively, multilayer devices with good efficiencies have also been fabricated by crosslinking of the emissive layer [159, 161]. While most of the reported efficiencies in solution-processed multilayer OLEDs are low, there is one report by Wang *et al.* of exceptionally high efficiencies up to 18.0% at 100 cd/m² with four spin-coated organic layers [164]. The device structure for such a highly efficient OLED consisted of a hole-injection layer of poly(3,4-ethylenedioxythiophene):poly(styrenesulfonate) (PEDOT:PSS) processed from water on top of an ITO substrate, followed by a hole-transport layer of PVK processed from chlorobenzene [167]. The emissive layer was a blend of polyfluorene, PBD and a red-emitting iridium complex in a *p*-xylene solution. Finally, an electron-transport layer of poly[(9,9-bis(3'-((*N,N*-dimethyl)-*N*-ethylammonium)propyl)-2,7-fluorene)-2,7-(9,9-dioctylfluorene)-4,7-(2,1,3-benzoselenadiazole)]dibromide (PFN) was processed from a

methanol solution. A barium electron-injection layer and an aluminum cathode were evaporated on top of the organic layers.

6.1.2 Crosslinking of the Emissive Layer

Although the use of orthogonal solvents is the most popular method for solution-processed multilayer OLEDs, crosslinking places fewer restrictions on the solubility of the materials and is therefore preferable. Furthermore, if crosslinking can be achieved by exposure to light, fewer steps are necessary in the fabrication of patterned OLEDs [131, 132]. Therefore, a crosslinkable emissive layer will be introduced here (Figure 6.1). This crosslinkable copolymer is based on the optimized orange copolymer, as described in chapter 4, with the addition of a cinnamate based group that has already been used for the crosslinkable hole-transport materials in chapter 3. The copolymer was synthesized by the group of Prof. Markus Weck of the School of Chemistry and Biochemistry at the Georgia Institute of Technology.

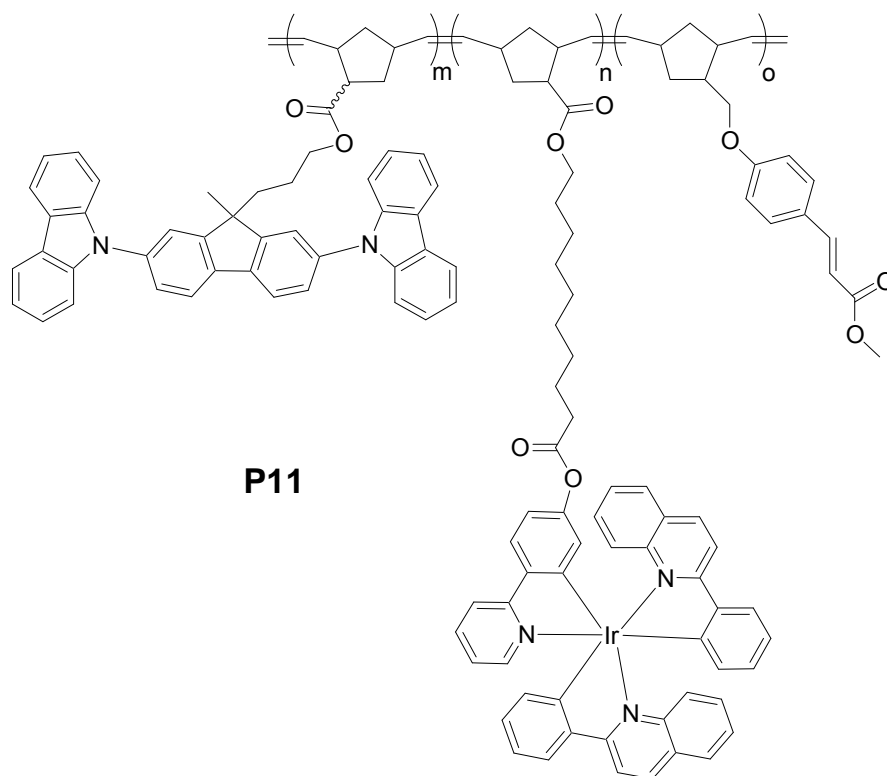


Figure 6.1. Crosslinkable electrophosphorescent copolymer based on polymer **P10a(5)** with a charge-transport moiety (left), a phosphorescent orange-emitting complex (center), and a crosslinkable cinnamate based group (right) with $m:n:o = 70:5:25$.

6.1.3 Electron-Transport/Hole-Blocking Polymer

Not many electron-transport polymers for organic light-emitting diodes have been reported in the literature, and none are commercially available. Hence, for most of the above mentioned literature with solution-processed multilayer OLEDs, new polymers had to be synthesized for the electron-transport layer. All of these newly synthesized electron-transport polymers were based on polyfluorene where electron-transport groups were added to either the backbone of the polymer (see Figure 6.2) [161, 165] or to its side-chains [162, 164, 166]. Where electron-transport polymers were not available, electron-

transport small-molecules were either processed directly from solution [130, 160, 163] or they were processed in a polymer matrix [159]. For the present work, new polymers based on small molecules with known electron-transport properties have been synthesized by the group of Prof. Seth Marder of the School of Chemistry and Biochemistry at the Georgia Institute of Technology as potential candidates for a solution-processable electron-transport/hole-blocking layer. Two of these polymers are presented in the following paragraphs.

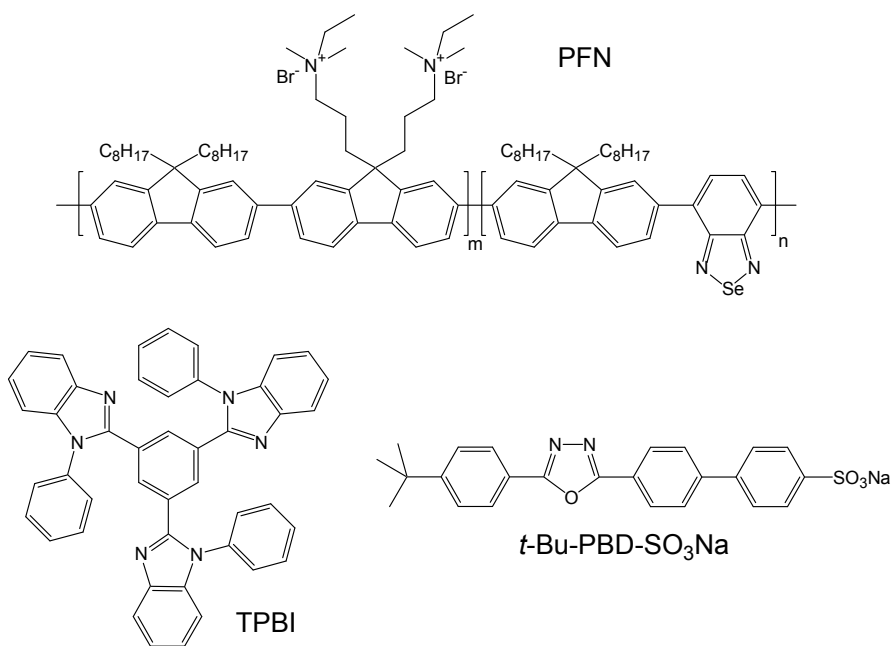


Figure 6.2. Chemical structures of solution-processable electron-transport materials used in the literature [130, 160, 164]. Whereas PFN and TPBI are examples of a polymer and a small molecule, respectively, that are soluble in organic solvents, *t*-Bu-PBD-SO₃Na is soluble in ethanol.

Silacyclopentadienes (siloles) have been used primarily in fluorescent OLEDs since their photoluminescence can be tuned and high electron mobilities can be achieved.

First mentioned in 1996 as an electron-transport material [168], siloles were shown to have comparable electron affinities [169], but significantly higher electron mobilities than Alq₃ [170]. Consequently, high external quantum efficiencies have been shown in fluorescent OLEDs where both the emissive layer and the electron-transport layer were comprised of different silole derivatives [171]. The small molecule equivalent of the silole polymer that is used in this work (**P12**, Figure 6.3) is expected to have a high ionization potential [169] and has been used in OLEDs before [172].

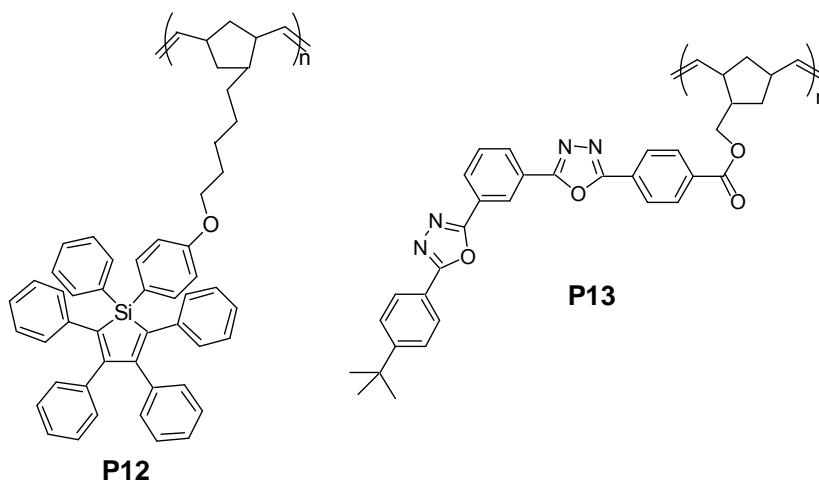


Figure 6.3. Chemical structures of electron-transport polymers based on a silole small-molecule (**P12**) and based on a bisoxadiazole small-molecule (**P13**).

The second electron-transport polymer was based on a bisoxadiazole small molecule (**P13**, Figure 6.3). As mentioned in the context of molecularly doped OLEDs (section 5.1.2, page 56), oxadiazoles have been used successfully as dopants in the emissive layer for more efficient electron-transport and better charge balance in the device [63, 68, 173]. Electron mobilities of 10^{-5} cm²/Vs were measured for the oxadiazole

derivative PBD [174]. Furthermore, some oxadiazoles have a high ionization potential, which makes the material attractive as a hole-blocking and electron-transport material simultaneously [175]. The bisoxadiazole polymer that is used here is derived from a small molecule with a high ionization potential that has led to high efficiencies in molecularly doped OLEDs [68, 133, 176].

6.2 Experimental Results

6.2.1 OLEDs with a Crosslinkable Emissive Layer

To test the effect of a crosslinked emissive layer on the device performance, devices similar to those in chapter 4 were fabricated. A 35 nm-thick film of the hole-transport polymer **P3** was spin-coated onto air-plasma treated ITO coated glass and crosslinked under a broadband UV light with an exposure of 40 mJ/cm². An approximately 17 nm-thick film of the crosslinkable copolymer **P11** was then spin-coated on top of the hole-transport layer. After the deposition of the crosslinkable copolymer, some substrates were directly transferred into the vacuum chamber while others were exposed to UV with a dose of 1250 mJ/cm² first. Unfortunately, such a high energy dose is necessary to crosslink even such a thin layer of the copolymer **P11** since the hole-transport moiety of the copolymer absorbs in the same wavelength range as the cinnamate group that is used for the photocrosslinking (Figure 6.4) [100]. To finish the device fabrication, a 40 nm-thick film of BCP was vacuum deposited on top of the solution-processed layers, followed by a 2.5 nm-thick film of LiF and a 200 nm-thick film of aluminum.

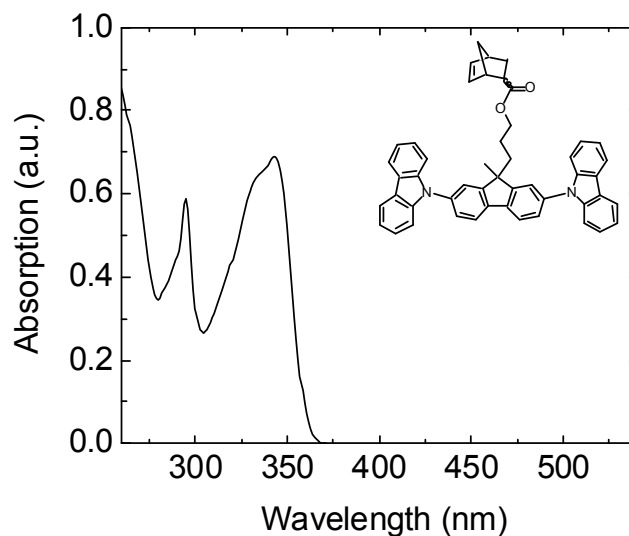


Figure 6.4. Absorption spectrum of the monomer of the hole-transport moiety in copolymer **P11**.

For the resulting devices, the current density, the luminance and the external quantum efficiency as a function of the applied voltage are shown in Figure 6.5. First of all, it should be noted that the efficiencies for devices with the crosslinkable copolymer as the emissive layer are generally lower than the efficiencies reported for the copolymer without the crosslinking group (chapter 4). This decrease can be attributed to a poor charge balance since more than a quarter of all hole-transport moieties in the copolymer have to be replaced by cinnamate groups to achieve crosslinking of the material.

Furthermore, Figure 6.5 shows that all the measured characteristics decrease after the long UV exposure of the emissive layer, resulting in an external quantum efficiency of only $0.5 \pm 0.1\%$ at 100 cd/m^2 . A similar decrease at high UV exposure has been reported earlier for PVK-based OLEDs [177]. These results indicate that photo-

crosslinking is not suited for carbazole-based materials, but other crosslinking processes will have to be pursued. Nevertheless, since OLEDs with non-negligible efficiencies can be fabricated using the crosslinkable copolymer **P11**, solution-processed multilayer OLEDs will be demonstrated using this emissive layer.

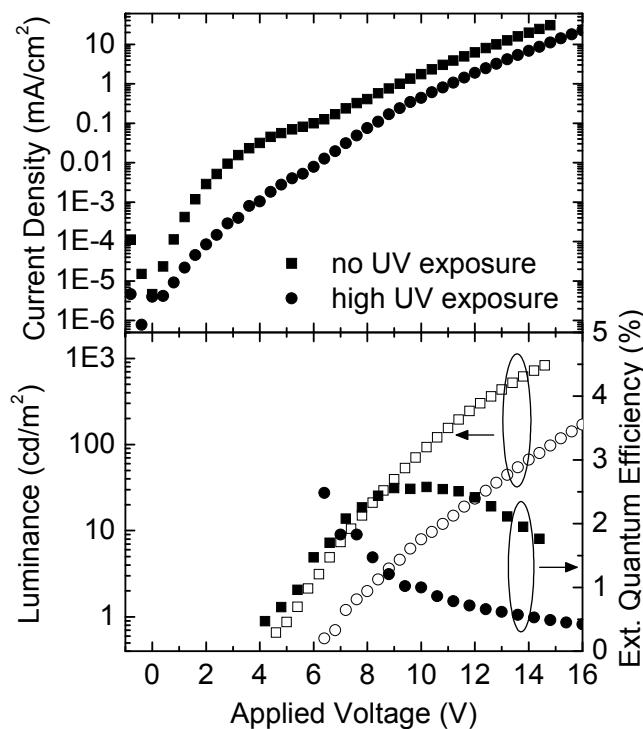


Figure 6.5. Current density (solid symbols, top), luminance (empty symbols, bottom), and external quantum efficiency (solid symbols, bottom) as a function of the applied voltage for devices with the structure ITO/**P3** (35 nm)/**P11** (17 nm)/BCP (40 nm)/LiF (2.5 nm)/Al with (circles) and without (square) 1250 mJ/cm² UV exposure of **P11**.

6.2.2 Solution-Processed Multilayer OLEDs

For devices with a solution-processed electron-transport layer, the hole-transport and the emissive layer were deposited and crosslinked as described in section 6.2.1.

Additionally, instead of the evaporation of BCP, one of the two electron-transport polymers **P12** and **P13** was spin-coated from toluene (**P12**) or from chlorobenzene (**P13**) on top of the crosslinked emissive layer to form a layer with a thickness of 40 or 35 nm, respectively. Finally, 2.5 nm of LiF and 200 nm of aluminum were thermally evaporated as an electron-injection layer and the cathode.

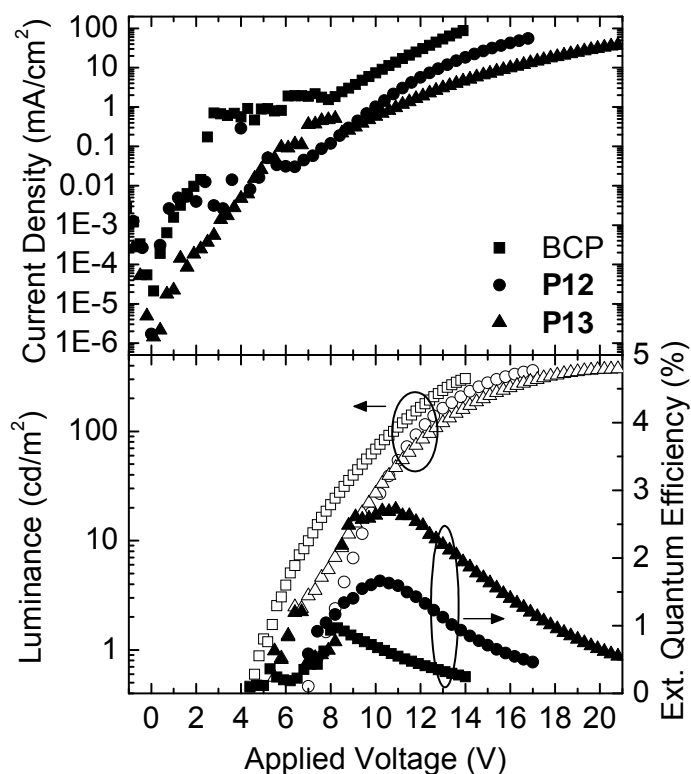


Figure 6.6. Current density (solid symbols, top), luminance (empty symbols, bottom), and external quantum efficiency (solid symbols, bottom) as a function of the applied voltage for devices with the structure ITO/**P3** (35 nm)/**P11** (17 nm)/ETL (35-40 nm)/LiF (2.5 nm)/Al where the electron-transport layer (ETL) consisted of BCP (squares), **P12** (circles), or **P13** (triangles).

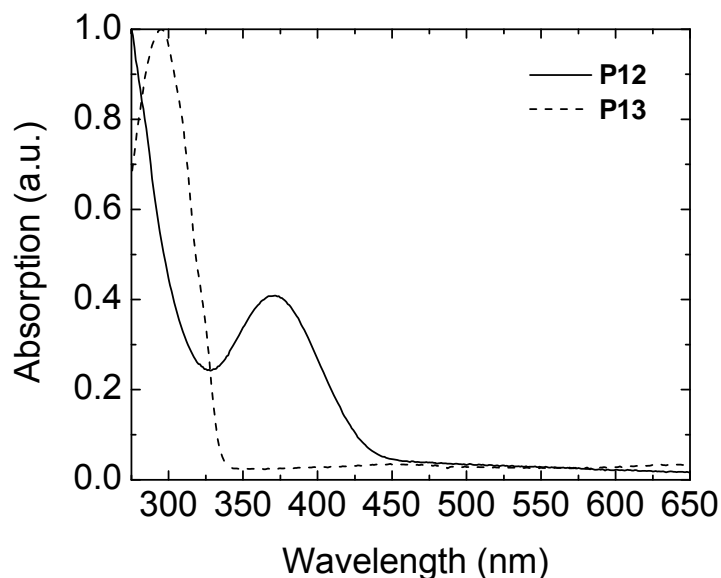


Figure 6.7. Absorption spectra of P12 (solid line) and P13 (dashed line).

The current density, the luminance and the external quantum efficiency as a function of the applied voltage of these solution-processed multilayer OLEDs are shown in Figure 6.6. A decrease of the current densities was observed for devices with a solution-processed electron-transport layer compared to the evaporated BCP layer. This decrease can be attributed to an electron mobility in the polymers that is expected to be lower compared to BCP [109]. However, a decrease in the number of electrons can increase the charge balance in the device by matching the hole current that has been decreased because of the use of the crosslinkable emissive layer (see above). Therefore, higher efficiencies can be measured in devices with a solution-processed electron-transport layer. The higher efficiency of $2.0 \pm 0.2\%$ at 100 cd/m^2 for devices with **P13** compared to an efficiency of $1.3 \pm 0.1\%$ at 100 cd/m^2 for devices with **P12** can be

explained by the larger energy gap of **P13** (see the absorption spectrum of the two electron-transport polymers in Figure 6.7). Assuming that the two polymers **P12** and **P13** have similar electron affinities, we expect that **P13** has a higher ionization potential than **P12**, which makes it more suitable as a hole-blocking material whereas holes can be transported more easily across a layer of **P12**.

6.2.3 Photopatterned OLEDs

After the successful demonstration of solution-processed multilayer OLEDs, the photocrosslinkable emissive copolymer can be used to pattern a substrate with different colors. Patterning is required mainly for display applications where red, green, and blue (RGB) pixels have to be placed in close proximity to each other. For example, in mobile display applications like cell phones, an RGB pixel containing pixels of each color usually covers only an area in the range of $300 \times 300 \mu\text{m}^2$. However, patterning of areas with different colors is also necessary for certain lighting applications, i.e. for mood-lighting panels that are color tunable to simulate the sun light at different hours of the day. Patterning of displays by using photocrosslinkable emissive materials has already been reported with fluorescent and phosphorescent materials [132, 159]. Unlike those reports, the present work focuses on color tuning in lighting applications.

To achieve a tunable white light, OLEDs of at least two different colors have to be driven separately. Consequently, a separation of the two colors is needed in the emissive layer and in either the cathode or the anode. Here, the ITO anode was etched into an interdigitated pattern as shown in Figure 6.8. Linewidths of $110 \mu\text{m}$ with $40 \mu\text{m}$ gap in between were chosen, which corresponds to a period of $300 \mu\text{m}$ as used in RGB

pixels. White light was then achieved as a combination of orange and blue color [178]. For orange emission, the crosslinkable copolymer **P11** was used. Blue light, on the other hand, was generated in a layer of the crosslinkable TPD-based copolymer **P3** by relying on the fluorescence of TPD [179, 180]. Part of a substrate with patterned ITO and one crosslinked polymer layer after development is shown in Figure 6.8.

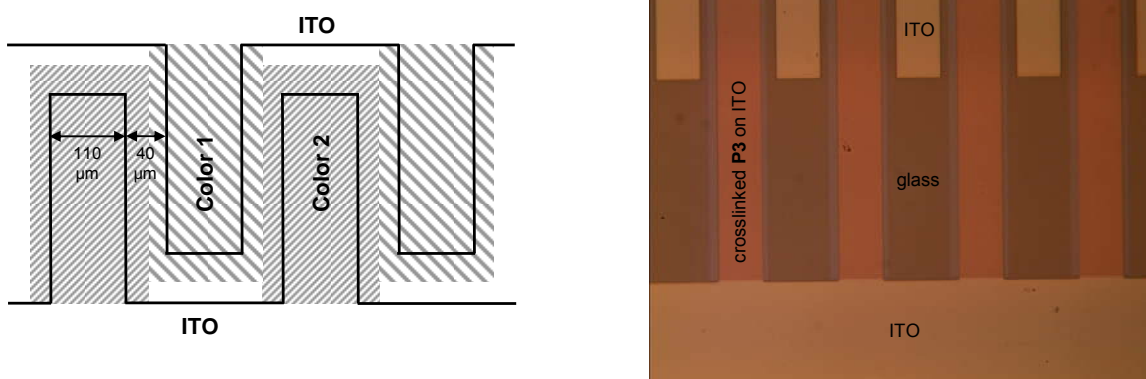


Figure 6.8. Schematic of interdigitated electrodes with photopatterned emissive layers (left), and a micrograph of the electrodes with a photopatterned layer of **P3** (right).

The following procedure was used to fabricate the photopatterned OLEDs. First, the ITO on a glass substrate was patterned using standard etching procedures. A hole-transport layer consisting of the crosslinkable TPD-based copolymer **P3** with a thickness of 35 nm was then spin-coated on top of the patterned ITO and crosslinked under a broadband UV light with an exposure of 40 mJ/cm². Next, a 17 nm-thick layer of the orange crosslinkable copolymer **P11** was deposited from solution on top of the hole-transport layer and crosslinked in a mask aligner at a wavelength of 365 nm with an exposure of 1250 mJ/cm² through a mask. The pattern was developed by spin-coating chlorobenzene on top of the exposed film. For the blue lines, a 35 nm-thick layer of **P3**

was deposited as the emissive layer to achieve similar current densities and drive voltages for the orange and the blue lines. The blue emissive layer was patterned like the orange emissive layer except that the exposure was only 40 mJ/cm^2 . Finally, a 35 nm-thick layer of the bisoxadiazole polymer **P13** was spin-coated on top of the patterned emissive layers, and a 200 nm-thick aluminum cathode was thermally evaporated. The final device under operation is shown in Figure 6.9. A diagram of the fabrication process of the patterned multilayer device is shown in the Appendix.

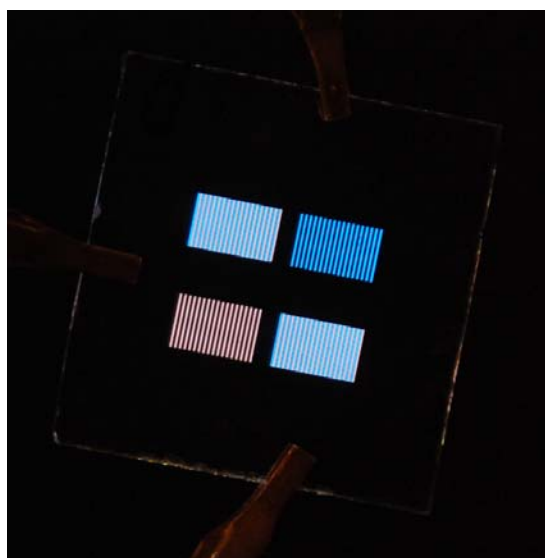


Figure 6.9. Photograph of photopatterned OLEDs with orange electrophosphorescent and blue electrofluorescent lines with linewidths of $110 \mu\text{m}$.

By changing the applied voltage for the lines with different color, the spectrum of the mixed devices could be tuned throughout the white. However, because of the low intensity of the devices and their short lifetime, CIE coordinates could not be measured.

CHAPTER 7

MODELING THE CHARGE INJECTION INTO OLEDs

7.1 Introduction

As mentioned earlier, organic semiconductors have recently advanced enough to be incorporated into a variety of solid-state devices such as organic light-emitting diodes, organic solar cells, organic diodes, and organic field-effect transistors [23, 48, 56, 181]. When integrating these devices into circuits with increasing complexity, it becomes critical to have accurate and relatively simple models to describe their electrical characteristics. For instance, OLEDs are usually assumed to behave according to the diode equation, even though the predictive capabilities of this oversimplified model in describing the electrical properties over the full range of voltages are rather limited.

To make up for this deficiency, different approaches to model organic diodes have been reported in the literature. Simple models are achieved with partial fits of the electrical characteristics in the low voltage or high voltage range. For example, the steep increase in current at low voltages has mostly been attributed to thermionic or Schottky emission of charges across the energy barrier between the Fermi level of the electrode and the HOMO or the LUMO of the organic layer [31, 182].

The current at higher voltages is usually assumed to be limited by space-charge limited current (SCLC) effects [183-185]. However, besides for materials that make nearly ohmic contact (i.e. ITO / MEH-PPV), the electrical characteristics mostly follow a power law with an exponent that is substantially larger than two [186, 187]. Therefore, just one circuit element typically cannot fit the full electrical characteristics, and its

predictions are limited to partial fits in selected regions of the current-voltage characteristics.

Alternatively, better fits of the electrical characteristics have been achieved using more complex models based on basic semiconductor and electromagnetic equations [188-190]. These systems of equations are usually solved in a finite elements approach where the carrier and field distributions inside an organic layer are calculated and optimized to fit given boundary conditions. Although such calculations can lead to quite accurate fits of experimental data, they are heavily dependent on parameters such as the intrinsic charge carrier density or the intrinsic electric field that cannot be measured in an independent experiment, and a wide range of values have been published for these parameters [47, 188, 191, 192]. Moreover, such complicated systems of equations cannot be easily integrated in circuit design software for accurate modeling of organic devices.

In this chapter, an equivalent-circuit approach to model the electrical characteristics of a basic organic single-layer diode is presented and the model is implemented in SPICE, a widely used circuit-simulation program. The equivalent-circuit model is based on physical principles of an organic diode and will be explained in the following section. Furthermore, temperature-dependent experimental electrical characteristics of different single-layer diodes will be fitted with the proposed model to extract material parameters. Finally, the resulting parameters will be compared to the values that are reported in the literature.

7.2 Theory and Model

Based on the operational principles of organic diodes, such as charge injection and charge transport (see section 2.2.1, page 17 and section 2.2.3, page 21), an equivalent circuit model for an organic single-layer diode is proposed that consists of a thermionic Schottky diode for injection into the organic semiconductor in series with a voltage-dependent resistor representing the space-charge limited current (SCLC) for the bulk conductivity in the device (Figure 7.1). A shunt resistor R_p is placed in parallel to these two circuit elements to account for any leakage current through the device.

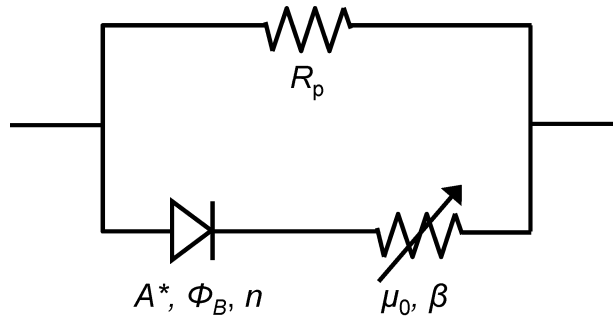


Figure 7.1. Equivalent circuit of an organic single-layer diode.

In this model, the diode is described by the general diode equation

$$J = J_0 \left(\exp \left[\frac{qV}{nkT} \right] - 1 \right), \quad (2.2)$$

where J_0 is the saturation current and n is the ideality factor. Using the prefactor for thermionic emission:

$$J_0 = A^* T^2 \exp\left(-\frac{\Phi_B}{kT}\right), \quad (2.3)$$

the value for the saturation current can further be split into the effective Richardson constant A^* and the injection barrier Φ_B if the temperature dependence of the diode is known.

Likewise, with the equation for SCLC

$$J = \frac{9}{8} \mu \epsilon \epsilon_0 \frac{V^2}{L^3}, \quad (2.12)$$

the voltage-dependent resistor in the equivalent circuit is dependent on the mobility μ and the thickness L of the organic layer. However, as shown in section 2.2.2, page 18 in the framework of the disorder formalism, the mobility is a function of the electric field and the temperature:

$$\mu(\sigma, E) = \mu_{0,0} \exp\left[-\left(\frac{2}{3} \frac{\sigma}{kT}\right)^2\right] \exp\left[C\left(\left[\frac{\sigma}{kT}\right]^2 - \Sigma^2\right)E^{1/2}\right]. \quad (2.10)$$

Assuming that the internal field of the single-layer diode is constant, and in order to minimize the number of parameters that are used in the model, the equation for the mobility is simplified to

$$\mu = \mu_0 \exp\left(\beta \sqrt{\frac{V}{L}}\right) \quad (7.1)$$

with μ_0 the zero-field mobility and β the field-dependence factor of the mobility.

7.3 Experiment

Four different materials were used as the organic layer in a single-layer device geometry (see Figure 7.2). As shown in the above chapters, 4,4'-bis[*N*-(1-naphthyl)-*N*-

phenyl-amino]biphenyl (α -NPD) and *N,N'*-bis(*m*-tolyl)-*N,N'*-diphenyl-1,1'-biphenyl-4,4'-diamine (TPD) are well-known hole-transport materials with wide bandgaps [120, 193]. Whereas α -NPD was used in its small-molecule form, a TPD-based polymer (**P1**) [100] was used for another set of devices to make sure that the proposed model does not only apply to small molecules but also to polymers. Other devices incorporated a layer of the electron-transport organic semiconductor C₆₀ or a layer of the hole-transport material pentacene. These latter two materials were selected because they have significantly higher mobilities [22, 23] and smaller bandgaps [48] compared to α -NPD and **P1**.

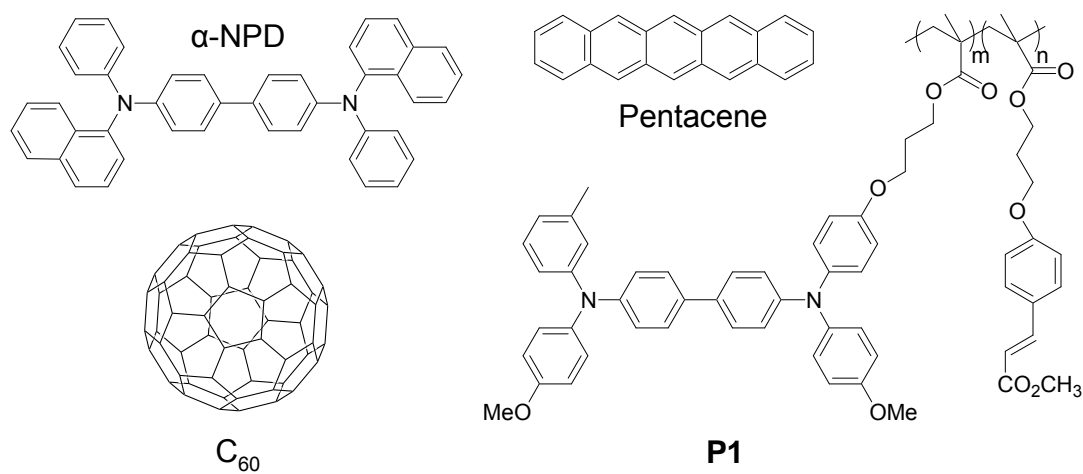


Figure 7.2. Chemical structures of α -NPD, **P1**, C₆₀ and pentacene.

Diodes were fabricated on air-plasma treated ITO coated glass substrates. For the organic layer, the small molecules of α -NPD, C₆₀, and pentacene were thermally evaporated. For C₆₀ diodes, an additional layer of 8 nm BCP was deposited on top of the fullerenes to avoid aluminum diffusion into the C₆₀ [194]. For the polymer diodes, a 90 nm thick film was spin-coated from toluene on top of the air-plasma treated ITO

substrates. The polymer film was crosslinked using a standard broad-band UV light with a 0.7 mW/cm^2 power density for 1 minute. For all diodes, a 200 nm-thick aluminum cathode was vacuum deposited on top of the organic layer. Finally, model parameter values were determined by fitting the experimental data with the equivalent-circuit model using the HSPICE optimization tool.

7.4 Results and Discussion

First, when testing a new model it is important to verify that the experimental electrical characteristics to which the model is applied are highly reproducible. Figure 7.3 shows the data of 5 different devices with geometry ITO/ α -NPD (80 nm)/Al and 5 different devices with geometry ITO/ α -NPD (150 nm)/Al. The high reproducibility of these electrical characteristics leads to a standard deviation of less than 10% of the fitted values for the ideality factor n and the zero-field mobility μ_0 . For the saturation current density J_0 and the field-dependence of the mobility β , the standard deviation is higher and can reach $\pm 100\%$ of the fitted value.

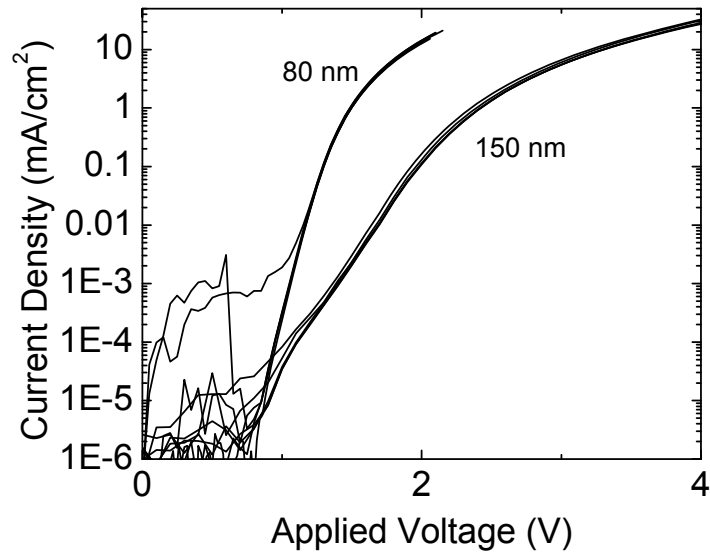


Figure 7.3. Current density versus applied voltage at room temperature for α -NPD diodes with thicknesses of 80 nm and 150 nm. Plots of five devices are shown for each thickness.

In the next step, to test the validity of the space-charge limited current model, α -NPD diodes with different thicknesses were fabricated and tested. Model parameters were extracted from fits to the experimental data (see Figure 7.4) and are summarized in Table 7.1. The mobility parameters are found to be nearly independent of the thickness, which supports the introduction of the SCLC voltage-dependent series resistor in our model.

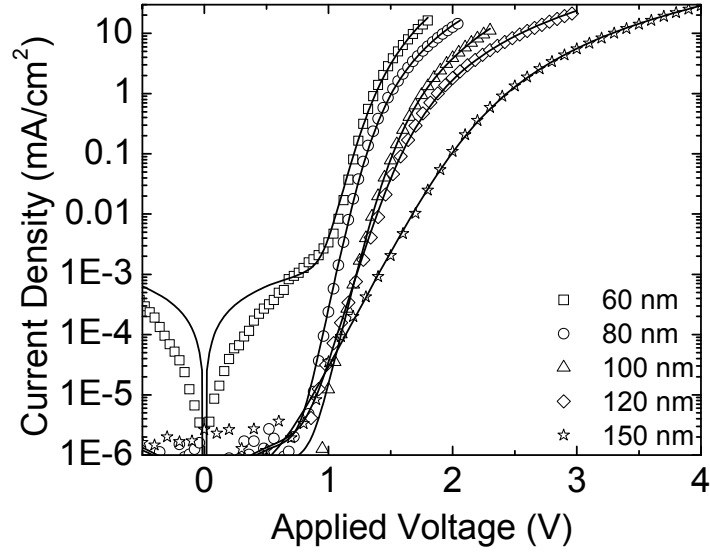


Figure 7.4. Current density as a function of the applied voltage at room temperature for α -NPD diodes with thicknesses ranging from 60 nm to 150 nm. Experimental data is shown as empty symbols; solid lines represent the simulated curves.

Table 7.1. Saturation current density J_0 , ideality factor n , parallel resistance R_p , zero-field mobility μ_0 , and mobility field-dependence factor β , all resulting from fits of the model to electrical characteristics at room temperature for α -NPD diodes with different thicknesses L .

L (nm)	J_0 (mA/cm ²)	n	R_p ($\Omega \cdot \text{cm}^2$)	μ_0 (cm ² /Vs)	β (cm/V) ^{1/2}
60	1.1×10^{-11}	2.0	8.0×10^5	1.8×10^{-4}	1.1×10^{-6}
80	6.2×10^{-14}	1.7	4.1×10^8	1.5×10^{-4}	4.9×10^{-6}
100	1.8×10^{-14}	1.9	8.7×10^8	1.2×10^{-4}	1.5×10^{-3}
120	6.5×10^{-12}	2.5	3.8×10^8	1.8×10^{-4}	1.0×10^{-7}
150	3.5×10^{-9}	4.3	9.8×10^8	2.4×10^{-4}	1.2×10^{-4}

Likewise, the model was applied to the experimental data of diodes with geometry ITO/**P1** (90 nm)/Al, and good fits were obtained except for the low voltage range (Figure 7.5). In our model, the current in that region is dominated by the parallel resistor R_p , even though the experimental data does not show a linear increase. However, since diodes, especially organic light-emitting diodes, are operated at higher voltage where current injection is more efficient, a certain discrepancy of the equivalent circuit at low voltages does not seem to be very problematic.

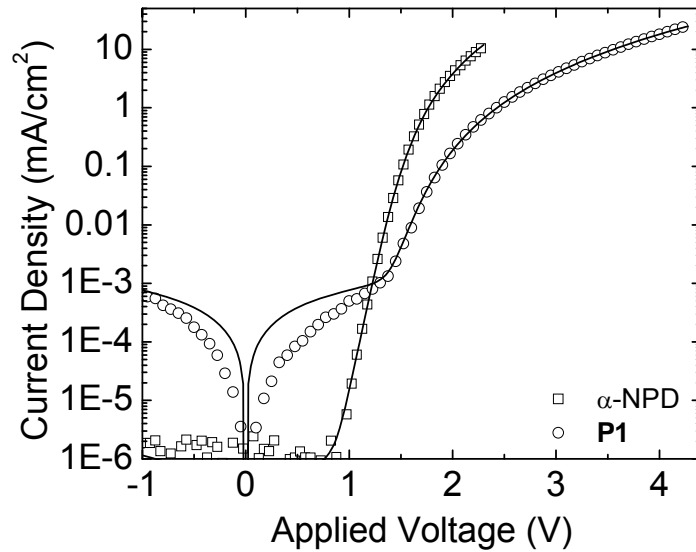


Figure 7.5. Current density as a function of the applied voltage at room temperature for organic diodes with organic layers of α -NPD (100 nm, squares) and **P1** (90 nm, circles). Experimental data is shown as empty symbols; solid lines represent the simulated curves.

From the electrical characteristics of the α -NPD diodes and the diodes of **P1** at room temperature, the mobility values were determined to be $1.2 \times 10^{-4} \text{ cm}^2/\text{Vs}$ and $4.5 \times$

$10^{-6} \text{ cm}^2/\text{Vs}$ respectively (see Table 7.2, page 99). These values are in good agreement with mobility values measured in time-of-flight experiments and SCLC measurements [93, 195, 196]. Furthermore, the temperature-dependence of the mobility can be determined from measurements of the organic single-layer diode at different temperatures, as shown in Figure 7.6 for a device with geometry ITO/ α -NPD (100 nm)/Al.

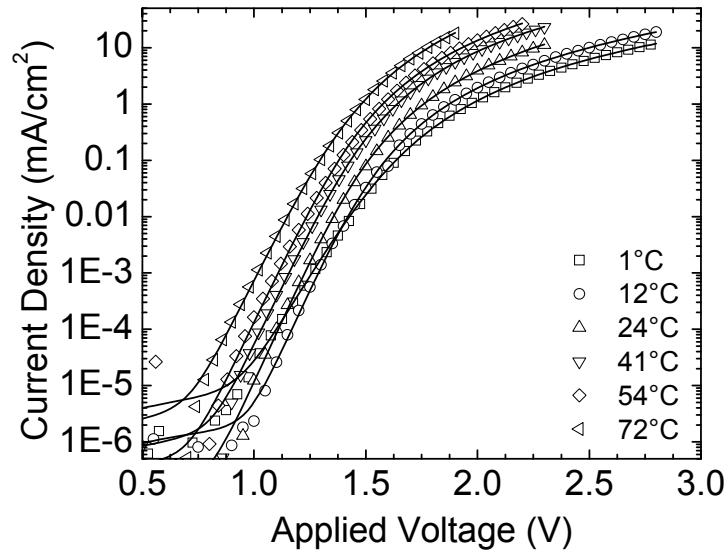


Figure 7.6. Current density as a function of the applied voltage for an α -NPD diode with a thickness of 100 nm measured at temperatures ranging from 1 °C to 72 °C. Experimental data is shown as empty symbols; solid lines represent the simulated curves.

Combining equations (2.1) and (7.1), the mobility at zero-field and zero-temperature $\mu_{0,0}$ as well as the width of the energetical disorder distribution σ can be calculated from the intercept and the slope, respectively, of a linear fit when plotting the logarithm of the zero-field mobility μ_0 versus T^2 . In fact, such plots of our extracted

parameters resulted in reasonable fits for the α -NPD diodes and the diodes incorporating **P1** (Figure 7.7). The width of the energetical disorder distribution σ was calculated to be 0.096 eV and 0.128 eV for diodes incorporating α -NPD and **P1**, respectively. The corresponding zero-field and zero-temperature mobility values were $\mu_{0,0} = 7.0 \times 10^{-2} \text{ cm}^2/\text{Vs}$ for α -NPD and $\mu_{0,0} = 3.8 \times 10^{-1} \text{ cm}^2/\text{Vs}$ for **P1**.

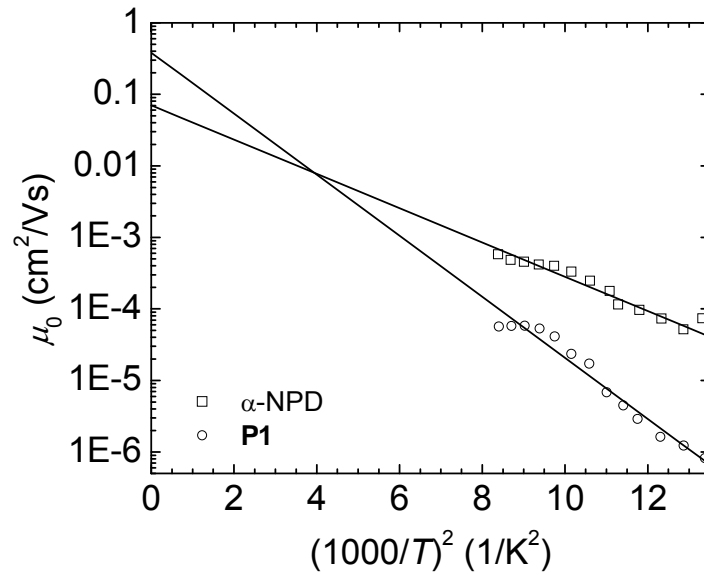


Figure 7.7. Plot of zero-field mobility versus $(1000/T)^2$ for organic diodes consisting of α -NPD (100 nm, squares) and **P1** (90 nm, circles). Experimental data is shown as empty symbols; solid lines are linear fits to this data.

Table 7.2. Saturation current density J_0 , ideality factor n , parallel resistance R_p , zero-field mobility μ_0 , and mobility field-dependence factor β , all resulting from fits of the model to electrical characteristics at room temperature for organic diodes with thickness L . For pentacene and C_{60} diodes, the series resistance R_s is noted instead of any mobility. The effective Richardson constant A^* and the injection barrier Φ_B were extrapolated from current measurements at different temperatures.

	L (nm)	J_0 (mA/cm ²)	n ()	R_p ($\Omega^*\text{cm}^2$)	μ_0 (cm ² /Vs)	β (cm/V) ^{1/2})	R_s ($\Omega^*\text{cm}^2$)	A^* (A/(cm ² *K ²))	Φ_B (eV)
α -NPD	100	1.8×10^{-14}	1.9	8.7×10^8	1.2×10^{-4}	1.5×10^{-3}	N/A	1.9×10^{-5}	0.99
P1	90	1.5×10^{-14}	2.2	1.3×10^6	4.5×10^{-6}	2.8×10^{-3}	N/A	-	-
Pentacene	80	7.7×10^{-4}	1.6	1.7×10^6	N/A	N/A	1.4	1.2×10^{-4}	0.42
C_{60}	100	3.6×10^{-9}	1.7	2.7×10^4	N/A	N/A	1.1	1.8×10^{-5}	0.72

Despite the good agreement of the proposed model for the previous diodes, some adjustments to the equivalent circuit were necessary to fit the electrical characteristics of diodes based on pentacene and C_{60} . Typically, organic semiconductors show ohmic behavior before space-charge limited current occurs. Combining Equation (2.12) with the equation for ohmic drift current

$$J = n_0 e \mu \frac{V}{L} \quad (2.11)$$

where e is the elementary charge and n_0 the charge carrier density, a crossover voltage V_C from ohmic to space-charge limited current can be calculated yielding

$$V_C = \frac{8}{9} \frac{e}{\epsilon} L^2 n_0 \quad (7.2)$$

with

$$n_0 \propto \exp\left(-\frac{E_g}{2kT}\right) \quad (7.3)$$

where E_g is the bandgap of the material. From equation (7.2), it can be seen that the crossover voltage between the ohmic and SCLC regimes increases for materials with smaller bandgaps such as pentacene and C_{60} . Hence, ohmic (linear) drift current can still be observed at higher voltages in diodes based on pentacene or C_{60} (E_g : 1.9 eV and 1.7 eV, for pentacene and C_{60} [48], respectively) compared to diodes based on α -NPD or TPD (E_g : 3.1 eV and 3.2 eV, for α -NPD [197] and TPD [182], respectively). In fact, by replacing the SCLC resistor in our model with a constant resistor R_s , good fits to the experimental data of pentacene and C_{60} diodes can be achieved (see Figure 7.8), which has already been shown in equivalent circuits of pentacene/ C_{60} organic photovoltaic cells [198]. However, no mobility values can be determined from R_s since both the charge carrier concentration n_0 and the mobility μ are unknown in the equation for R_s :

$$R_s = \frac{L}{n_0 e \mu}. \quad (7.4)$$

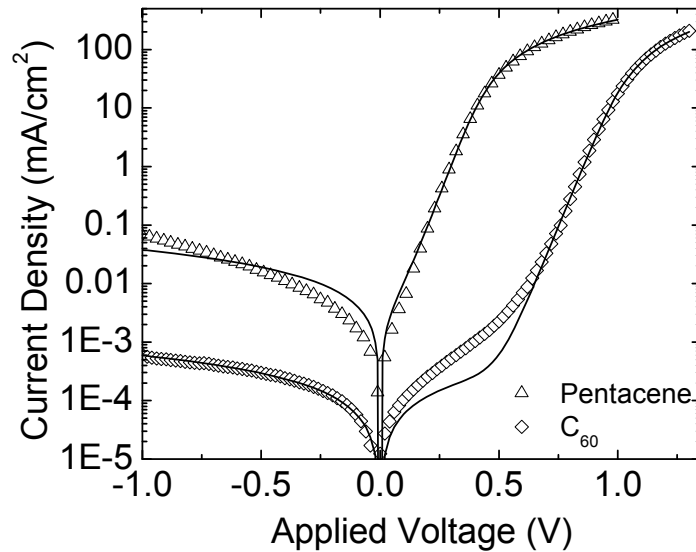


Figure 7.8. Current density as a function of the applied voltage at room temperature for organic diodes with organic layers of pentacene (80 nm, triangles) and C₆₀ (100 nm)/BCP (8 nm, diamonds). Experimental data is shown as empty symbols; solid lines represent the simulated curves.

Finally, to calculate the injection barrier and the effective Richardson constant, current density measurements in single-layer diodes were performed as a function of temperature (see Figure 7.6 for α -NPD and Figure 7.9 for pentacene diodes). By plotting the logarithm of (J_0/T^2) versus $(1/kT)$, the injection barrier and the effective Richardson constant can be determined from the slope and the intercept, respectively, of a linear fit to the experimental data as a function of temperature, as shown in Figure 7.10. Calculated values of the fitted parameters are summarized in Table 7.2. Note that data from diodes incorporating **P1** did not yield a linear fit. Hence, the values of the effective Richardson constant and the injection barrier energy could not be extracted.

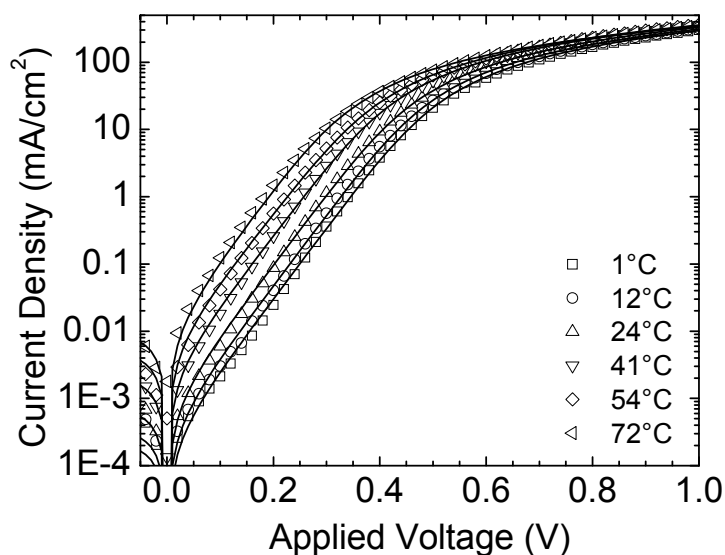


Figure 7.9. Current density as a function of the applied voltage for a pentacene diode with a thickness of 80 nm measured at temperatures ranging from 1 °C to 72 °C. Experimental data is shown as empty symbols; solid lines represent the simulated curves.

All calculated effective Richardson constants were in the range of 10^{-5} to 10^{-4} A/(cm²K²), which is in the upper range of experimentally determined effective Richardson constants in organic materials [182, 199, 200] but below the theoretical value of $\sim 10^{-2}$ A/(cm²K²) [29]. The fitted injection barrier for the C₆₀ diodes ($\Phi_B = 0.72$ eV) seems to suggest that electrons are in fact not injected from the aluminum (work function $W = 4.2$ eV) into the C₆₀ film (LUMO: 4.5 eV [48]) through defect states in the BCP, as was mentioned in earlier reports [201]. More likely, electrons get injected into the LUMO of BCP first, since the measured injection barrier corresponds well with the barrier between aluminum and BCP (LUMO of BCP: 3.5 eV [48]).

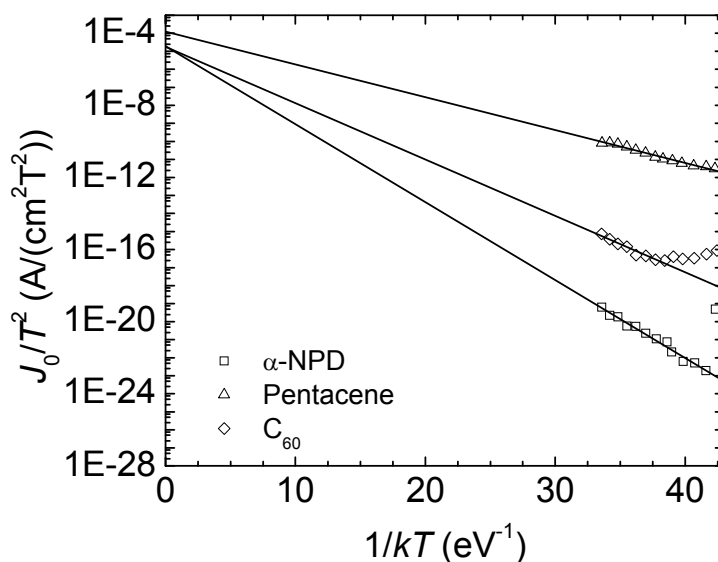


Figure 7.10. Plot of (J_0/T^2) versus $(1/kT)$ for organic diodes consisting of three different materials to extrapolate the injection barrier Φ_B and the effective Richardson constant A^* . Experimental data is shown as empty symbols; solid lines are linear fits to the data.

In the case of the α -NPD and the pentacene diodes, both values for the injection barriers that were calculated from the fits in Figure 7.10 are higher than the energy barriers that are expected between the work function of plasma treated ITO ($W = 4.7$ eV) [202] and the HOMO energies of α -NPD [197] (5.5 eV) and pentacene [48] (4.9 eV). However, similar values for the energy barrier have resulted from x-ray and ultraviolet photoemission spectroscopy (XPS and UPS) measurements [203, 204], and the increased barrier energies have been attributed to dipoles that form at the interface with ITO, which causes a vacuum level misalignment and therefore an increase in the injection barrier.

CHAPTER 8

CONCLUSIONS AND OUTLOOK

8.1 Conclusions

In summary, this work reports on the fabrication of OLEDs with solution-processed organic layers. Whereas chapter 4 and 5 still require the thermal evaporation of one or two organic layers, all organic layers of the devices shown in chapter 6 were deposited from solution.

In chapter 4, it has been shown that the efficiency in devices based on an evaporated emissive layer of CBP:Ir(ppy)₃ can be improved by using solution-processed hole-transport materials with higher ionization potentials and lower hole mobilities. Furthermore, even higher efficiencies were achieved in a simplified 3-layer device architecture where BCP was used as the hole-blocking and electron-transport material simultaneously. A device structure with ITO/PVK/CBP:Ir(ppy)₃/BCP/LiF/Al showed an improved EQE of 21.2% (72 cd/A) at 100 cd/m², which is the highest efficiency that has been for a device with less than four organic layers. Furthermore, this device structure requires the deposition of only two organic layers from the vapor phase.

In chapter 5, OLED devices with a solution-processed hole-transport layer and a copolymer based emissive layer have been shown where the copolymers had bis(carbazolyl)fluorene charge-transport groups and phosphorescent iridium complexes in the side-chains. By incorporating phosphorescent complexes with different ligands, the photoluminescence spectrum of the copolymer was tuned, and devices with four different

electroluminescence spectra were presented where the OLEDs based on copolymers with orange/red emission showed higher efficiency than the devices with blue/green emission.

Furthermore, the orange copolymer that showed the highest efficiency in this initial screening was further optimized by introducing systematic changes to the chemical nature of the polymer, and the effects of the changes on the efficiencies of OLEDs were measured. The molecular weight of the copolymer only displayed significant influence on the efficiency of the device at high molecular weights (>70 kDa). More significant changes in the efficiency could be observed when the loading level of the iridium group was varied. The highest efficiencies were measured in OLEDs based on copolymers with an iridium loading level around 5 mol%. Improvements were found when different linkers were used between the side-chains and the polymer backbone. Introducing an ester group into the linker between the hole-transport group and the polymer backbone helped to increase the efficiency. Furthermore, the replacement of the short linkage between the iridium complex and the polymer backbone with a longer carbon chain led to an even larger improvement. Efficiencies of $4.9 \pm 0.4\%$ at 100 cd/m^2 were measured in optimized devices. This is the first study of all these effects on one copolymer system. Moreover, there is only a handful of reports about OLEDs incorporating copolymers as the emissive layers where higher efficiencies have been reported.

In chapter 6, using a photocrosslinkable hole-transport polymer and a photocrosslinkable polymeric orange-emitting layer, solution-processed multilayer OLEDs were fabricated. For these devices, newly synthesized electron-transport polymers based on small molecules with good electron charge-transport properties were used. Efficiencies of up to $2.0 \pm 0.2\%$ were achieved. Unlike most other reports of

solution-processed multilayer OLEDs, this work presents a multilayer fabrication based on a crosslinkable emissive layer. It represents the first implementation of electron-transport polymers that are soluble in organic solvents whereas other electron-transport polymers are water-soluble, which is unfavorable for the lifetime of the devices since OLEDs are heavily sensitive to oxygen and water.

By photopatterning of the emissive layer, a white light source with tunable color was fabricated. The color of the light source could be tuned from blue through the white to orange. This is the first successful report of such a light source with solution-processed emissive layers where the different colors were patterned directly without the introduction of additional sacrificial layers.

Finally, in chapter 7, an equivalent-circuit model for organic diodes was proposed. The model assumes that the injection of charges from an electrode into the organic semiconductor is governed by thermionic emission. The drift current across the semiconductor is then described by a voltage-dependent resistor representing space-charge limited current (SCLC) in series with the injecting diode.

Applying this model to the experimental data of two single-layer diodes consisting of either α -NPD or a TPD-based polymer returned mobilities that are similar to published results. Furthermore, the extracted values are consistent with the disorder formalism of the mobility, which was confirmed by temperature dependent measurements of the electrical characteristics.

For pentacene and C_{60} diodes, the equivalent circuit had to be modified by replacing the voltage-dependent resistor with a constant resistor to represent the ohmic drift current that can be observed in such diodes due to the small bandgap of the two

materials. No information about the mobility values could be gained from this model since the current within the considered voltage range did not reach an SCLC regime in these devices with lower-bandgap materials.

Finally, effective Richardson constants and injection barrier energies could also be extracted from temperature dependence measurements of the electrical characteristics of the diodes. Both parameters were in good agreement with measured parameters in the literature.

Combining these results, it has been shown that the proposed equivalent circuit is a simple but reliable model to simulate organic single-layer diodes. The model is mainly based on parameters that can be extracted from independent experiments, such as mobility or UPS measurements. With the implementation of the equivalent circuit in SPICE, the model can also be readily used in circuit optimizations. However, it has to be noted that the proposed model at this stage does not fit well for high-efficiency OLEDs comprised of multiple layers and that further refinements to the current model will be required.

8.2 Outlook

Since devices with PVK as a hole-transport material resulted in the highest efficiency for the devices that were shown in chapter 4, OLEDs with a solution-processed emissive layer as shown in chapter 5 and 6 are potentially more efficient if a crosslinkable hole-transport material with an ionization potential and a mobility comparable to PVK were to be used. However, because of the wide bandgap of carbazole compounds, they absorb in the same range as the cinnamate crosslinking group that was

used in this work for photocrosslinkable materials. Therefore, photocrosslinking is not suitable for carbazole compounds since high UV exposure doses are necessary for crosslinking (see chapter 6). Thus, different crosslinking methods, such as thermal crosslinking, will have to be pursued.

While good efficiencies have been shown for copolymers that incorporated an orange phosphorescent emitter, copolymers with a green and blue emitter yielded only low efficiencies. It can be assumed that an optimization of the green and blue copolymers similar to the optimization of the orange copolymer will lead to higher efficiencies for those two colors, too. However, it is possible that the low efficiencies in the green and the blue copolymers result from bad energy transfer from the host materials to the phosphorescent emitter and different host monomers might have to be incorporated into the copolymers to achieve higher efficiencies.

For high efficiency in OLEDs with solution-processed organic layers only, photocrosslinking of the emissive copolymers is not suitable either because of the high UV exposure doses that are necessary to crosslink the copolymer, similarly to the carbazole compounds as hole-transport materials. Likewise, it is therefore necessary to pursue other crosslinking methods although the advantage of easy patternability is lost.

Finally, the equivalent circuit that has been introduced for single-layer diodes will have to be expanded for organic light-emitting diodes to include a circuit element that represents the recombination in the diode. This additional element has a very significant influence on the current flow in highly efficient devices where almost all electrons recombine and the space-charge limited current across the device becomes negligible.

8.3 List of Publications

A. Haldi, B. Domercq, B. Kippelen, R. D. Hreha, J. Y. Cho, and S. R. Marder, "Highly efficient green phosphorescent organic light-emitting diodes with simplified device geometry," *Applied Physics Letters*, vol. 92, p. 253502, 2008.

A. Haldi, A. Kimyonok, B. Domercq, L. E. Hayden, S. C. Jones, S. R. Marder, M. Weck, and B. Kippelen, "Optimization of orange-emitting electrophosphorescent copolymers for organic light-emitting diodes," *Advanced Functional Materials*, 2008, accepted.

A. Haldi, A. Sharma, W. J. Potscavage Jr., and B. Kippelen, "Equivalent circuit model for organic single-layer diodes," *Journal of Applied Physics*, 2008, accepted.

A. Haldi, J. B. Kim, B. Domercq, A. P. Kulkarni, S. Barlow, A. P. Gifford, S. A. Jenekhe, S. R. Marder, and B. Kippelen, "Fabrication of a blue $M \times N$ pixel organic light-emitting diode video display incorporating a thermally stable emitter," *Journal of Display Technology*, 2008, submitted.

APPENDIX - DEVICE FABRICATION

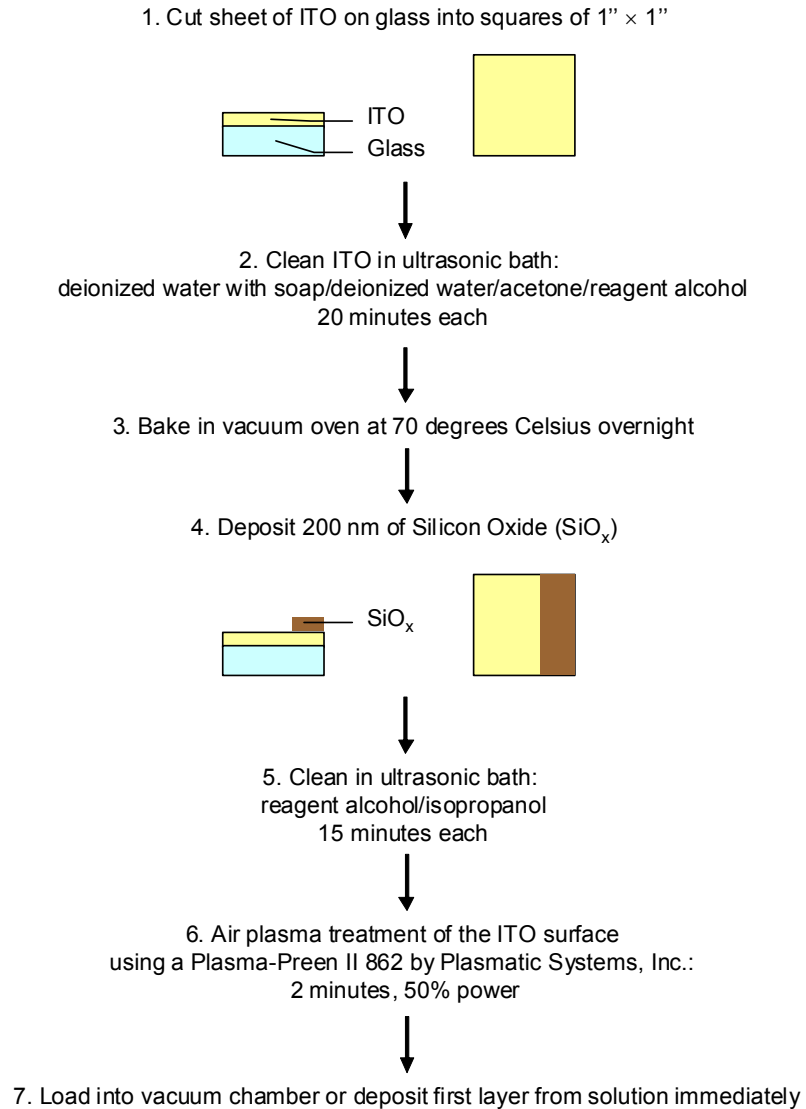


Figure A-1. Diagram of the substrate cleaning process.

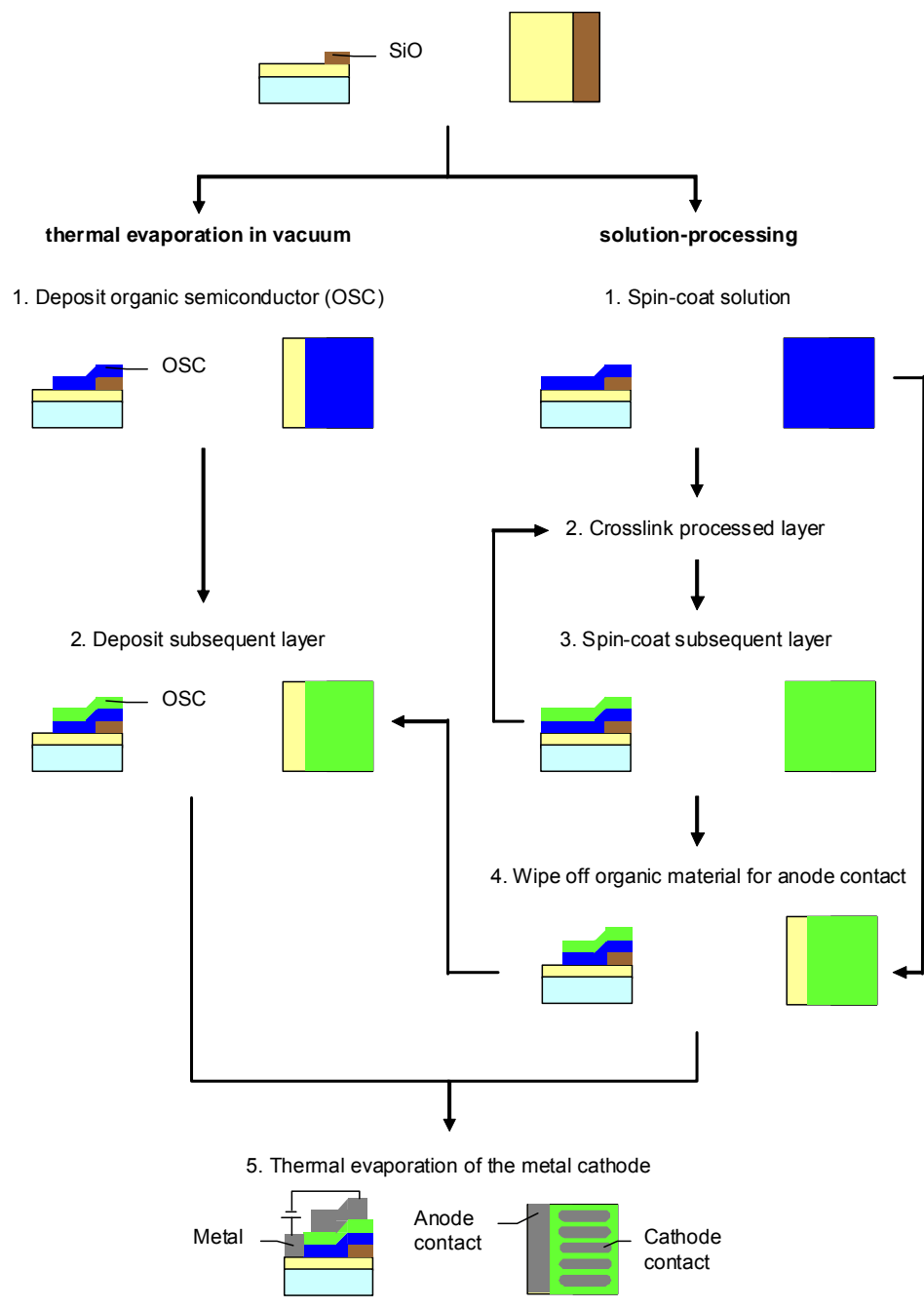


Figure A-2. Diagram of the OLED device fabrication process.

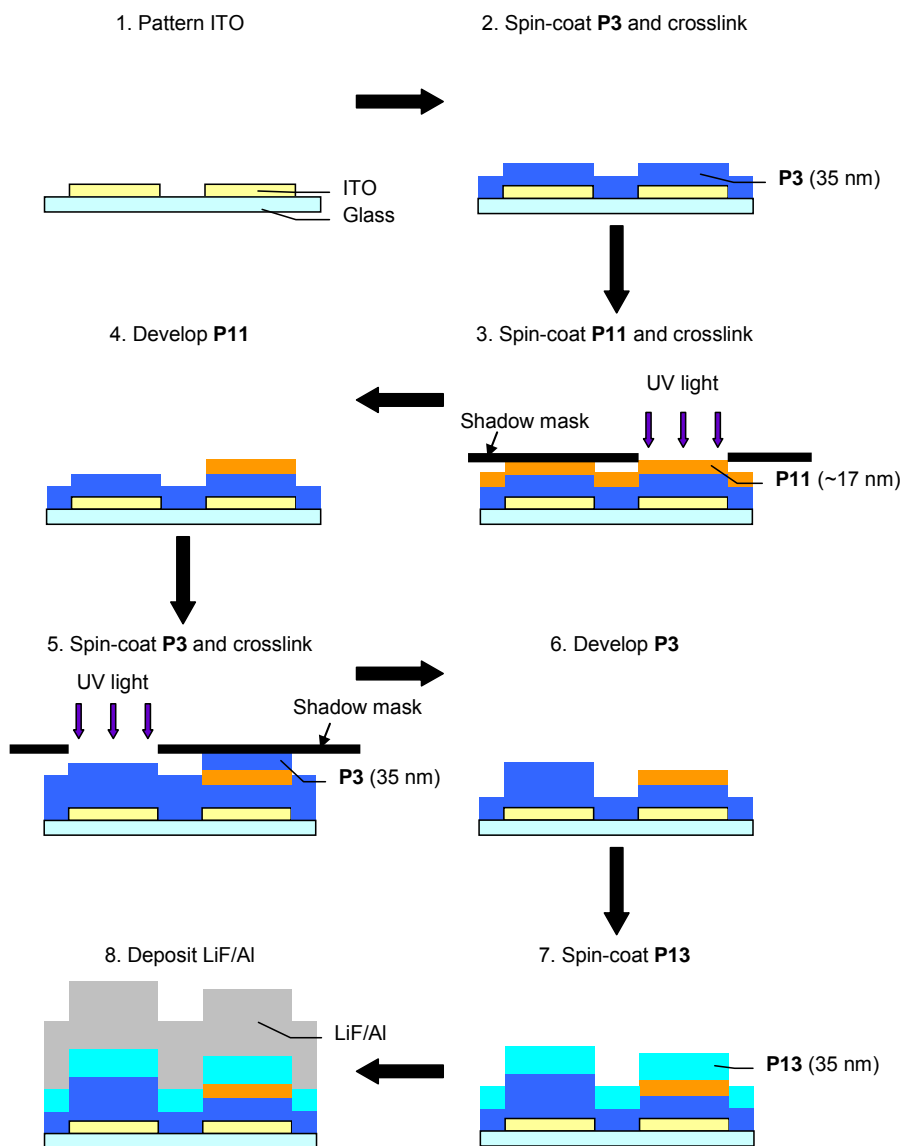


Figure A-3. Diagram of the fabrication process for patterned solution-processed multilayer OLEDs.

REFERENCES

- [1] www.sony.com (accessed June 2008).
- [2] www.novaled.com (accessed June 2008).
- [3] www.universaldisplay.com (accessed June 2008).
- [4] A. Bernanose, "Electroluminescence of organic compounds," *British Journal of Applied Physics*, pp. S54-S56, 1955.
- [5] M. Pope, P. Magnante, and H. P. Kallmann, "Electroluminescence in organic crystals," *Journal of Chemical Physics*, vol. 38, pp. 2042-2043, 1963.
- [6] P. S. Vincett, W. A. Barlow, R. A. Hann, and G. G. Roberts, "Electrical conduction and low voltage blue electroluminescence in vacuum-deposited organic films," *Thin Solid Films*, vol. 94, pp. 171-183, 1982.
- [7] C. W. Tang and S. A. Vanslyke, "Organic electroluminescent diodes," *Applied Physics Letters*, vol. 51, pp. 913-915, 1987.
- [8] J. H. Burroughes, D. D. C. Bradley, A. R. Brown, R. N. Marks, K. Mackay, R. H. Friend, P. L. Burns, and A. B. Holmes, "Light-emitting-diodes based on conjugated polymers," *Nature*, vol. 347, pp. 539-541, 1990.
- [9] M. A. Baldo, D. F. O'Brien, Y. You, A. Shoustikov, S. Sibley, M. E. Thompson, and S. R. Forrest, "Highly efficient phosphorescent emission from organic electroluminescent devices," *Nature*, vol. 395, pp. 151-154, 1998.
- [10] S. C. Chang, J. Liu, J. Bharathan, Y. Yang, J. Onohara, and J. Kido, "Multicolor organic light-emitting diodes processed by hybrid inkjet printing," *Advanced Materials*, vol. 11, pp. 734-737, 1999.
- [11] D. A. Pardo, G. E. Jabbour, and N. Peyghambarian, "Application of screen printing in the fabrication of organic light-emitting devices," *Advanced Materials*, vol. 12, pp. 1249-1252, 2000.
- [12] D. F. O'Brien, P. E. Burrows, S. R. Forrest, B. E. Koene, D. E. Loy, and M. E. Thompson, "Hole transporting materials with high glass transition temperatures for use in organic light-emitting devices," *Advanced Materials*, vol. 10, pp. 1108-1112, 1998.
- [13] E. Bellmann, S. E. Shaheen, R. H. Grubbs, S. R. Marder, B. Kippelen, and N. Peyghambarian, "Organic two-layer light-emitting diodes based on high- T_g hole-transporting polymers with different redox potentials," *Chemistry of Materials*, vol. 11, pp. 399-407, 1999.

- [14] www.polyic.com (accessed June 2008).
- [15] www.ge.com (accessed June 2008).
- [16] CIE, *Commission Internationale de l'Eclairage Proceedings, 1931*. Cambridge: Cambridge University Press, 1932.
- [17] M. Abkowitz, I. Chen, and J. H. Sharp, "Electron spin resonance of the organic semiconductor alpha-copper phtalocyanine," *Journal of Chemical Physics*, vol. 48, pp. 4561-4567, 1968.
- [18] N. Almeleh and S. E. Harrison, "Trapping effects in the organic semiconductor triphenylene," *Journal of Physics and Chemistry of Solids*, vol. 27, pp. 893-901, 1966.
- [19] J. McGinnes, P. Corry, and P. Proctor, "Amorphous-semiconductor switching in melanins," *Science*, vol. 183, pp. 853-855, 1974.
- [20] H. Shirakawa, E. J. Louis, A. G. Macdiarmid, C. K. Chiang, and A. J. Heeger, "Synthesis of electrically conducting organic polymers - halogen derivatives of polyacetylene, (CH)_x," *Journal of the Chemical Society-Chemical Communications*, pp. 578-580, 1977.
- [21] T. W. Kelley, P. F. Baude, C. Gerlach, D. E. Ender, D. Muyres, M. A. Haase, D. E. Vogel, and S. D. Theiss, "Recent progress in organic electronics: Materials, devices, and processes," *Chemistry of Materials*, vol. 16, pp. 4413-4422, 2004.
- [22] N. J. Haddock, B. Domercq, and B. Kippelen, "High mobility C₆₀ organic field-effect transistors," *Electronics Letters*, vol. 41, pp. 444-446, 2005.
- [23] S. F. Nelson, Y. Y. Lin, D. J. Gundlach, and T. N. Jackson, "Temperature-independent transport in high-mobility pentacene transistors," *Applied Physics Letters*, vol. 72, pp. 1854-1856, 1998.
- [24] D. W. Oxtoby, W. A. Freeman, and T. F. Block, *Chemistry: Science of Change*, 4th ed. Pacific Grove: Thomson-Brooks, 2003.
- [25] M. Pope and C. E. Swenberg, *Electronic Processes in Organic Crystals and Polymers*, 2nd ed. New York: Oxford Science Publications, 1999.
- [26] J. L. Bredas, J. P. Calbert, D. A. da Silva, and J. Cornil, "Organic semiconductors: A theoretical characterization of the basic parameters governing charge transport," *Proceedings of the National Academy of Sciences of the United States of America*, vol. 99, pp. 5804-5809, 2002.
- [27] W. R. Silveira and J. A. Marohn, "Microscopic view of charge injection in an organic semiconductor," *Physical Review Letters*, vol. 93, p. 116104, 2004.

- [28] D. Braun, "Electronic injection and conduction processes for polymer devices," *Journal of Polymer Science Part B-Polymer Physics*, vol. 41, pp. 2622-2629, 2003.
- [29] J. C. Scott and G. G. Malliaras, "Charge injection and recombination at the metal-organic interface," *Chemical Physics Letters*, vol. 299, pp. 115-119, 1999.
- [30] E. M. Conwell and M. W. Wu, "Contact injection into polymer light-emitting diodes," *Applied Physics Letters*, vol. 70, pp. 1867-1869, 1997.
- [31] K. Harada, A. G. Werner, M. Pfeiffer, C. J. Bloom, C. M. Elliott, and K. Leo, "Organic homojunction diodes with a high built-in potential: Interpretation of the current-voltage characteristics by a generalized Einstein relation," *Physical Review Letters*, vol. 94, p. 036601, 2005.
- [32] I. H. Campbell and B. K. Crone, "Characteristics of an organic light-emitting diode utilizing a phosphorescent, shallow hole trap," *Applied Physics Letters*, vol. 89, p. 172108, 2006.
- [33] R. F. Pierret, *Semiconductor Device Fundamentals*, 2nd ed. Reading, MA: Addison-Wesley, 1996.
- [34] R. A. Marcus, "Theory of oxidation-reduction reactions involving electron transfer," *Journal of Chemical Physics*, vol. 24, pp. 966-978, 1956.
- [35] K. Sakanoue, M. Motoda, M. Sugimoto, and S. Sakaki, "A molecular orbital study on the hole transport property of organic amine compounds," *Journal of Physical Chemistry A*, vol. 103, pp. 5551-5556, 1999.
- [36] H. Bassler, "Charge transport in disordered organic photoconductors - a Monte-Carlo simulation study," *Physica Status Solidi B-Basic Research*, vol. 175, pp. 15-56, 1993.
- [37] P. M. Borsenberger, L. Pautmeier, and H. Bassler, "Charge transport in disordered molecular solids," *The Journal of Chemical Physics*, vol. 94, pp. 5447-5454, 1991.
- [38] V. Coropceanu, J. Cornil, D. A. da Silva, Y. Olivier, R. Silbey, and J. L. Bredas, "Charge transport in organic semiconductors," *Chemical Reviews*, vol. 107, pp. 926-952, 2007.
- [39] A. Miller and E. Abrahams, "Impurity conduction at low concentrations," *Physical Review*, vol. 120, pp. 745-755, 1960.
- [40] R. Coehoorn, W. F. Pasveer, P. A. Bobbert, and M. A. J. Michels, "Charge-carrier concentration dependence of the hopping mobility in organic materials with Gaussian disorder," *Physical Review B*, vol. 72, p. 155206, 2005.

- [41] P. M. Borsenberger, W. T. Gruenbaum, and E. H. Magin, "Hole transport in vapor deposited bis(ditolylaminostyryl)benzene," *Physica B-Condensed Matter*, vol. 228, pp. 226-232, 1996.
- [42] R. H. Parmenter and W. Ruppel, "2-carrier space-charge-limited current in a trap-free insulator," *Journal of Applied Physics*, vol. 30, pp. 1548-1558, 1959.
- [43] M. A. Lampert and P. Mark, *Current Injection in Solids*. New York: Academic Press, 1970.
- [44] P. Mark and W. Helfrich, "Space-charge-limited currents in organic crystals," *Journal of Applied Physics*, vol. 33, pp. 205-215, 1962.
- [45] P. N. Murgatroyd, "Theory of space-charge-limited current enhanced by Frenkel effect," *Journal of Physics D-Applied Physics*, vol. 3, pp. 151-156, 1970.
- [46] P. Langevin, "The ionisation of gases," *Annales de Chimie et de Physique*, vol. 28, pp. 289-384, 1903.
- [47] I. Kamohara, M. Townsend, and B. Cottle, "Simulation of heterojunction organic thin film devices and exciton diffusion analysis in stacked-hetero device," *Journal of Applied Physics*, vol. 97, p. 014501, 2005.
- [48] S. Yoo, B. Domercq, and B. Kippelen, "Efficient thin-film organic solar cells based on pentacene/C₆₀ heterojunctions," *Applied Physics Letters*, vol. 85, pp. 5427-5429, 2004.
- [49] H. Bassler, Y. H. Tak, D. V. Khramtchenkov, and V. R. Nikitenko, "Models of organic light-emitting diodes," *Synthetic Metals*, vol. 91, pp. 173-179, 1997.
- [50] D. J. Griffiths, *Introduction to Quantum Mechanics*, 2nd ed. Upper Saddle River, NJ: Pearson Prentice Hall, 2005.
- [51] D. Beljonne, Z. G. Shuai, A. J. Ye, and J. L. Bredas, "Charge-recombination processes in oligomer- and polymer-based light-emitting diodes: A molecular picture," *Journal of the Society for Information Display*, vol. 13, pp. 419-427, 2005.
- [52] D. S. McClure, "Selection rules for singlet-triplet perturbations in polyatomic molecules," *Journal of Chemical Physics*, vol. 17, pp. 665-666, 1949.
- [53] R. S. Becker, *Theory and Interpretation of Fluorescence and Phosphorescence*. New York: Wiley Interscience, 1969.
- [54] R. C. Evans, P. Douglas, and C. J. Winscom, "Coordination complexes exhibiting room-temperature phosphorescence: Evaluation of their suitability as triplet emitters in organic light emitting diodes," *Coordination Chemistry Reviews*, vol. 250, pp. 2093-2126, 2006.

- [55] M. A. Baldo, C. Adachi, and S. R. Forrest, "Transient analysis of organic electrophosphorescence. II. Transient analysis of triplet-triplet annihilation," *Physical Review B*, vol. 62, pp. 10967-10977, 2000.
- [56] M. A. Baldo, S. Lamansky, P. E. Burrows, M. E. Thompson, and S. R. Forrest, "Very high-efficiency green organic light-emitting devices based on electrophosphorescence," *Applied Physics Letters*, vol. 75, pp. 4-6, 1999.
- [57] M. Kesslinger and J. Michl, *Excited States and Photochemistry of Organic Molecules*. New York: VCH Publishers, 1995.
- [58] G. Ramos-Ortiz, Y. Oki, B. Domercq, and B. Kippelen, "Forster energy transfer from a fluorescent dye to a phosphorescent dopant: a concentration and intensity study," *Physical Chemistry Chemical Physics*, vol. 4, pp. 4109-4114, 2002.
- [59] C. Adachi, M. A. Baldo, M. E. Thompson, and S. R. Forrest, "Nearly 100% internal phosphorescence efficiency in an organic light-emitting device," *Journal of Applied Physics*, vol. 90, pp. 5048-5051, 2001.
- [60] M. A. Baldo, D. F. O'Brien, M. E. Thompson, and S. R. Forrest, "Excitonic singlet-triplet ratio in a semiconducting organic thin film," *Physical Review B*, vol. 60, pp. 14422-14428, 1999.
- [61] E. A. Meulenkaamp, R. van Aar, J. J. A. M. Bastiaansen, A. J. van den Biggelaar, H. Borner, K. Brunner, M. Buchel, A. van Dijken, N. M. M. Kikken, M. Kilitziraki, M. M. de Kok, B. M. Langeveld, M. P. H. Ligter, S. I. E. Vulto, P. van de Weijer, and S. H. P. M. de Winter, "High-efficiency polymer LEDs: triplets and novel devices," *Proceedings of SPIE-The International Society of Optical Engineering*, vol. 5464, pp. 90-103, 2004.
- [62] D. Beljonne, A. J. Ye, Z. Shuai, and J. L. Bredas, "Chain-length dependence of singlet and triplet exciton formation rates in organic light-emitting diodes," *Advanced Functional Materials*, vol. 14, pp. 684-692, 2004.
- [63] S. Lamansky, R. C. Kwong, M. Nugent, P. I. Djurovich, and M. E. Thompson, "Molecularly doped polymer light emitting diodes utilizing phosphorescent Pt(II) and Ir(III) dopants," *Organic Electronics*, vol. 2, pp. 53-62, 2001.
- [64] B. Krummacher, M. K. Mathai, V. E. Choong, S. A. Choulis, F. So, and A. Winnacker, "Influence of charge balance and microcavity effects on resultant efficiency of organic-light emitting devices," *Organic Electronics*, vol. 7, pp. 313-318, 2006.
- [65] L. S. Hung, C. W. Tang, and M. G. Mason, "Enhanced electron injection in organic electroluminescence devices using an Al/LiF electrode," *Applied Physics Letters*, vol. 70, pp. 152-154, 1997.

- [66] J.-M. Moon, J.-H. Bae, J.-A. Jeong, S.-W. Jeong, N.-J. Park, H.-K. Kim, J.-W. Kang, J.-J. Kim, and M.-S. Yi, "Enhancement of hole injection using ozone treated Ag nanodots dispersed on indium tin oxide anode for organic light emitting diodes," *Applied Physics Letters*, vol. 90, p. 163516, 2007.
- [67] Y. Cao, I. D. Parker, G. Yu, C. Zhang, and A. J. Heeger, "Improved quantum efficiency for electroluminescence in semiconducting polymers," *Nature*, vol. 397, pp. 414-417, 1999.
- [68] X. H. Yang, D. C. Muller, D. Neher, and K. Meerholz, "Highly efficient polymeric electrophosphorescent diodes," *Advanced Materials*, vol. 18, pp. 948-954, 2006.
- [69] K. M. Vaeth and C. W. Tang, "Light-emitting diodes based on phosphorescent guest/polymeric host systems," *Journal of Applied Physics*, vol. 92, pp. 3447-3453, 2002.
- [70] G. He, M. Pfeiffer, K. Leo, M. Hofmann, J. Birnstock, R. Pudzich, and J. Salbeck, "High-efficiency and low-voltage p-i-n electrophosphorescent organic light-emitting diodes with double-emission layers," *Applied Physics Letters*, vol. 85, pp. 3911-3913, 2004.
- [71] J. S. Kim, P. K. H. Ho, N. C. Greenham, and R. H. Friend, "Electroluminescence emission pattern of organic light-emitting diodes: Implications for device efficiency calculations," *Journal of Applied Physics*, vol. 88, pp. 1073-1081, 2000.
- [72] B. E. A. Saleh and M. C. Teich, *Fundamentals of Photonics*, 2nd ed. New York: Wiley-Interscience, 2007.
- [73] G. Gu, D. Z. Garbuzov, P. E. Burrows, S. Venkatesh, S. R. Forrest, and M. E. Thompson, "High-external-quantum-efficiency organic light-emitting devices," *Optics Letters*, vol. 22, pp. 396-398, 1997.
- [74] W. Holzer, A. Penzkofer, and T. Tsuboi, "Absorption and emission spectroscopic characterization of Ir(ppy)₃," *Chemical Physics*, vol. 308, pp. 93-102, 2005.
- [75] L. H. Smith, J. A. E. Wasey, I. D. W. Samuel, and W. L. Barnes, "Light out-coupling efficiencies of organic light-emitting diode structures and the effect of photoluminescence quantum yield," *Advanced Functional Materials*, vol. 15, pp. 1839-1844, 2005.
- [76] K. Meerholz and D. C. Muller, "Outsmarting waveguide losses in thin-film light-emitting diodes," *Advanced Functional Materials*, vol. 11, pp. 251-253, 2001.
- [77] H. Greiner, "Light extraction from organic light emitting diode substrates: Simulation and experiment," *Japanese Journal of Applied Physics Part I-Regular Papers Brief Communications & Review Papers*, vol. 46, pp. 4125-4137, 2007.

- [78] M. Agrawal, Y. Sun, S. R. Forrest, and P. Peumans, "Enhanced outcoupling from organic light-emitting diodes using aperiodic dielectric mirrors," *Applied Physics Letters*, vol. 90, p. 241112, 2007.
- [79] B. C. Krummacher, M. K. Mathai, V. Choong, S. A. Choulis, F. So, and A. Winnacker, "General method to evaluate substrate surface modification techniques for light extraction enhancement of organic light emitting diodes," *Journal of Applied Physics*, vol. 100, p. 054702, 2006.
- [80] C. F. Madigan, M. H. Lu, and J. C. Sturm, "Improvement of output coupling efficiency of organic light-emitting diodes by backside substrate modification," *Applied Physics Letters*, vol. 76, pp. 1650-1652, 2000.
- [81] T. Tsutsui, M. Yahiro, H. Yokogawa, K. Kawano, and M. Yokoyama, "Doubling coupling-out efficiency in organic light-emitting devices using a thin silica aerogel layer," *Advanced Materials*, vol. 13, pp. 1149-1152, 2001.
- [82] H. Riel, S. Karg, T. Beierlein, B. Ruhstaller, and W. Riess, "Phosphorescent top-emitting organic light-emitting devices with improved light outcoupling," *Applied Physics Letters*, vol. 82, pp. 466-468, 2003.
- [83] T. Dobbertin, M. Kroeger, D. Heithecker, D. Schneider, D. Metzdorf, H. Neuner, E. Becker, H. H. Johannes, and W. Kowalsky, "Inverted top-emitting organic light-emitting diodes using sputter-deposited anodes," *Applied Physics Letters*, vol. 82, pp. 284-286, 2003.
- [84] Q. Huang, S. Reineke, K. Walzer, M. Pfeiffer, and K. Leo, "Quantum efficiency enhancement in top-emitting organic light-emitting diodes as a result of enhanced intrinsic quantum yield," *Applied Physics Letters*, vol. 89, p. 263512, 2006.
- [85] L. H. Smith, J. A. E. Wasey, and W. L. Barnes, "Light outcoupling efficiency of top-emitting organic light-emitting diodes," *Applied Physics Letters*, vol. 84, pp. 2986-2988, 2004.
- [86] G. Wyszecki and W. S. Stiles, *Color Science: Concepts and Methods, Quantitative Data, and Formulae*, 2nd ed. New York: Wiley-Interscience, 2000.
- [87] T. Wakimoto, Y. Fukuda, K. Nagayama, A. Yokoi, H. Nakada, and M. Tsuchida, "Organic EL cells using alkaline metal compounds as electron injection materials," *IEEE Transactions on Electron Devices* vol. 44, pp. 1245-1248, 1997.
- [88] T. Tsutsui, M. J. Yang, M. Yahiro, K. Nakamura, T. Watanabe, T. Tsuji, Y. Fukuda, T. Wakimoto, and S. Miyaguchi, "High quantum efficiency in organic light-emitting devices with iridium-complex as a triplet emissive center," *Japanese Journal of Applied Physics Part 2-Letters*, vol. 38, pp. L1502-L1504, 1999.

- [89] D. Tanaka, H. Sasabe, Y. J. Li, S. J. Su, T. Takeda, and J. Kido, "Ultra high efficiency green organic light-emitting devices," *Japanese Journal of Applied Physics Part 2-Letters & Express Letters*, vol. 46, pp. L10-L12, 2007.
- [90] A. Fukase, K. Luan, T. Dao, and J. Kido, "High-efficiency organic electroluminescent devices using iridium complex emitter and arylamine-containing polymer buffer layer," *Polymers for Advanced Technologies*, vol. 13, pp. 601-604, 2002.
- [91] M. Ikai, S. Tokito, Y. Sakamoto, T. Suzuki, and Y. Taga, "Highly efficient phosphorescence from organic light-emitting devices with an exciton-block layer," *Applied Physics Letters*, vol. 79, pp. 156-158, 2001.
- [92] R. D. Hreha, Y. D. Zhang, B. Domercq, N. Larribeau, J. N. Haddock, B. Kippelen, and S. R. Marder, "Synthesis of photo-crosslinkable hole-transport polymers with tunable oxidation potentials and their use in organic light-emitting diodes," *Synthesis-Stuttgart*, vol. 9, pp. 1201-1212, 2002.
- [93] B. Domercq, R. D. Hreha, Y. D. Zhang, A. Haldi, S. Barlow, S. R. Marder, and B. Kippelen, "Organic light-emitting diodes with multiple photocrosslinkable hole-transport layers," *Journal of Polymer Science Part B-Polymer Physics*, vol. 41, pp. 2726-2732, 2003.
- [94] J. Kido, H. Shionoya, and K. Nagai, "Single-layer white light-emitting organic electroluminescent devices based on dye-dispersed poly(*N*-vinylcarbazole)," *Applied Physics Letters*, vol. 67, pp. 2281-2283, 1995.
- [95] G. Pfister and C. H. Griffiths, "Temperature-dependence of transient hole hopping transport in disordered organic solids - carbazole polymers," *Physical Review Letters*, vol. 40, pp. 659-662, 1978.
- [96] J. H. Choi, E. S. Lee, S. H. Choi, H. K. Baik, K. M. Song, Y. S. Lim, and S.-M. Lee, "Work function increase of indium-tin-oxide surfaces by atmospheric air plasma treatment with steady-state airflow," *Journal of Vacuum Science & Technology A: Vacuum, Surfaces, and Films*, vol. 23, pp. 1479-1482, 2005.
- [97] F. Steuber, J. Staudigel, M. Stossel, J. Simmerer, and A. Winnacker, "Reduced operating voltage of organic electroluminescent devices by plasma treatment of the indium tin oxide anode," *Applied Physics Letters*, vol. 74, pp. 3558-3560, 1999.
- [98] P. Marsal, I. Avilov, D. A. da Silva Filho, J. L. Bredas, and D. Beljonne, "Molecular hosts for triplet emission in light emitting diodes: A quantum-chemical study," *Chemical Physics Letters*, vol. 392, pp. 521-528, 2004.
- [99] J. Pina, J. Seixas de Melo, H. D. Burrows, A. P. Monkman, and S. Navaratnam, "On the triplet state of poly(*N*-vinylcarbazole)," *Chemical Physics Letters*, vol. 400, pp. 441-445, 2004.

- [100] B. Domercq, R. D. Hreha, Y. D. Zhang, N. Larribeau, J. N. Haddock, C. Schultz, S. R. Marder, and B. Kippelen, "Photo-patternable hole-transport polymers for organic light-emitting diodes," *Chemistry of Materials*, vol. 15, pp. 1491-1496, 2003.
- [101] C. Giebeler, H. Antoniadis, D. D. C. Bradley, and Y. Shirota, "Influence of the hole transport layer on the performance of organic light-emitting diodes," *Journal of Applied Physics*, vol. 85, pp. 608-615, 1999.
- [102] G. E. Jabbour, J. F. Wang, and N. Peyghambarian, "High-efficiency organic electrophosphorescent devices through balance of charge injection," *Applied Physics Letters*, vol. 80, pp. 2026-2028, 2002.
- [103] N. Tamoto, C. Adachi, and K. Nagai, "Electroluminescence of 1,3,4-oxadiazole and triphenylamine-containing molecules as an emitter in organic multilayer light emitting diodes," *Chemistry of Materials*, vol. 9, pp. 1077-1085, 1997.
- [104] F. Laquai and D. Hertel, "Influence of hole transport units on the efficiency of polymer light emitting diodes," *Applied Physics Letters*, vol. 90, p. 142109, 2007.
- [105] S. Okutsu, T. Onikubo, M. Tamano, and T. Enokida, "Molecular design of hole transport material with various ionization potential for organic light-emitting diode applications," *IEEE Transactions on Electron Devices*, vol. 44, pp. 1302-1306, 1997.
- [106] Y. Wang, "Dramatic effects of hole transport layer on the efficiency of iridium-based organic light-emitting diodes," *Applied Physics Letters*, vol. 85, pp. 4848-4850, 2004.
- [107] M. A. Baldo and S. R. Forrest, "Transient analysis of organic electrophosphorescence: I. Transient analysis of triplet energy transfer," *Physical Review B*, vol. 62, pp. 10958-10966, 2000.
- [108] T. Yasuda, Y. Yamaguchi, D. C. Zou, and T. Tsutsui, "Carrier mobilities in organic electron transport materials determined from space charge limited current," *Japanese Journal of Applied Physics Part 1-Regular Papers Short Notes & Review Papers*, vol. 41, pp. 5626-5629, 2002.
- [109] S. Naka, H. Okada, H. Onnagawa, and T. Tsutsui, "High electron mobility in bathophenanthroline," *Applied Physics Letters*, vol. 76, pp. 197-199, 2000.
- [110] S. C. Lo, N. A. H. Male, J. P. J. Markham, S. W. Magennis, P. L. Burn, O. V. Salata, and I. D. W. Samuel, "Green phosphorescent dendrimer for light-emitting diodes," *Advanced Materials*, vol. 14, pp. 975-979, 2002.
- [111] P. L. Burn, S. C. Lo, and I. D. W. Samuel, "The development of light-emitting dendrimers for displays," *Advanced Materials*, vol. 19, pp. 1675-1688, 2007.

- [112] S. W. Kim, J. H. Park, S. S. Oh, D. Y. Kim, E. H. Choi, G. S. Cho, Y. H. Seo, S. O. Kang, B. Park, Y. Saito, N. Watanabe, H. Takezoe, and J. Watanabe, "Highly efficient green phosphorescent single-layered organic light-emitting devices," *Applied Physics Letters*, vol. 89, p. 213511, 2006.
- [113] F. I. Wu, H. J. Su, C. F. Shu, L. Y. Luo, W. G. Diao, C. H. Cheng, J. P. Duan, and G. H. Lee, "Tuning the emission and morphology of cyclometalated iridium complexes and their applications to organic light-emitting diodes," *Journal of Materials Chemistry*, vol. 15, pp. 1035-1042, 2005.
- [114] M. Suzuki, S. Tokito, F. Sato, T. Igarashi, K. Kondo, T. Koyama, and T. Yamaguchi, "Highly efficient polymer light-emitting devices using ambipolar phosphorescent polymers," *Applied Physics Letters*, vol. 86, p. 103507, 2005.
- [115] S. Tokito, M. Suzuki, F. Sato, M. Kamachi, and K. Shirane, "High-efficiency phosphorescent polymer light-emitting devices," *Organic Electronics*, vol. 4, pp. 105-111, 2003.
- [116] H. Y. Zhen, C. Luo, W. Yang, W. Y. Song, B. Du, J. X. Jiang, C. Y. Jiang, Y. Zhang, and Y. Cao, "Electrophosphorescent chelating copolymers based on linkage isomers of naphthylpyridine-iridium complexes with fluorene," *Macromolecules*, vol. 39, pp. 1693-1700, 2006.
- [117] C. Adachi, M. E. Thompson, and S. R. Forrest, "Architectures for efficient electrophosphorescent organic light-emitting devices," *IEEE Journal of Selected Topics in Quantum Electronics*, vol. 8, pp. 372-377, 2002.
- [118] X. Z. Jiang, A. K. Y. Jen, B. Carlson, and L. R. Dalton, "Red-emitting electroluminescent devices based on osmium-complexes-doped blend of poly(vinylnaphthalene) and 1,3,4-oxadiazole derivative," *Applied Physics Letters*, vol. 81, pp. 3125-3127, 2002.
- [119] H. Yan, Q. Huang, B. J. Scott, and T. J. Marks, "A polymer blend approach to fabricating the hole transport layer for polymer light-emitting diodes," *Applied Physics Letters*, vol. 84, pp. 3873-3875, 2004.
- [120] S. T. Zhang, Z. J. Wang, J. M. Zhao, Y. Q. Zhan, Y. Wu, Y. C. Zhou, X. M. Ding, and X. Y. Hou, "Electron blocking and hole injection: The role of N,N'-bis(naphthalen-1-yl)-N,N'-bis(phenyl)benzidine in organic light-emitting devices," *Applied Physics Letters*, vol. 84, pp. 2916-2918, 2004.
- [121] K. Meerholz, "Device physics - Enlightening solutions," *Nature*, vol. 437, pp. 327-328, 2005.
- [122] P. T. Herwig and K. Müllen, "A soluble pentacene precursor: synthesis, solid-state conversion into pentacene and application in a field-effect transistor," *Advanced Materials*, vol. 11, pp. 480-483, 1999.

- [123] X. H. Yang and D. Neher, "Polymer electrophosphorescence devices with high power conversion efficiencies," *Applied Physics Letters*, vol. 84, pp. 2476-2478, 2004.
- [124] E. Bacher, M. Bayerl, P. Rudati, N. Reckefuss, C. D. Muller, K. Meerholz, and O. Nuyken, "Synthesis and characterization of photo-cross-linkable hole-conducting polymers," *Macromolecules*, vol. 38, pp. 1640-1647, 2005.
- [125] J. P. Lu, Y. N. Jin, J. F. Ding, Y. Tao, and M. Day, "High-efficiency multilayer polymeric blue light-emitting diodes using boronate esters as cross-linking linkages," *Journal of Materials Chemistry*, vol. 16, pp. 593-601, 2006.
- [126] A. Charas, H. Alves, L. Alcacer, and J. Morgado, "Use of cross-linkable polyfluorene in the fabrication of multilayer polyfluorene-based light-emitting diodes with improved efficiency," *Applied Physics Letters*, vol. 89, p. 143519, 2006.
- [127] B. Ma, F. Lauterwasser, L. Deng, C. S. Zonte, B. J. Kim, J. M. J. Frechet, C. Borek, and M. E. Thompson, "New thermally cross-linkable polymer and its application as a hole-transporting layer for solution processed multilayer organic light emitting diodes," *Chemistry of Materials*, vol. 19, pp. 4827-4832, 2007.
- [128] E. Bellmann, S. E. Shaheen, S. Thayumanavan, S. Barlow, R. H. Grubbs, S. R. Marder, B. Kippelen, and N. Peyghambarian, "New triarylamine-containing polymers as hole transport materials in organic light-emitting diodes: Effect of polymer structure and cross-linking on device characteristics," *Chemistry of Materials*, vol. 10, pp. 1668-1676, 1998.
- [129] G. L. Wu, C. H. Yang, B. H. Fan, B. Zhang, X. M. Chen, and Y. F. Li, "Synthesis and characterization of photo-crosslinkable polyfluorene with acrylate side-chains," *Journal of Applied Polymer Science*, vol. 100, pp. 2336-2342, 2006.
- [130] S. R. Tseng, S. C. Lin, H. F. Meng, H. H. Liao, C. H. Yeh, H. C. Lai, S. F. Horng, and C. S. Hsu, "General method to solution-process multilayer polymer light-emitting diodes," *Applied Physics Letters*, vol. 88, p. 163501, 2006.
- [131] C. D. Muller, A. Falcou, N. Reckefuss, M. Rojahn, V. Wiederhirn, P. Rudati, H. Frohne, O. Nuyken, H. Becker, and K. Meerholz, "Multi-colour organic light-emitting displays by solution processing," *Nature*, vol. 421, pp. 829-833, 2003.
- [132] M. C. Gather, A. Kohnen, A. Falcou, H. Becker, and K. Meerholz, "Solution-processed full-color polymer organic light-emitting diode displays fabricated by direct photolithography," *Advanced Functional Materials*, vol. 17, pp. 191-200, 2007.
- [133] M. J. Yang and T. Tsutsui, "Use of poly(9-vinylcarbazole) as host material for iridium complexes in high-efficiency organic light-emitting devices," *Japanese Journal of Applied Physics Part 2-Letters*, vol. 39, pp. L828-L829, 2000.

- [134] S. Lamansky, P. I. Djurovich, F. Abdel-Razzaq, S. Garon, D. L. Murphy, and M. E. Thompson, "Cyclometalated Ir complexes in polymer organic light-emitting devices," *Journal of Applied Physics*, vol. 92, pp. 1570-1575, 2002.
- [135] F.-C. Chen, G. He, and Y. Yang, "Triplet exciton confinement in phosphorescent polymer light-emitting diodes," *Applied Physics Letters*, vol. 82, pp. 1006-1008, 2003.
- [136] X. H. Yang, D. Neher, D. Hertel, and T. K. Daubler, "Highly efficient single-layer polymer electrophosphorescent devices," *Advanced Materials*, vol. 16, pp. 161-166, 2004.
- [137] W. G. Zhu, Y. Q. Mo, M. Yuan, W. Yang, and Y. Cao, "Highly efficient electrophosphorescent devices based on conjugated polymers doped with iridium complexes," *Applied Physics Letters*, vol. 80, pp. 2045-2047, 2002.
- [138] J. P. J. Markham, I. D. W. Samuel, S. C. Lo, P. L. Burn, M. Weiter, and H. Bassler, "Charge transport in highly efficient iridium cored electrophosphorescent dendrimers," *Journal of Applied Physics*, vol. 95, pp. 438-445, 2004.
- [139] J. Q. Ding, J. Gao, Y. X. Cheng, Z. Y. Xie, L. X. Wang, D. G. Ma, X. B. Jing, and F. S. Wang, "Highly efficient green-emitting phosphorescent iridium dendrimers based on carbazole dendrons," *Advanced Functional Materials*, vol. 16, pp. 575-581, 2006.
- [140] A. J. Sandee, C. K. Williams, N. R. Evans, J. E. Davies, C. E. Boothby, A. Kohler, R. H. Friend, and A. B. Holmes, "Solution-processible conjugated electrophosphorescent polymers," *Journal of the American Chemical Society*, vol. 126, pp. 7041-7048, 2004.
- [141] S. J. Liu, Q. Zhao, Y. Deng, Y. J. Xia, J. Lin, Q. L. Fan, L. H. Wang, and W. Huang, " π -conjugated chelating polymers with a charged iridium complex in the backbones: Toward saturated-red phosphorescent polymer light-emitting diodes," *Journal of Physical Chemistry C*, vol. 111, pp. 1166-1175, 2007.
- [142] N. R. Evans, L. S. Devi, C. S. K. Mak, S. E. Watkins, S. I. Pascu, A. Kohler, R. H. Friend, C. K. Williams, and A. B. Holmes, "Triplet energy back transfer in conjugated polymers with pendant phosphorescent iridium complexes," *Journal of the American Chemical Society*, vol. 128, pp. 6647-6656, 2006.
- [143] C. L. Lee, N. G. Kang, Y. S. Cho, J. S. Lee, and J. J. Kim, "Polymer electrophosphorescent device: comparison of phosphorescent dye doped and coordinated systems," *Optical Materials*, vol. 21, pp. 119-123, 2003.
- [144] X. D. Wang, K. Ogino, K. Tanaka, and H. Usui, "Novel iridium complex and its copolymer with N-vinyl carbazole for electroluminescent devices," *IEEE Journal of Selected Topics in Quantum Electronics*, vol. 10, pp. 121-126, 2004.

- [145] X. Y. Wang, A. Kimyonok, and M. Weck, "Functionalization of polymers with phosphorescent iridium complexes via click chemistry," *Chemical Communications*, pp. 3933-3935, 2006.
- [146] X. Y. Wang, R. N. Prabhu, R. H. Schmehl, and M. Weck, "Polymer-based tris(2-phenylpyridine)iridium complexes," *Macromolecules*, vol. 39, pp. 3140-3146, 2006.
- [147] A. Kimyonok, B. Domercq, A. Haldi, J.-Y. Cho, J. R. Carlise, X.-Y. Wang, L. E. Hayden, S. C. Jones, S. Barlow, S. R. Marder, B. Kippelen, and M. Weck, "Norbornene-based copolymers with iridium complexes and bis(carbazolyl)fluorene groups in their side-chains and their use in light-emitting diodes," *Chemistry of Materials*, vol. 19, pp. 5602-5608, 2007.
- [148] K. Dedeian, J. M. Shi, N. Shepherd, E. Forsythe, and D. C. Morton, "Photophysical and electrochemical properties of heteroleptic tris-cyclometalated iridium(III) complexes," *Inorganic Chemistry*, vol. 44, pp. 4445-4447, 2005.
- [149] S. Lamansky, P. Djurovich, D. Murphy, F. Abdel-Razzaq, H. E. Lee, C. Adachi, P. E. Burrows, S. R. Forrest, and M. E. Thompson, "Highly phosphorescent bis-cyclometalated iridium complexes: synthesis, photophysical characterization, and use in organic light emitting diodes," *Journal of the American Chemical Society*, vol. 123, pp. 4304-4312, 2001.
- [150] R. Ragni, E. A. Plummer, K. Brunner, J. W. Hofstraat, F. Babudri, G. M. Farinola, F. Naso, and L. De Cola, "Blue emitting iridium complexes: synthesis, photophysics and phosphorescent devices," *Journal of Materials Chemistry*, vol. 16, pp. 1161-1170, 2006.
- [151] C. Yi, C. J. Yang, J. Liu, M. Xu, J. H. Wang, Q. Y. Cao, and X. C. Gao, "Red to near-infrared electrophosphorescence from an iridium complex coordinated with 2-phenylpyridine and 8-hydroxyquinoline," *Inorganica Chimica Acta*, vol. 360, pp. 3493-3498, 2007.
- [152] X. W. Zhang, Z. Chen, C. L. Yang, Z. G. Li, K. Zhang, H. Q. Yao, J. G. Qin, J. W. Chen, and Y. Cao, "Highly efficient polymer light-emitting diodes using color-tunable carbazole-based iridium complexes," *Chemical Physics Letters*, vol. 422, pp. 386-390, 2006.
- [153] A. Tsuboyama, H. Iwawaki, M. Furugori, T. Mukaide, J. Kamatani, S. Igawa, T. Moriyama, S. Miura, T. Takiguchi, S. Okada, M. Hoshino, and K. Ueno, "Homoleptic cyclometalated iridium complexes with highly efficient red phosphorescence and application to organic light-emitting diode," *Journal of the American Chemical Society*, vol. 125, pp. 12971-12979, 2003.
- [154] Y. Kawamura, K. Goushi, J. Brooks, J. J. Brown, H. Sasabe, and C. Adachi, "100% phosphorescence quantum efficiency of Ir(III) complexes in organic semiconductor films," *Applied Physics Letters*, vol. 86, pp. 071104-3, 2005.

- [155] X. Gong, M. R. Robinson, J. C. Ostrowski, D. Moses, G. C. Bazan, and A. J. Heeger, "High-efficiency polymer-based electrophosphorescent devices," *Advanced Materials*, vol. 14, pp. 581-585, 2002.
- [156] P. M. Borsenberger, L. Pautmeier, R. Richert, and H. Bassler, "Hole transport in 1,1-bis(di-4-tolylaminophenyl)cyclohexane," *Journal of Chemical Physics*, vol. 94, pp. 8276-8281, 1991.
- [157] X. Gong, J. C. Ostrowski, D. Moses, G. C. Bazan, and A. J. Heeger, "Electrophosphorescence from a polymer guest-host system with an iridium complex as guest: Forster energy transfer and charge trapping," *Advanced Functional Materials*, vol. 13, pp. 439-444, 2003.
- [158] Y. H. Niu, B. Q. Chen, S. Liu, H. Yip, J. Bardecker, A. K. Y. Jen, J. Kavitha, Y. Chi, C. F. Shu, Y. H. Tseng, and C. H. Chien, "Highly efficient red electrophosphorescent devices based on an iridium complex with trifluoromethyl-substituted pyrimidine ligand," *Applied Physics Letters*, vol. 85, pp. 1619-1621, 2004.
- [159] N. Rehmman, C. Ulbricht, A. Kohnen, P. Zacharias, M. C. Gather, D. Hertel, E. Holder, K. Meerholz, and U. S. Schubert, "Advanced device architecture for highly efficient organic light-emitting diodes with an orange-emitting crosslinkable iridium(III) complex," *Advanced Materials*, vol. 20, pp. 129-133, 2008.
- [160] X. Gong, S. Wang, D. Moses, G. C. Bazan, and A. J. Heeger, "Multilayer polymer light-emitting diodes: white-light emission with high efficiency," *Advanced Materials*, vol. 17, pp. 2053-2058, 2005.
- [161] J. Li, T. Sano, Y. Hirayama, T. Tomita, H. Fujii, and K. Wakisaka, "Improvement of electroluminescence efficiency of blue-polymer-light-emitting diodes using polymer hole-transporting and electron-transporting layers," *Japanese Journal of Applied Physics Part 1-Regular Papers Brief Communications & Review Papers*, vol. 45, pp. 3746-3749, 2006.
- [162] X. D. Niu, C. J. Qin, B. H. Zhang, J. W. Yang, Z. Y. Xie, Y. X. Cheng, and L. X. Wang, "Efficient multilayer white polymer light-emitting diodes with aluminum cathodes," *Applied Physics Letters*, vol. 90, p. 203513, 2007.
- [163] C. A. Olivati, A. J. F. Carvalho, D. T. Balogh, and R. M. Faria, "Electrical properties of polymer/metal interface in polymer light-emitting devices: electron injection barrier suppression," *Journal of Materials Science*, vol. 41, pp. 2767-2770, 2006.
- [164] L. Wang, B. Liang, F. Huang, J. B. Peng, and Y. Cao, "Utilization of water/alcohol-soluble polyelectrolyte as an electron injection layer for fabrication of high-efficiency multilayer saturated red-phosphorescence polymer light-

- emitting diodes by solution processing," *Applied Physics Letters*, vol. 89, p. 151115, 2006.
- [165] W. L. Ma, P. K. Iyer, X. Gong, B. Liu, D. Moses, G. C. Bazan, and A. J. Heeger, "Water/methanol-soluble conjugated copolymer as an electron-transport layer in polymer light-emitting diodes," *Advanced Materials*, vol. 17, pp. 274-277, 2005.
- [166] Y. Zhang, F. Huang, A. K. Y. Jen, and Y. Chi, "High-efficiency and solution processible multilayer white polymer light-emitting diodes using neutral conjugated surfactant as an electron injection layer," *Applied Physics Letters*, vol. 92, p. 063303, 2008.
- [167] K. Zhang, Z. Chen, C. L. Yang, X. W. Zhang, Y. T. Tao, L. Duan, L. Chen, L. Zhu, J. G. Qin, and Y. Cao, "Improving the performance of phosphorescent polymer light-emitting diodes using morphology-stable carbazole-based iridium complexes," *Journal of Materials Chemistry*, vol. 17, pp. 3451-3460, 2007.
- [168] K. Tamao, M. Uchida, T. Izumizawa, K. Furukawa, and S. Yamaguchi, "Silole derivatives as efficient electron transporting materials," *Journal of the American Chemical Society*, vol. 118, pp. 11974-11975, 1996.
- [169] X. W. Zhan, C. Risko, F. Amy, C. Chan, W. Zhao, S. Barlow, A. Kahn, J. L. Bredas, and S. R. Marder, "Electron affinities of 1,1-diaryl-2,3,4,5-tetraphenylsiloles: Direct measurements and comparison with experimental and theoretical estimates," *Journal of the American Chemical Society*, vol. 127, pp. 9021-9029, 2005.
- [170] H. Murata, G. G. Malliaras, M. Uchida, Y. Shen, and Z. H. Kafafi, "Non-dispersive and air-stable electron transport in an amorphous organic semiconductor," *Chemical Physics Letters*, vol. 339, pp. 161-166, 2001.
- [171] H. Murata, Z. H. Kafafi, and M. Uchida, "Efficient organic light-emitting diodes with undoped active layers based on silole derivatives," *Applied Physics Letters*, vol. 80, pp. 189-191, 2002.
- [172] B. Z. Tang, X. W. Zhan, G. Yu, P. P. S. Lee, Y. Q. Liu, and D. B. Zhu, "Efficient blue emission from siloles," *Journal of Materials Chemistry*, vol. 11, pp. 2974-2978, 2001.
- [173] Y. Hamada, C. Adachi, T. Tsutsui, and S. Saito, "Blue-light-emitting organic electroluminescent devices with oxadiazole dimer dyes as an emitter," *Japanese Journal of Applied Physics Part 1-Regular Papers Short Notes & Review Papers*, vol. 31, pp. 1812-1816, 1992.
- [174] Y. Kawabe and J. Abe, "Electron mobility measurement using exciplex-type organic light-emitting diodes," *Applied Physics Letters*, vol. 81, pp. 493-495, 2002.

- [175] S. Oyston, C. S. Wang, G. Hughes, A. S. Batsanov, I. F. Perepichka, M. R. Bryce, J. H. Ahn, C. Pearson, and M. C. Petty, "New 2,5-diaryl-1,3,4-oxadiazole-fluorene hybrids as electron transporting materials for blended-layer organic light emitting diodes," *Journal of Materials Chemistry*, vol. 15, pp. 194-203, 2005.
- [176] D. O'Brien, A. Bleyer, D. G. Lidzey, D. D. C. Bradley, and T. Tsutsui, "Efficient multilayer electroluminescence devices with poly(*m*-phenylenevinylene-co-2,5-dioctyloxy-*p*-phenylenevinylene) as the emissive layer," *Journal of Applied Physics*, vol. 82, pp. 2662-2670, 1997.
- [177] Q. Lei, B. Debasis, and H. H. Paul, "Effects of ultraviolet light irradiation on poly(vinylcarbazole)," *Applied Physics Letters*, vol. 92, p. 053303, 2008.
- [178] T. W. Lee, T. Noh, B. K. Choi, M. S. Kim, D. W. Shin, and J. Kido, "High-efficiency stacked white organic light-emitting diodes," *Applied Physics Letters*, vol. 92, p. 043301, 2008.
- [179] J. Kido, M. Kimura, and K. Nagai, "Multilayer white light-emitting organic electroluminescent device," *Science*, vol. 267, pp. 1332-1334, 1995.
- [180] T. Tsuboi, H. Murayama, and A. Penzkofer, "Photoluminescence characteristics of Ir(ppy)₃ and PtOEP doped in TPD host material," *Thin Solid Films*, vol. 499, pp. 306-312, 2006.
- [181] S. Steudel, K. Myny, V. Arkhipov, C. Deibel, S. De Vusser, J. Genoe, and P. Heremans, "50MHz rectifier based on an organic diode," *Nature Materials*, vol. 4, pp. 597-600, 2005.
- [182] A. J. Campbell, D. D. C. Bradley, J. Laubender, and M. Sokolowski, "Thermally activated injection limited conduction in single layer N,N'-diphenyl-N,N'-bis(3-methylphenyl)1-1'-biphenyl-4,4'-diamine light emitting diodes," *Journal of Applied Physics*, vol. 86, pp. 5004-5011, 1999.
- [183] L. Bozano, S. A. Carter, J. C. Scott, G. G. Malliaras, and P. J. Brock, "Temperature- and field-dependent electron and hole mobilities in polymer light-emitting diodes," *Applied Physics Letters*, vol. 74, pp. 1132-1134, 1999.
- [184] G. G. Malliaras and J. C. Scott, "Numerical simulations of the electrical characteristics and the efficiencies of single-layer organic light emitting diodes," *Journal of Applied Physics*, vol. 85, pp. 7426-7432, 1999.
- [185] A. Kumar, P. K. Bhatnagar, P. C. Mathur, M. Husain, S. Sengupta, and J. Kumar, "Temperature and electric-field dependences of hole mobility in light-emitting diodes based on poly [2-methoxy-5-(2-ethylhexoxy)-1,4-phenylene vinylene]," *Journal of Applied Physics*, vol. 98, p. 024502, 2005.

- [186] P. W. M. Blom, M. J. M. deJong, and J. J. M. Vlegaar, "Electron and hole transport in poly(*p*-phenylene vinylene) devices," *Applied Physics Letters*, vol. 68, pp. 3308-3310, 1996.
- [187] W. Brutting, S. Berleb, and A. G. Muckl, "Space-charge limited conduction with a field and temperature dependent mobility in Alq light-emitting devices," *Synthetic Metals*, vol. 122, pp. 99-104, 2001.
- [188] P. S. Davids, I. H. Campbell, and D. L. Smith, "Device model for single carrier organic diodes," *Journal of Applied Physics*, vol. 82, pp. 6319-6325, 1997.
- [189] C. C. Lee, Y. D. Jong, P. T. Huang, Y. C. Chen, P. J. Hu, and Y. Chang, "Numerical simulation of electrical model for organic light-emitting devices with fluorescent dopant in the emitting layer," *Japanese Journal of Applied Physics Part 1-Regular Papers Brief Communications & Review Papers*, vol. 44, pp. 8147-8152, 2005.
- [190] F. Neumann, Y. A. Genenko, C. Melzer, and H. von Seggern, "Self-consistent theory of unipolar charge-carrier injection in metal/insulator/metal systems," *Journal of Applied Physics*, vol. 100, p. 084511, 2006.
- [191] S. J. Martin, A. B. Walker, A. J. Campbell, and D. D. C. Bradley, "Electrical transport characteristics of single-layer organic devices from theory and experiment," *Journal of Applied Physics*, vol. 98, p. 063709, 2005.
- [192] T. Ogawa, D.-C. Cho, K. Kaneko, T. Mori, and T. Mizutani, "Numerical analysis of the carrier behavior of organic light-emitting diode: comparing a hopping conduction model with a SCLC model," *Thin Solid Films*, vol. 438-439, pp. 171-176, 2003.
- [193] J. L. Maldonado, M. Bishop, C. Fuentes-Hernandez, P. Caron, B. Domercq, Y. D. Zhang, S. Barlow, S. Thayumanavan, M. Malagoli, J. L. Bredas, S. R. Marder, and B. Kippelen, "Effect of substitution on the hole mobility of bis(diarylamino)biphenyl derivatives doped in poly(styrene)," *Chemistry of Materials*, vol. 15, pp. 994-999, 2003.
- [194] P. Peumans, A. Yakimov, and S. R. Forrest, "Small molecular weight organic thin-film photodetectors and solar cells," *Journal of Applied Physics*, vol. 93, pp. 3693-3723, 2003.
- [195] S. Naka, H. Okada, H. Onnagawa, Y. Yamaguchi, and T. Tsutsui, "Carrier transport properties of organic materials for EL device operation," *Synthetic Metals*, vol. 111, pp. 331-333, 2000.
- [196] T. Y. Chu and O. K. Song, "Hole mobility of *N,N'*-bis(naphthalen-1-yl)-*N,N'*-bis(phenyl) benzidine investigated by using space-charge-limited currents," *Applied Physics Letters*, vol. 90, p. 203512, 2007.

- [197] V. I. Adamovich, S. R. Cordero, P. I. Djurovich, A. Tamayo, M. E. Thompson, B. W. D'Andrade, and S. R. Forrest, "New charge-carrier blocking materials for high efficiency OLEDs," *Organic Electronics*, vol. 4, pp. 77-87, 2003.
- [198] S. Yoo, B. Domercq, and B. Kippelen, "Intensity-dependent equivalent circuit parameters of organic solar cells based on pentacene and C₆₀," *Journal of Applied Physics*, vol. 97, p. 103706, 2005.
- [199] S. Barth, P. Muller, H. Riel, P. F. Seidler, W. Rie, H. Vestweber, U. Wolf, and H. Bassler, "Electron injection into an Alq₃ single-layer organic light-emitting diode," *Synthetic Metals*, vol. 111-112, pp. 327-330, 2000.
- [200] F. Yakuphanoglu, E. Basaran, B. F. Senkal, and E. Sezer, "Electrical and optical properties of an organic semiconductor based on polyaniline prepared by emulsion polymerization and fabrication of Ag/Polyaniline/n-Si Schottky diode," *Journal of Physical Chemistry B*, vol. 110, pp. 16908-16913, 2006.
- [201] P. Peumans and S. R. Forrest, "Very-high-efficiency double-heterostructure copper phthalocyanine/C₆₀ photovoltaic cells," *Applied Physics Letters*, vol. 79, pp. 126-128, 2001.
- [202] D. J. Milliron, I. G. Hill, C. Shen, A. Kahn, and J. Schwartz, "Surface oxidation activates indium tin oxide for hole injection," *Journal of Applied Physics*, vol. 87, pp. 572-576, 2000.
- [203] I. G. Hill and A. Kahn, "Combined photoemission/*in vacuo* transport study of the indium tin oxide/copper phthalocyanine/*N,N*-diphenyl-*N,N*'-bis(1-naphthyl)-1,1'-biphenyl-4,4" diamine molecular organic semiconductor system," *Journal of Applied Physics*, vol. 86, pp. 2116-2122, 1999.
- [204] N. J. Watkins, L. Yan, and Y. L. Gao, "Electronic structure symmetry of interfaces between pentacene and metals," *Applied Physics Letters*, vol. 80, pp. 4384-4386, 2002.